BUBBLE DYNAMICS AND ACOUSTIC DROPLET VAPORIZATION IN GAS EMBOLOTHERAPY

by

David S. Li

A dissertation submitted in partial fulfillment
of the requirements for the degree of
Doctor of Philosophy
(Biomedical Engineering)
in the University of Michigan
2014

Doctoral Committee:

Professor Joseph L. Bull, Chair
Assistant Professor Krzysztof J. Fidkowski
Professor J. Brian Fowlkes
Professor Shuichi Takayama

To my loving mother, father, and sister
for their unconditional love and support

Acknowledgements

I am grateful to have had the good fortune to interact with an amazing group of individuals throughout my doctoral studies at the University of Michigan at Ann Arbor. Without their collective efforts, advice, and moral support the work presented in this dissertation could not have been possible. I would first like to credit the guidance and training from my doctoral committee members – Professors Joe Bull, Chris Fidkowski, Brian Fowlkes, and Shuichi Takayama. I would like to thank my advisor, Joe Bull, for the mentorship, discussion, and support throughout the years. My understanding of bubble dynamics and acoustics was only possible with the guidance from Brian Fowlkes. My fundamental training in computational tools for fluid mechanics could not have been complete without the advisement from Chris Fidkowski. Finally, the generosity from Shuichi Takayama and access to resources did not go unappreciated. And to my committee as a whole, I would like to thank them all for the mentoring and training that helped craft me into the scientist and engineer I am today.

The assistance and thought provoking discussions from the current and former lab members throughout the years was much appreciated. But more importantly, they created the most light-hearted and enjoyable work atmosphere on a day-to-day basis I will ever experience. For that reason, I will never forget my friends and colleagues from the Biotransport Lab – Stanley Samuel, Robinson Seda, John Pitre, Adnan Qamar, Rob Dodde, Sam Stephenson, Nelson Smith, Marty Schlicht and ZZ Wong.

Aside from Biotransport Lab, my studies could not have been completed without the generous help of collaborators throughout the years. I would like to thank Mario Fabiilli and Oliver Kripfgans from the Basic Radiological Sciences ultrasound group for their help with droplet supply, ultra-high speed camera setup, and thought-provoking discussion on all things acoustic droplet vaporization related. From the histotripsy group, I am incredibly grateful for Yohan Kim's assistance and willingness to perform transducer calibrations upon request. I would also like to thank Brian Johnson for the advice, training, and access to resources allowing me to construct the microfluidic devices throughout academic pursuits.

Most importantly, the level of appreciation I have for the patience, counseling, and encouragement throughout the years from my family cannot be sufficiently expressed in words. My mother and father have always been an incredible source of inspiration and along with my loving sister and best friend, Amy, my family has always provided laughter and love. Once again, I would like to thank my dearest family for everything they provided throughout my life. Without them, none of this could have been accomplished.

Table of Contents

List of Tables

List of Figures

List of Appendices

List of Symbols and Acronyms

ADV – Acoustic droplet vaporization

A.U. – Arbitrary units

BEM – Boundary element method

D – Diameter

DI – Deionized

DDFP – Dodecafluoropentane

f – F-number

HCC – Hepatocellular carcinoma

HIFU – High-intensity focused ultrasound

MI – Mechanical index

N – Discreet count

PDMS – Polydimethylsiloxane

PFC – Perfluorocarbon

PNP – Peak negative pressure

PPP – Peak positive pressure

Q – Flow rate

R – Radius

STD – Standard deviation

T_C – Critical limit of super heat

TACE - Transarteriole chemoembolotherapy

TAE – Transarteriole embolotherapy

V – Velocity

c – Speed of sound

c_{kj} – Conditional constant for boundary element model

Ca – Capillary number

δ_{kj} – Dirac delta function

f – Frequency

f_i – Stress component

$\vec{f}$ – Stress vector

G_{ij} – Stokeslet

k – Contact line velocity scaling constant

$\varkappa$ – Curvature

λ – Wavelength

l – Length

$\vec{n}$ – Normal vector

ρ – Density

p – Pressure

t – Time

T– Time

R_b – Bubble Radius

R_v – Vessel Radius

Re – Reynolds Number

τ – Shear Stress

T_{ijk} – Stresslet

$\vec{T}$ – Torque

θ_D – Dynamic contact angle

θ_S – Static contact angle

σ – (Chapter V) Stress, (Chapter VI) surface tension

μ – Viscosity

$\vec{u}$ – Velocity vector

u_{cl} – Contact line velocity

V_b – Bubble interface velocity

x – Position

$\vec{x}_0$ – Singular point location

$\vec{Y}$ – Moving interface points

Abstract

Gas embolotherapy is a twist on traditional catheter based embolotherapy approaches. Rather than using a solid or semi-solid embolizing agent to restrict blood flow, localized gas bubbles are used instead. These gas bubbles are formed by the controlled vaporization of intravenously injected liquid microdroplets using focused ultrasound. This vaporization process is often referred to as acoustic droplet vaporization (ADV). A greater understanding of the ADV process, bubble transport, and acoustic-bubble interactions are essential to devising a safe and effective therapy.

This dissertation delves into the dynamics at various time-scales throughout the ADV process from the initial conversion process up to the bubble transport in vessels. The following work has been divided into five time-scale events that may occur throughout the ADV process. First, ultra-high speed imaging investigating the initial gas nucleus formation within liquid microdroplets is compared against a numerical model of the acoustic field within the droplet to determine the mechanism behind ADV. After the droplet is converted into a high-pressure bubble, the effect of pulse length and acoustic power are correlated with the likelihood of collapsing the newly formed bubble possibly resulting in vessel damage. Next, influences from channel resistance on the bubble expansion rates are investigated by comparing the ADV bubble evolution process in free-field conditions versus in a constrained microchannel. Once a bubble is formed, transport phenomena and possible additional acoustic pulses may influence bubble dynamics and the efficacy of the treatment.

The scenario of a finite-sized bubble attached to a vessel wall approaching a bifurcation point is modeled using the boundary element method in order to understand the influences of sticking conditions and bifurcation geometry on bubble lodging or dislodging. Finally, an instability resulting from short acoustic pulses impinging on a bubble attached to a solid boundary resulting in droplet atomization of the bulk liquid in the bubble is characterized.

The implications from all of these dynamics are discussed in the context of gas embolotherapy as well as other bubble or ADV based therapies. It is concluded that potential sources of damage include bubble torus formation, rapid expansion of relatively large droplets in small vessels, and contact line motion of the bubble. However, it is revealed that the possible sources of vessel damage can be addressed through careful modulation of acoustic parameters, choice of droplet size distribution, and conditions that promote bubble lodging. Furthermore, a mechanism under controlled acoustic conditions may result in bioeffects allowing for enhanced drug transport across the vessel wall is presented.

CHAPTER I: INTRODUCTION

Background and Motivation

Embolotherapy is the occlusion of blood vessels using foreign bodies for therapeutic applications. Often performed by interventional radiologists, embolotherapy requires careful and strategic transcatheter delivery of solids or semi-solid usually in the forms of gel-foams, polymer beads, balloons, and wire coils to selective feeder vessels to cause blood occlusion[1]. Embolotherapy has been extensively used in the mitigation of uncontrolled bleeding in the gastrointestinal regions due to ulcerative diseases, pancreatitis, diverticular disease, angiodysplasia, and etc. as well as controlling traumatic hemorrhages in kidneys, liver, and spleen[2]. It has also been proven to be efficacious and used extensively in the treatment uterine fibroids and is has been proposed as a method of treating various forms of vascularized cancers, such as hepatocellular carcinoma (HCC) and renal carcinoma[3,4].

HCC is the most common form of liver cancer accounting for 85-90% of all forms of liver cancer[5]. It is found in 30 per 100,000 males every year, and it responsible for 1.25 million deaths every year. The difficulty with treating HCC is that 70-85% of patients with HCC also have liver cirrhosis, rendering most patients ineligible for traditional methods of treatment such as tumor resection[6]. On top of that, chemotherapy treatments alone have also been found ineffective in treating HCC[6]. However, case studies have shown that HCC can be successfully treated using embolotherapy techniques to cause tumor necrosis[7,8].

The concept of restricting blood supply to "starve" cancerous tumors was first successfully demonstrated by Boehm *et al.* in 1997[9]. The embolizing agent is typically delivered by navigation of a catheter through the vasculature down to specific feeder vessels. Laccourreye *et al.* 1993 was able to demonstrate that if administered a sufficiently high density of solid particles locally in a blood vessel, this will result in occlusion of the vessel, diversion of blood flow to neighboring vessels, and resulting in permanent tissue damage at the site of embolization[10]. Case studies have shown that of HCC have been treated effectively using transarterial embolotherapy (TAE). Further studies have suggested that embolotherapy can be further enhanced through the coupled delivery of chemotherapeutics, also known as transarterial chemoembolization (TACE). However, recent reports have shown that the outcomes using TACE or TAE for HCC treating show no statistical difference[6, 8]. Although curative measures, such as liver transplant or tumor resection, are preferred for early stage tumors, only 30-40% of patients are suitable for such treatments. Therefore majority of patients are presented with locoregional or palliative alternatives therapies with TAE or TACE as the primary therapeutic approaches. Several additional challenges associated with catheterization have created barriers in favor against using traditional embolotherapy techniques as a cancer therapy. Traditional embolotherapy techniques are time intensive procedures often requiring catheterization to strategic blood vessels for emboli delivery to minimize collateral tissue damage. Embolotherapy treatments quickly become too labor and time intensive when several feeder vessels must be occluded for successful treatment. Interventional radiologists are often limited to catherizing and occluding at most a handful of vessels. Additionally, catheter based embolization treatments require fluoroscopy and these complex, extended procedures can easily lead to prolonged

fluoroscopic radiation exposure to the skin thus increasing risk to forms of melanoma[2]. With embolotherapy, the most lethal complication is inadvertent embolization of major vessels, thus embolotherapeutic treatment of tumors has typically been used as a last resort[2].

Gas embolotherapy is a novel departure from the traditional catheter based methods of embolotherapy, which may be well suited as an ultrasound based cancer therapy aimed at treating highly vascularized tumors such as HCC[4, 11, 12]. This gas embolotherapy approach was first described, and later patented, by Apfel 1998[13]. Rather than using the aforementioned solid or semi-solid embolizing agents, liquid pefluorocarbon (PFC) microdroplets are introduced into the vascular network and selectively activated using focused ultrasound transducer to form gas bubbles 125 times larger than the initial droplet volumetrically[14]. The droplets are formulated such that its mean diameter is on the order, if not smaller, than erythrocytes found in the blood stream. Therefore the liquid PFC microdroplets are allowed to freely circulate through the vasculature and do not disrupt the microcirculation. Only when the droplets are selectively activated using ultrasound do they form a larger gas bubble that can lodge in the vasculature, diverting blood supply, and eventually causing tumor necrosis[14].

The activation process of the microdroplets to form the gas phase emboli relies on a mechanism referred to as acoustic droplet vaporization (ADV). The ADV process is a threshold based phenomena when a sufficiently high intensity pulse of acoustic energy, normally in the form of focused high frequency ultrasound, is directed at the droplets causing the droplets to vaporize forming gas bubbles. The formulations of the droplets are critical in both stability and activation of the droplets. In biomedical application, the droplet material chosen must have a bulk boiling point lower than body temperature (37°C) and is

normally various of chemical derivatives of PFCs. Because the droplets are packaged in droplet form, the Laplace pressure from interfacial tension is able to suppress spontaneous vaporization due to droplet boiling by raising the boiling point within the droplet[15]. The microdroplets used for gas embolotherapy are on the size order of 3 microns in diameter[14]. Typically, the microdroplets used in biomedical applications use feature a dodecafluoropentane (DDFP, CAS No. 678–26–2) with a bulk material boiling point of 29°C at atmospheric pressure and are encapsulated with a lipid or albumin based shell. Although the bulk fluid boiling point of DDFP is lower than body temperature and the level of boiling point reduction from the Laplace pressure is variable. Stability studies on albumin encapsulated DDFP microdroplets have been shown to be stable up to 65°C[14]. In recent years further investigation has gone towards using other PFCs including perfluoropropane (CAS No. 76-19-7), perfluorobutane (CAS No. 355-25-9), perfluorohexane (CAS No. 355-42-0), and perfluorooctane (CAS No. 307-34-6) in an effort to augment acoustic thresholds or droplet stability[16-21].

The envisioned gas embolotherapy treatment would begin with intravenous bolus injections of microdroplet suspensions. The microdroplets would then circulate throughout the blood stream in an inert state. At the tumor site, focused ultrasound can be applied which then vaporizes the droplets (Figure 1.1). The resulting bubbles could then occlude the tumor vasculature on the time scales of 30 minutes to 2 hours[4]. Multiple treatments could be performed until sufficient tumor occlusion is observed. The treatment is meant to be minimally invasive and have high spatial selectivity. Although gas embolotherapy is currently catered towards the treatment of HCC, the treatment can be extended to other forms of cancer such as renal carcinoma, small cell lung cancer, etc. Gas embolotherapy has been

proposed as a method of enhancing chemotherapy as well radiofrequency ablation by reducing convection of chemotherapeutics or heat away from the targeted site due to blood flow[22].

Interest in the ADV process goes beyond gas embolotherapy in the field of medicine as ADV processes are currently being applied towards drug delivery vehicles and more stable forms of contrast agents, also referred to as phase change contrast agents (PCCA)[20, 21]. More sophisticated dual phase PFC microdroplets featuring a PFC layer encapsulating a water core with dissolved drug has been shown to be a successful platform in preventing inadvertent drug leakage prior to vaporization[17, 18]. In the PCCA front, allowing contrast agents to circulate in its liquid state and locally vaporizing them to create gaseous resonating bubbles has been shown to extend the lifetime of contrast agents per dose[20]. As additional interest in using ADV in medicine increases it is important to gain a better understanding into the mechanics of the ADV process to mitigate unwanted bioeffects such as cell or tissue damage. Alternatively, the ability to control the level of stresses induced may illicit bioeffects such as the enhancement of drug delivery[23-25].

The ADV process can be broken up into 3 phases (Figure 1.2): gas nucleation site formation, expansion phase of the bubble, and diffusion or dissolution into the bulk media. The gas nucleation site formation phase is the first event in the process where isolated gas bubbles are formed within the liquid PFC droplet. These gas nuclei serve as sources for the liquid PFC to convert to its gas phase. Hypotheses behind the actual mechanics driving the ADV are still debated, but what is known is that the phase change process lasts on the order of 1 microsecond and during the phase change process there is little bubble expansion observed[19, 26-28]. Once the droplet has changed phase in the first microsecond, a high-

pressure bubble is generated and begins to undergo a rapid expansion in order to reach its equilibrium diameter (approximately 125 volumetric or 5 time diametric expansion). This process lasts less than 100 microseconds and can achieve interfacial velocities of up to 2 m/s[29, 30]. Theoretical models and limited experimental data suggest that during the rapid expansion when the bubble nears the equilibrium size the bubble can either slowly approach the equilibrium diameter or overshoot and relax to the equilibrium diameter. Several numerical models have been developed over the years in an effort to better estimate the expansion rates and extrapolate approximate stresses experienced. These models range from 1D model to 2D models from the most basic condition of simple expansion with rigid boundaries to the inclusion of flexible walls or the gas conversion process[30-33]. Currently limited experimental data exists resolving the expansion rates of droplets in bulk fluid let alone in small vessel like conditions[29, 34]. Once the PFC bubble has formed transport phenomena and gas diffusion processes can take over until the bubbles finally completely dissolves into the blood stream. During this period bubbles may persist in the vasculature for minutes to hours or even days. Once the stable bubble has been formed dynamics of the bubble are more ubiquitous to ultrasound-bubble based applications. As a result questions with regards to cavitation[25, 28, 35], bubble jets[36-38], sonoporation[25, 39], bubble lodging and transport[40-43], etc. and possibly coupling such dynamics for drug delivery[15, 24, 44, 45] or ultrasound therapy[46-48] are of great interest.

The following work explores the dynamics behind the ADV process at various time scales, from the initial nucleation site formation up to longer time scale transport phenomena of bubbles through vessels as well as possible acoustic-bubble phenomena. This

work has been organized into the following chapters progressing through the phases throughout the lifetime of an ADV droplet:

- Chapter II (Initial nucleation site formation due to acoustic droplet vaporization) – The initial formation of the gas nucleus is observed within micrometer sized PFC droplets are directly imaged using ultra-high speed imaging. A numerical acoustic model was developed to predict where the initial gas nucleus would form within the droplet. The numerical model was used to verify a hypothesized acoustic mechanism initiating ADV.
- Chapter III (Formation of toroidal bubbles during acoustic droplet vaporization) – The dynamics immediately after the initial phase change is observed for varying pressures and pulse lengths from the transducer. The possible implications on vessel damage are also discussed.
- Chapter IV (The bubble evolution from acoustic droplet vaporization in microchannels) – The expansion process on the order of hundreds of microseconds are explored. Experiments were carried out for both free-field conditions as well as in microchannels representing idealized vessels. Effects from constraining the droplets to a channel are compared.
- Chapter V (A boundary element model of microbubble sliding through a bifurcation) – A numerical model using the boundary element method is development to probe the dynamics of bubbles attached to a vessel wall approaching a bifurcation to gain insight on finite sized bubbles traveling through a vessel.
- Chapter VI (Acoustic atomization process within bubbles attached to a solid boundary) – Once the bubble is formed classic problems beyond the context of gas

embolotherapy can take place with acoustic bubble interactions. A previously unobserved phenomenon of atomization events within bubbles attached to a solid boundary is discussed in detail in this chapter.

- Chapter VII (Conclusions and future directions) – Overall results are summarized and their impacts on gas embolotherapy as an ultrasound cancer therapy are discussed. Future directions and questions raised are also presented.

Chapter I: Figures

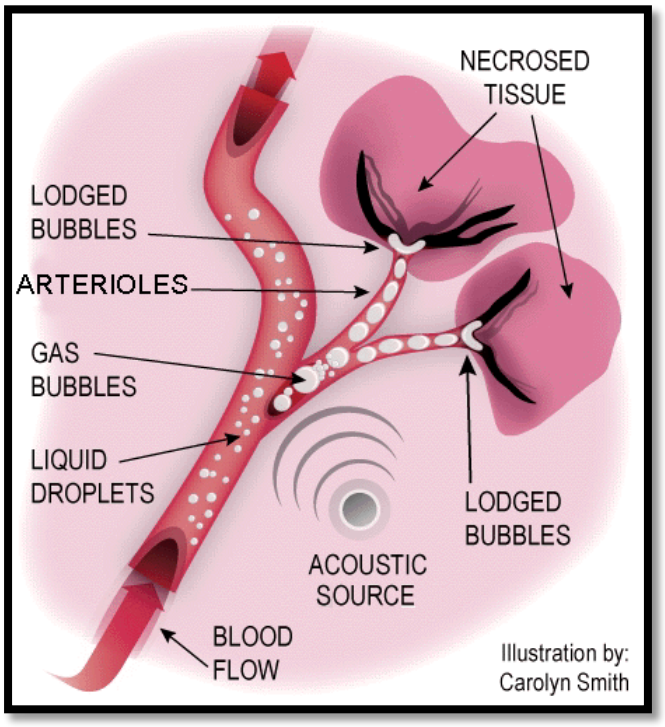

Figure 1. 1: Concept art of the gas embolotherpay. Gas emebolotherapy begins with the introduction of PFC microdroplets via intravenous injection. At the feeder vessel of the tumor, an ultrasound source is focused to vaporize the droplets. The subsequent bubbles that are formed can then lodge and occlude blood flow to the tumor, thus "starving" the tumor. Illustration by Carolyn Smith.

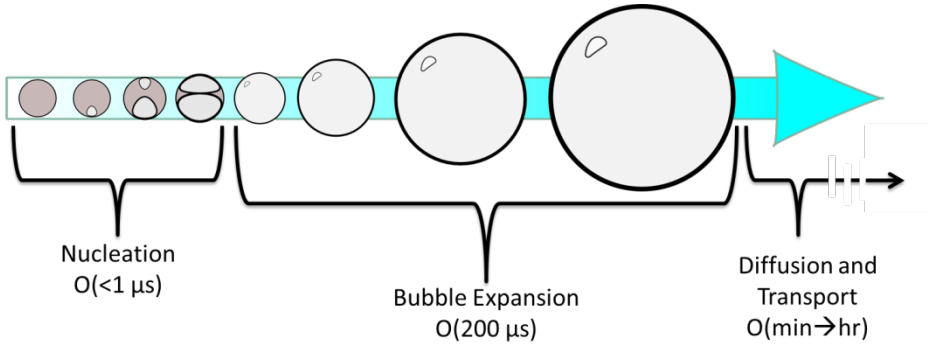

Figure 1. 2: Illustration showing the typical dynamics throughout the ADV timeline over the first 200 μs. An initial droplet is present and at time zero an ultrasound wave initiates a small gas nucleus to form within the droplet. On some occasions a second nucleation site forms on the opposing end of the droplet shortly after the first. The gas nuclei expand as liquid PFC is converted into its gas phase forming a high press bubble. Once the high-pressure bubble is formed a rapid expansion process occurs over a 50 μs period and eventually reaches an equilibrium size (on the order of 200 μs). Finally, the bubble can serve as a gas embolus until diffusion processes take over and the bubble dissolves into the bulk fluid.

Chapter I: References

[1] J. Golzarian, G. P. Siskin, M. Sharafuddin, H. Mimura and D. M. Coldwell, "Embolization Tools," in *Vascular Embolotherapy*, Germany, Springer Berlin Heidelberg, 2006, pp. 15-32.

[2] M. J. Sharafuddin, S. Sun and J. Golzarian, "Embolotherapy: Basic Principles and Applications," in *Vascular Embolotherapy*, Germany, Springer Berlin Heidelberg, 2006, pp. 3-13.

[3] G. P. Siskin, "Uterine Fibroid Embolization: Practice Development," in *Vascular Embolotherapy*, Germany, Springer Berlin Heidelberg, 2006, pp. 119-123.

[4] J. L. Bull, "Cardiovascular Bubble Dynamics," *Critical Reviews in Biomedical Engineering,* p. 33(4): 299–346, 2005.

[5] H. B. El-Serag and K. L. Rudolph, "Hepatocellular Carcinoma: Epidemiology and Molecular Carcinogenesis," *Gastroenterology,* p. 132(4): 2557–2576, 2007.

[6] N. Nakagawa and W. Castaneda-Zuniga, "Transcatheter chemoembolization for hepatocellular carcinoma and other promising transarterial therapies," in *Interventional Radiology*, Baltimore, Williams and Wilkins, 1997.

[7] R. Di Segni, A. Y. Young, Z. Qian and W. R. Castañeda-Zúñiga, "Embolotherapy: Agents, Equipment, and Techniques," in *Interventional Radiology*, Baltimore, Williams and Wilkins, 1997.

[8] M. Pleguezuelo, L. Marelli, M. Misseri, G. Germani, V. Calvaruso, E. Xiruochakis, P. Manousou and A. K. Burroughs, "TACE Versus TAE as Therapy for Hepatocellular Carcinoma," *Expert Review of Anticancer Therapy,* vol. 8, no. 10, pp. 1623-1641, 2008.

[9] T. Boehm, J. Folkman, T. Browder and M. S. O'Reilly, "Antiangiogenic Therapy of Experimental Cancer Does Not Induce Acquired Drug Resistance," *Letters to Nature,* pp. 390: 404-407, 1997.

[10] O. Laccourreye, A. Laurent, M. Polivka, M. Wassef, L. Domas, D. Brasnu and J. J. Merland, "Biodegradable Starch Microspheres for Cerebral Arterial Embolization," *Investigative Radiology,* pp. 28(2): 150-154, 1993.

[11] J. L. Bull, "The Application of Microbubbles for Targeted Drug Delivery," *Expert Opinion on Drug Delivery,* vol. 4, no. 5, pp. 475-493, 2007.

[12] Z. Z. Wong and J. L. Bull, "Microbubbles and Microdroplets for Drug Delivery," *Journal*

of Drug Delivery, Science, and Technology, vol. 21, no. 5, pp. 355-367, 2011.

[13] R. E. Apfel, "Activatable Infusible Dispersions Containing Droplets of a Superheated Liquid for Methods of Therapy and Diagnosis". United States of America Patent 5,840,276, 24 November 1998.

[14] O. D. Kripfgans, J. B. Fowlkes, D. L. Miller, O. P. Eldevik and P. L. Carson, "Acoustic Droplet Vaporization for Diagnostic Applications," *Ultrasound in Medicine and Biology,* p. 26(7): 1177–1189, 2000.

[15] N. Rapopart, K.-H. Nam, R. Gupta, Z. Gao, P. Mohan, A. Payne, N. Todd, X. Liu, T. Kim, J. Shea, C. Scaife, D. L. Parker, E.-K. Jeong and A. M. Kennedy, "Ultrasound-Mediated Tumor Imaging and Nanotherapy Using Drug Loaded, Block Copolymer Stabilized Perfluorocarbon Nanoemulsions," *Journal of Controlled Release,* vol. 153, pp. 4-15, 2011.

[16] P. Zhang and T. Porter, "An In Vitro Study of a Phase-Shift Nanoemulsion: A Potential Nucleation Agent for Bubble-Enhanced HIFU Tumor Ablation," *Ultrasound in Medicine and Biology,* vol. 36, no. 11, pp. 1856-1866, 2010.

[17] M. L. Fabiilli, K. J. Haworth, I. E. Sebastian, O. D. Kripfgans, P. L. Carson and J. B. Fowlkes, "Delivery of Chlorambucil Using Acoustically-Triggered Perfluoropentane Emulsion," *Ultrasound in Medicine & Biology,* vol. 36, no. 8, pp. 1364-1375, 2010.

[18] M. L. Fabiilli, J. A. Lee, O. D. Kripfgans, P. L. Carson and J. B. Fowlkes, "Delivery of Water-Soluble Drugs Using Acoustically Triggered Perfluorocarbon Double Emulsions," *Pharmaceutical Research,* p. 2753–2765, 2010.

[19] T. Giesecke and K. Hynynen, "Ultrasound-Mediated Cavitation Threshols of Liquid Perfluorocarbon Droplets in Vitro," *Ultrasound in Medicine and Biology,* pp. 1359-1365, 2003.

[20] P. S. Sheeran and P. A. Dayton, "Phase-Change Contrast Agents for Imaging and Therapy," *Current Pharmaceutical Design,* pp. 2152-2165, 2012.

[21] T. D. Martz, P. S. Sheeran, D. Bardin, A. P. Lee and P. A. Dayton, "Precision Manufacture of Phase-Change Perfluorocarbon Droplets Using Microfluidics," *Ultrasound in Medicine and Biology,* vol. 37, no. 11, pp. 1952-1957, 2011.

[22] O. D. Kripfgans, C. M. Orifici, P. L. Carson, K. A. Ives, O. P. Eldevik and B. J. Fowlkes, "Acoustic Droplet Vaporization for Temporal and Spatial Control of Tissue Occlusion: A Kidney Study," *IEEE Transactions on Ultrasonics, Ferroelectrics, and Frequency Controls,* pp. 52(7): 1101-1110, 2005.

[23] C. C. Chen, P. S. Sheeran, S.-Y. Wu, O. O. Olumolade, P. A. Dayton and E. E. Konofagou, "Targeted Drug Delivery with Focused Ultrasound-Induced Blood-Brain Barrier Opening Using Acoustically-Activated Nanodroplets," *Journal of Controlled Release,* p. In Press, 2013.

[24] K. W. Ferrara, "Driving delivery vehicles with ultrasound," *Advanced Drug Delivery Reviews,* p. 60:1097–1102, 2008.

[25] D. L. Miller, S. L. Pislaru and J. F. Greenleaf, "Sonoporation: Mechanical DNA Delivery by Ultrasonic Cavitation," *Somatic Cell and Molecular Genetics,* vol. 27, no. 1, pp. 115-134, 2002.

[26] O. D. Kripfgans, M. L. Fabiilli, P. L. Carson and J. B. Fowlkes, "On the acoustic vaporization of micrometer-sized droplets," *Journal of the Acoustical Society of America,* pp. 116(1): 272-281, 2004.

[27] O. Shpak, T. Kokhuis, Y. Luan, D. Lohse, N. de Jong, B. Fowlkes, M. Fabiilli and M. Versluis, "Ultrafast Dynamics of the Acoustic Vaporization of Phase-Change Microdroplets," *Journal of the Acoustical Society of America,* Accepted for publication.

[28] A. H. Lo, O. D. Kripfgans, P. L. Carson, E. D. Rothman and J. B. Fowlkes, "Acoustic Droplet Vaporization Threshold: Effects of Pulse Duration and Contrast Agent," *IEEE Transactions on Ultrasonics, Ferroelectrics, and Frequency Controls,* pp. 933-946, 2007.

[29] Z. Z. Wong, O. D. Kripfgans, A. Qamar, J. B. Fowlkes and J. L. Bull, "Bubble Evolution in Acoustric Droplet Vaporization at Physiological Temperature Via Ultra-High Speed Imaging," *Soft Matter,* 2011.

[30] A. Qamar, Z. Z. Wong, J. B. Fowlkes and J. L. Bull, "Evolution of Acoustically Vaporized Microdroplets in Gas Embolotherapy," *Journal of Biomechanical Engineering,* pp. 031010(1-12), 2012.

[31] A. Qamar, Z. Z. Wong, J. B. Fowlkes and J. L. Bull, "Dynamics of Acoustic Droplet Vaporization in Gas Embolotherapy," *Applied Physics Letters,* pp. 143702-1-3, 2010.

[32] T. Ye and J. L. Bull, "Direct Numerical Simulations of Micro-Bubble Expansion in Gas Embolotherapy," *Journal of Biomechanical Engineering,* pp. 126: 745-759, 2004.

[33] T. Ye and J. L. Bull, "Microbubble Expansion in a Flexible Tube," *Journal of Biomechanical Engineering,* pp. 128: 554-563, 2006.

[34] O. Shpak, L. Stricker, M. Versluis and D. Lohse, "The Role of Gas in Ultrasonically Driven Vapor Bubble," *Physics in Medicine and Biology,* vol. 58, p. 2523–2535, 2013.

[35] E. Sassaroli and K. Hynynen, "Cavitation Threshold of Microbubbles in Gel Tunnels by Focused Ultrasound," *Ultrasound in Medicine and Biology,* pp. 1651-1660, 2007.

[36] J. R. Blake, G. S. Keen, R. P. Tong and M. Wilson, "Acoustic Cavitation: The Fluid Dynamics of Non-Spherical Bubbles," *Philisophical Transactions of The Royal Society A,* vol. 357, pp. 251-267, 1999.

[37] E. Johnsen and T. Colonius, "Numerical Simulations of Non-Spherical Bubble Collapse," *Journal of Fluid Mechanics,* vol. 629, pp. 231-262, 2009.

[38] T. Kodama and Y. Tomita, "Cavitation Bubble Bahavior and Bubble-Shock Wave Interaction Near a Gelatin Surface as a Study of in Vivo Bubble Dynamics," *Applied Physics B: Lasers and Optics,* vol. 70, pp. 139-149, 1999.

[39] K. Ferrara, R. Pollard and M. Borden, "Ultrasound Microbubble Contrast Agents: Fundamentals and Application to Gene and Drug Delivery," *Annual Review of Biomedical Engineering,* vol. 9, pp. 415-447, 2007.

[40] A. J. Calderon, J. B. Fowlkes and J. L. Bull, "Bubble Splitting in Bifurcating Tubes: A Model Atudy of Cardiovascular Gas Emboli Transport," *Journal of Applied Physiology,* vol. 99, pp. 479-487, 2005.

[41] A. J. Calderon, B. Eshpuniyani, J. B. Fowlkes and J. L. Bull, "A Boundary Element Model of the Transport of a Semi-Infinite Bubble Through a Microvessel Bifurcation," *Physics of Fluids,* vol. 22, no. 061902, pp. 1-11, 2010.

[42] B. Eshpuniyani, J. B. Fowlkes and J. L. Bull, "A boundary element model of microbubble sticking and sliding in the microcirculation," *International Journal of Heat and Mass Transfer,* p. 51: 5700–5711, 2008.

[43] D. T. Valassis, R. E. Dodde, B. Eshpuniyani, J. B. Fowlkes and J. L. Bull, "Microbubble Transport Through a Bifurcating Vessel Network with Pulsatile Fow," *Biomedical Microdevices,* vol. 14, pp. 131-143, 2012.

[44] S. Hernot and A. L. Klibanov, "Microbubbles in Ultrasound-Triggered Drug and Gene Delivery," *Advanced Drug Delivery Reviews,* vol. 60, no. 10, pp. 1153-1166, 2008.

[45] M. S. Tartis, J. McCallan, A. F. Lum, R. LaBell, S. M. Stieger, T. O. Matsunaga and K. W. Ferrara, "Theraputic effects of paclitaxel-containing ultrasound contrast agents," *Ultrasound in Medicine & Biology,* p. 32(11):1771–1780, 2006.

[46] A. D. Maxwell, T.-Y. Wang, C. A. Cain, J. B. Fowlkes, O. A. Sapozhnikov, M. R. Bailey and Z. Xu, "Cavitation Clouds Created by Shock Scattering from Bubbles During Histotripsy," *Journal of the Acoustical Society of America,* vol. 130, no. 4, p. 1888–1898, 2011.

[47] Z. Xu, T. L. Hall, J. B. Fowlkes and C. A. Cain, "Optical and acoustic monitoring of bubble cloud dynamics at a tissue-fluid interface in ultrasound tissue erosion," *Journal of the Acoustical Society of America,* pp. 121(4): 2421-2430, 2007.

[48] J. C. Simon, O. A. Sapozhnikov, V. A. Khokhlova, Y.-N. Wang, L. A. Crum and M. R. Bailey, "Ultrasonic Atomization of Tissue and its Role in Tissue Fractionation by High Intensity Focused Ultrasound," *Physics in Medicine and Biology,* vol. 57, pp. 8061-8078, 2012.

CHAPTER II: INITIAL NUCLEATION SITE FORMATION DUE TO ACOUSTIC DROPLET VAPORIZATION

Introduction

Acoustic droplet vaporization (ADV) is a process in which liquid microdroplets are selectively vaporized using ultrasound to form larger gas bubbles. The ADV process has been proposed as the primary mechanism behind a potential ultrasound-based cancer therapy called gas embolotherapy[1-3]. In gas embolotherapy, liquid perfluorocarbon (PFC) microdroplets are intravenously injected into the bloodstream to freely circulate throughout the circulatory system. The PFCs chosen for droplet formulation have a bulk material boiling point below body temperature (i.e. < 37°C), such as docedafluoropentane (DDFP), and include a lipid or albumin shell stabilizing the droplet. Because of surface tension effects the boiling point of smaller droplets can be suppressed due to the Laplace pressure. However, the larger PFC microdroplets may not have a sufficiently high Laplace pressure to completely suppress spontaneous boiling and even a state of liquid superheat. Regardless, the degree of superheat of the larger PFC microdroplets is below the critical limit of super heat ($T_{C,DDFP}$=148°C)[4], minimizing the possibility of spontaneous explosive boiling from occurring. Furthermore, previous studies have shown that PFC microdroplets remain stable beyond 65°C[1, 5]. Studies have shown that ADV can offer sufficient occlusion in a supply vessel showing promise for gas embolotherapy[6, 7]. In addition to gas embolotherapy, the

ADV process has been proposed as a platform for localized drug delivery[8-10], high-intensity ultrasound (HIFU) tumor ablation[11], and phase-change contrast agents[12,13].

Few studies have examined the dynamics of the ADV process of PFC microdroplets. Earlier work paralleling the dynamics of ADV began with shock-induced explosive boiling by Frost in 1989[14]. Frost observed that the shock-induced vaporization process of liquid isopentane droplets differed from spontaneous explosive boiling. One of Frost's observations was that during shock-induced vaporization two consecutive gas nucleation sites developed in line with the propagation direction of the shockwave. The first nucleation site consistently appeared further from the shockwave source near the droplet interface, but never in the hemisphere proximal to the acoustic source. In the context of ADV of PFC microdroplets, Kripfgans *et al.* 2004 investigated the mechanism leading to nucleation[2] and Wong *et al.* 2011 focused on the expansion rates of PFC microbubbles following ADV[15]. Both Kripfgans *et al.* 2004 and Wong *et al.* 2011 shared similar observations with Frost that when two gas nucleation sites were formed, they were both on axis with the ultrasound. Kripfgans *et al.* 2004 hypothesized that the threshold for ADV of PFC droplets was directly linked to the amplitude in which the ultrasound was able to translate the droplet in an oscillatory fashion[2]. Giesecke and Hynynen 2003 recorded acoustic cavitation noise from ADV and hypothesized that nucleation originated outside the droplet interface as a cavitation bubble impinging on the droplet, penetrating the albumin shell, and initiating vaporization[5]. The proposed mechanism contradicted results suggesting that onset of ADV originates within the droplet and is cavitation independent[2, 16, 17]. More recently, Shpak *et al.* 2013 observed the nucleation process in single and double emulsion PFC droplets where in the latter case consistent localization of vaporization was observed, originating at 0.4·R away

from the center of the droplet along the axis of the ultrasound, where R is the droplet radius[18, 19]. The goal for this study is to directly visualize the nucleation site formation in liquid PFC microdroplets due to the ADV process and propose a potential mechanism initiating vaporization. A greater understanding behind the mechanics of the ADV process will allow the design of safer and more effective biomedical applications.

Methods

A schematic of the experimental setup is shown in figure 2.1. Individual PFC microdroplets were isolated in an acrylic tank containing degassed deionized (DI) water held at 37°C using a temperature controlled heating coil (HTP-1500, Adroit Medical Systems, Loudon, TN). Droplets were vaporized using single pulses of 3-15 cycles at 2.2-5.1 MPa peak negative pressure (PNP) from a 7.5 MHz single element f/2 (D=1.9 cm or 0.75 in) focused transducer (Panametrics A321S, Olympus, Waltham, MA). The transducer was fixed in place confocal to the optics at a 25° from the horizontal plane. The acoustic signal was generated by an HP 3314A function generator amplified by a Ritec GA-2500-A amplifier and monitored using an oscilloscope (WaveSurfer 44MXs, Teledyne LeCroy, Chestnut Ridge, NY). An Aligent 33120A function generator triggered the acoustic signal and gated the amplifier. The microdroplets (N=68) featured a DDFP liquid core (CAS No. 678–26–2) and an albumin shell. Details on the formulation of the PFC microdroplets can be found in Kripfgans *et al.* 2000[1]. The ADV event was captured using an inverted microscope (Nikon Eclipse TE2000-S, Nikon, Melville, NY) paired with ultra-high speed camera (SIM802, Specialised Imaging Ltd, Hertfordshire, UK) with 8 discreet CCDs, which captured 16 images at a time. The optical setup included a 4x, 10x, or 20x objective with 10x internal magnification from the microscope along with a 70-300mm Tamron f/4-5.6 macro

zoom lens with a reverse mounted 50 mm f/1.4 Nikkor lens on the camera providing an addition 1.4-6x magnification. In order to provide sufficient light to image the ADV process, a 300 Joule flash lamp (Adaptec AD300, Adapt Electronics, Essex, UK) with a fiber optic bundle was used to redirect light to the field of view providing a 15 μs burst of light.

Using COMSOL (COMSOL Inc., Burlington, MA) a finite element based model of the transient pressure acoustics module was used to simulate the acoustic field interacting with a static PFC microdroplet. The linear acoustics wave equations were solved in a cylindrical coordinate system, given by:

$$\frac{1}{\rho c^2}\frac{\partial^2 p}{\partial t^2} + \nabla\left(-\frac{1}{\rho}\nabla p\right) = 0 \tag{1}$$

Where ρ, c, p, and t represent density, speed of sound, pressure, and time, respectively. The density and speed of sound of water were assumed to be 993 kg/m^3 and 1523 m/s, respectively, while for DDFP the values were 1571 kg/m^3 and 405 m/s, respectively[20]. The model included the curved f/2 transducer element, similar to the transducer used during experiments, driven for 3 cycles in a water domain and the outer boundaries of the domain were radiating conditions representing unbounded constraints (Figure 2.2). Inside the domain a single PFC droplet was positioned at the spatial focal center of the transducer. The frequencies used in the study included the carrier frequency (7.5 MHz), the first harmonic (15 MHz), and the linear combination of the carrier frequency and the next two harmonics, which were matched according to intensity from hydrophone measurements (Figure 2.3). The time step selected was scaled according to the shortest harmonic wavelength in the DDFP domain versus the high frequency component imposed during simulations. A forward Euler time stepping scheme was used with a CFL condition

of 0.05. A time and grid convergence analysis was performed revealing convergence rates of 1.43 and 1.45 respectively (Figure 2.4). The convergence studies performed considered the case of a 3 cycle sine wave at 7.5 MHz interacting with a 70 μm diameter droplet. An irregular grid of triangular elements with linear basis functions was used. In the bulk fluid the element size was scaled according to the wavelength in water, and in the droplet the element sizes were scaled according to the wavelength in DDFP. Starting at the droplet interface in the bulk fluid half of the domain, the grid transitioned from the smaller DDFP domain element size to the larger water domain element size at an element growth rate of 1.06. Uniform grid refinement was used during the grid convergence study. For both grid and time convergence studies the change in pressure waveform in the droplet at a fixed point in time was used as the error metric for convergence. It was determined that 30 elements per wavelength for the bulk fluid domain and 30-50 elements per wavelength for the droplet provided sufficiently high accuracy solutions. The higher mesh densities were required for the small droplets in order to resolve the curvature of the droplet.

Results and Discussion

Approximately 25 μs after the initial firing of ultrasound the ADV process began, which was expected considering the sound speed in degassed DI water and the focal length of the transducer. The ADV process always began with a single gas nucleation site forming within the droplet (although the transducer was oriented at a shallow angle, it is recognized that this is single directional view and thus the localization of the nucleation site is limited by this projection). Occasionally a second nucleation site would form along the axis of the ultrasound propagation, which is consistent with previous observations[2, 14], shortly after the initial nucleation site is formed. After the nuclei were formed, the liquid PFC continued

converting into its gas phase causing the nuclei to grow in size. Visually, conversion of the liquid PFC to gas PFC would complete in the first 1-2 μs.

An in-house image edge detection script (in MATLAB) was used to identify and measure the distance between the centroid of the droplet and nucleus along the axis of acoustic propagation. Smaller droplets ($D_{droplet}$ < 20 μm) had the initial nucleation site form in the hemisphere closer to the ultrasound source (Figure 2.5), versus initial nucleation in larger droplets ($D_{droplet}$ > 20 μm) formed further from the ultrasound transducer. This differs from the conflicting observations from Frost[14] and Shpak *et al.* 2013[19] who both saw initial nucleation form exclusively on opposing sides of the droplet. However, in the limit where the PFC droplets are much larger than the wavelength (i.e. millimeter scale) the results match Frost's in the sense that initial nucleation may appear exclusively further from the acoustic source near the boundary of the droplet. As droplet size decreased, the wavelength begins to be of similar or longer than the droplet diameter and the initial nucleus traverses across the axis of acoustic propagation and forms proximal to the acoustic source (Figure 2.6) matching results and conditions from Shpak *et al.* 2013 who saw nucleation form at -0.4·R[19].

Visually, simulation results indicating the region of lowest acoustic pressure during the propagation of the acoustic wave within the droplet matched well with the experimentally observed location of first nucleation site formed (Figure 2.6). The simulated acoustic field shows a similar migration pattern of location of highest PNP to initial nucleus position as a function of wavelength to droplet diameter. Simulation results suggest that for droplets smaller than the half wavelength in DDFP (λ_{DDFP} = 54 μm), the carrier frequency is unable to refocus in the droplet. Because of reduced lensing effect from the carrier

wavelength being longer, the higher frequencies with shorter wavelengths are required to develop the high PNP regions in the droplet for ADV to occur. Also, as the droplet size decreased there was increased interference from the oncoming wave transmitted through the droplet interacting with the reflected wave from the back of the droplet as the wave passed through the droplet.

Because of the complex interactions that could occur within the droplet, inclusion of higher harmonics in the numerical model led to improvements in the model to describe the location of initial nucleation for small droplets (Figure 2.7). The increased reliance on higher pressures for ADV of increasingly smaller droplets is a likely outcome from the greater dependence on the presence of higher harmonics in the acoustic wave. Kripfgans *et al.* 2004, concluding that increasing transducer frequency lowers droplet vaporization threshold and also broadens the size range of droplets that can be easily vaporized[2].

Although the simulations suggest that a combination of acoustic lensing from the droplet and the short wavelength of DDFP from the slower speed of sound (c_{DDFP} = 405 m/s) determines where the largest PNP occurs within the droplet, ADV is a threshold-based process. Therefore tracking the location of 80% of the maximum PNP would reveal sensitivity of where nucleation may occur. Simulations confirm that if the acoustic output were beyond threshold, the PNP would cross threshold sooner causing nucleation to occur closer to the transducer as a whole. Plotting the 80% threshold PNP data against the initial nucleation site locations (Figure 2.7) shows excellent agreement. Furthermore the 80% threshold PNP acoustic fields still maintain good agreement with the shapes of the initial nucleus formed (Figure 2.6).

Mechanistically, acoustic lensing within the droplet may enhance the development of large local PNPs resulting in a cavitation-like event (i.e. nucleation site formation and onset of the ADV process). Once formed, the nucleation site appears stable and serves as a source for conversion of liquid to gaseous PFC, generating a high pressure bubble quickly undergoing rapid expansion to its equilibrium diameter described by Wong *et al.* 2011[15].

Conclusions

The location and development of gas nucleation sites formed within liquid PFC microdroplets during the ADV process was imaged. Simulation results and experimental results correlate well. This suggests that due to for shorter wavelength in DDFP than in water, an acoustic refocusing may be the source of nucleation. The range of wavelength to droplet diameters tested show the transition in initial nucleation site location Frost 1989[14] and Shpak *et al.* 2013[19] who observed initial nuclei form on opposing sides of the droplet. For the acoustic parameters used, the results indicate that the initial gas nucleus formed is always contained within the droplets. Furthermore, the ADV mechanism directly observed is potentially a different mechanism suggested from longer pulse lengths previously proposed by Giesecke and Hynynen 2003[5, 16, 17].

Chapter II: Figures

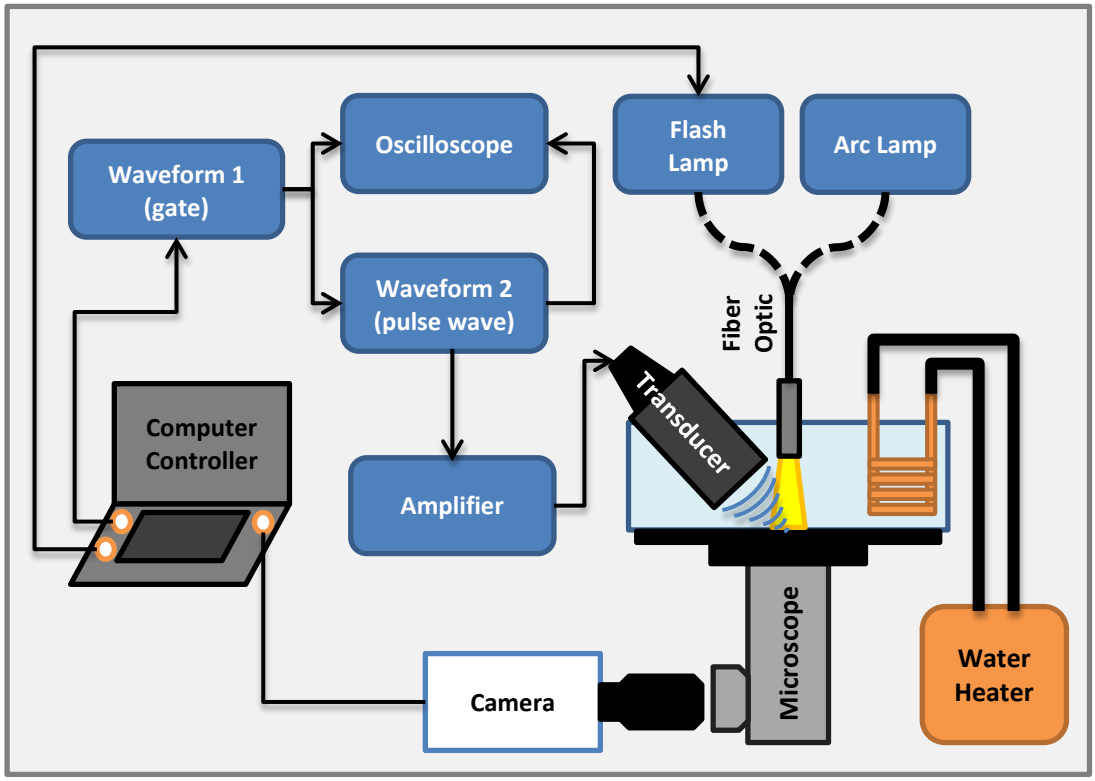

Figure 2. 1: Schematic of the experimental setup. The transducer and light source were oriented confocal with the inverted microscope objective. The ADV event was captured using an ultra-high speed camera through the side port of the microscope. The acoustic pulse was generated using an N cycle pulse from a function generator that was amplified prior to reaching the transducer.

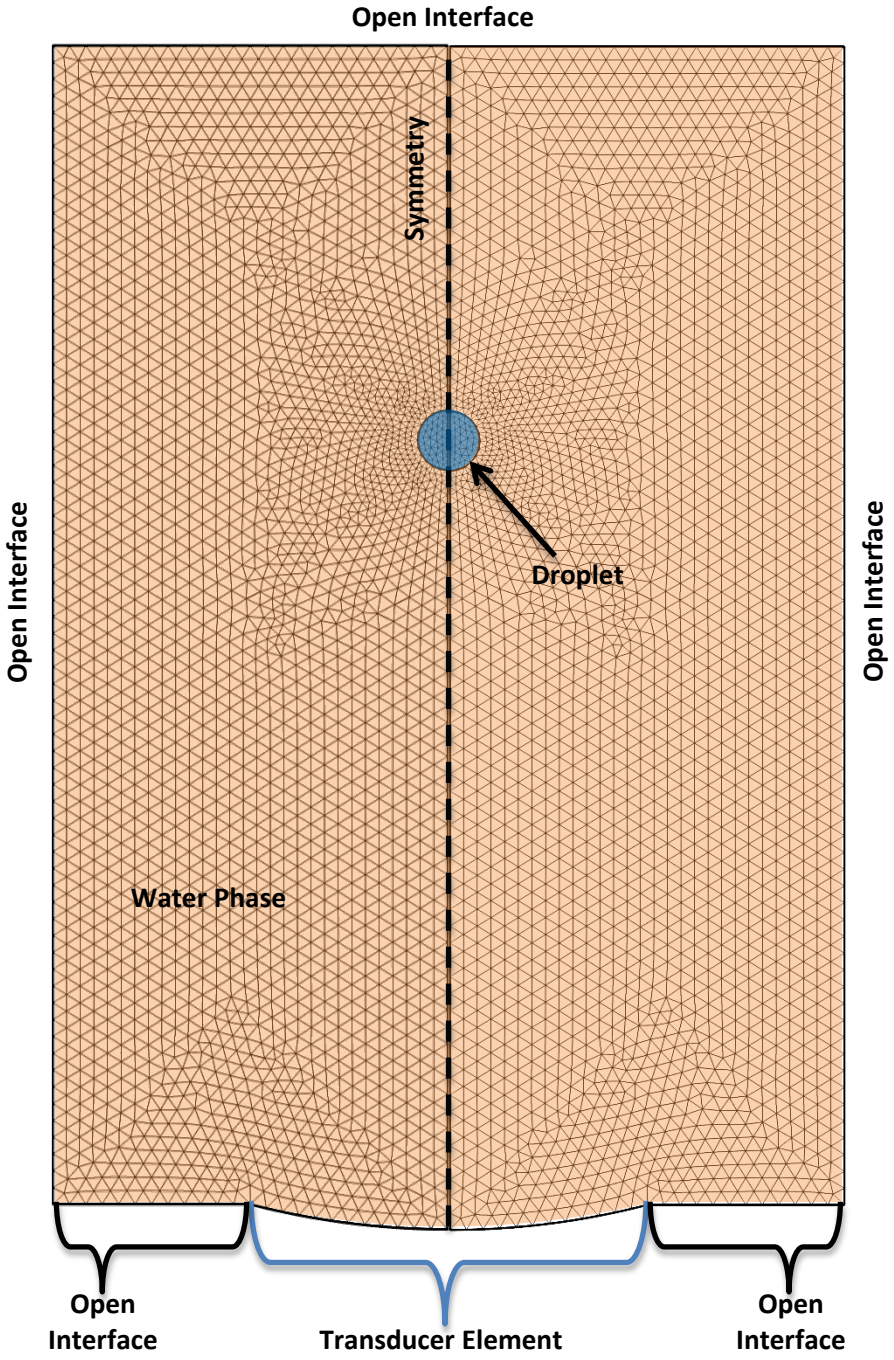

Figure 2. 2: The simulation domain of the transient acoustic model. A PFC droplet was placed the focal point of the transducer. The mesh density shown above was reduced by a factor of 100 and the droplet size was exaggerated for illustrative purposes.

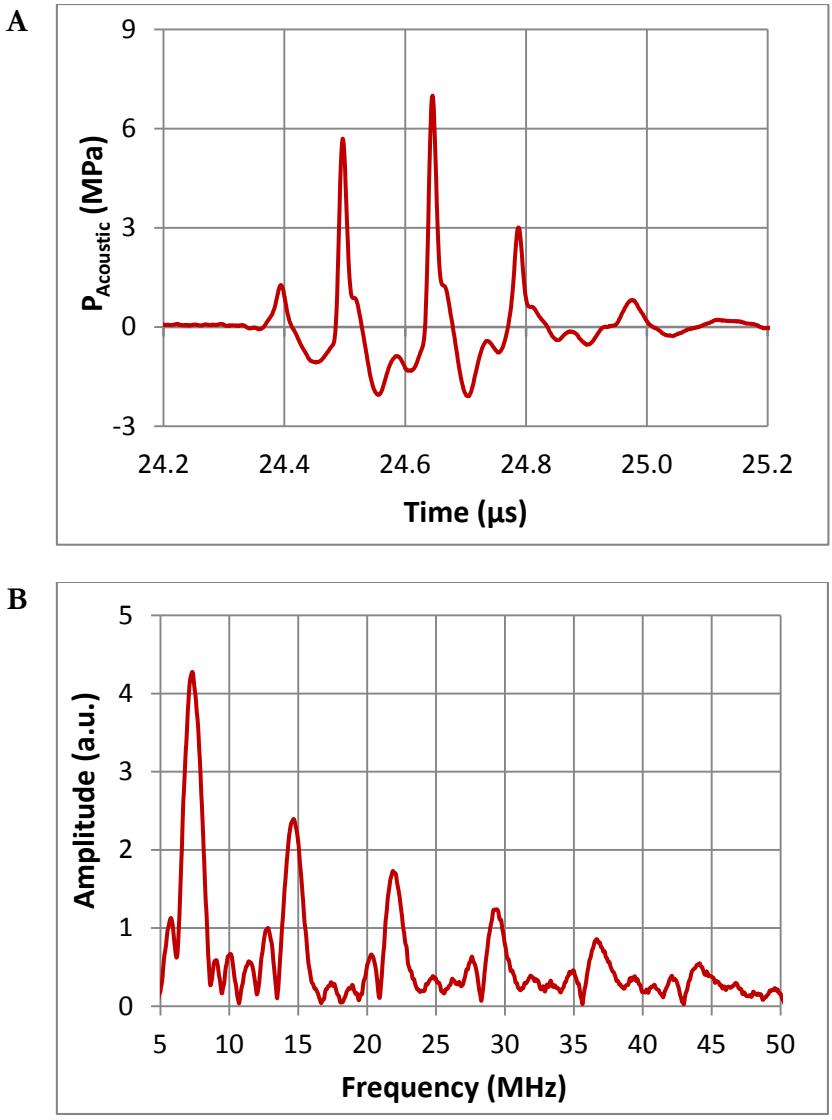

Figure 2. 3: (A) Transient acoustic signal and the (B) frequency response of the 7.5 MHz transducer at the focal point. The power spectrum reveals significant contribution from higher harmonics at the focus. The inset image shows the non-linear acoustic response from a 4 cycle sine input recorded from a fiber optic hydrophone at the focal spot.

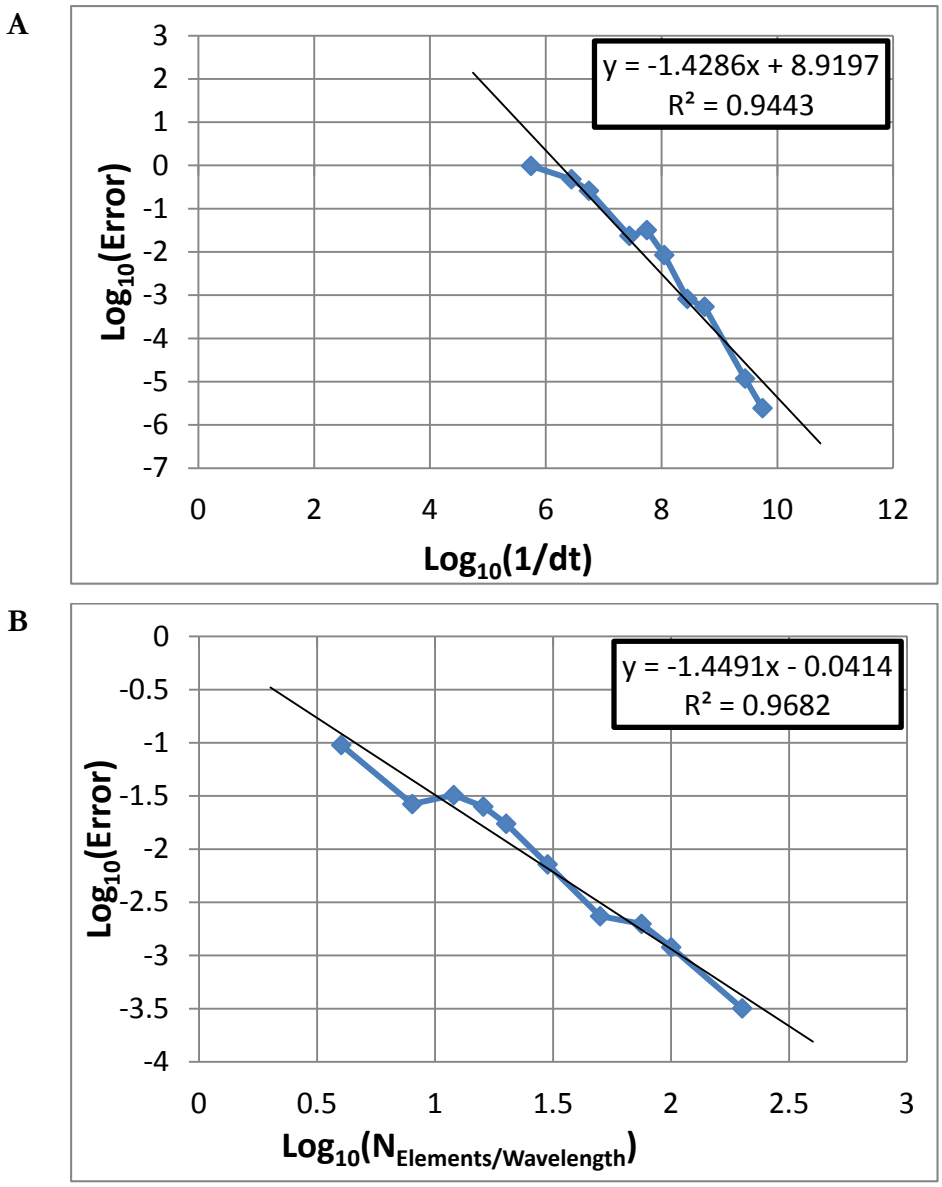

Figure 2. 4: (A) Time convergence and (B) grid convergence of the acoustic finite element model. Both time and grid convergence error reduced at a slope of 1.4.

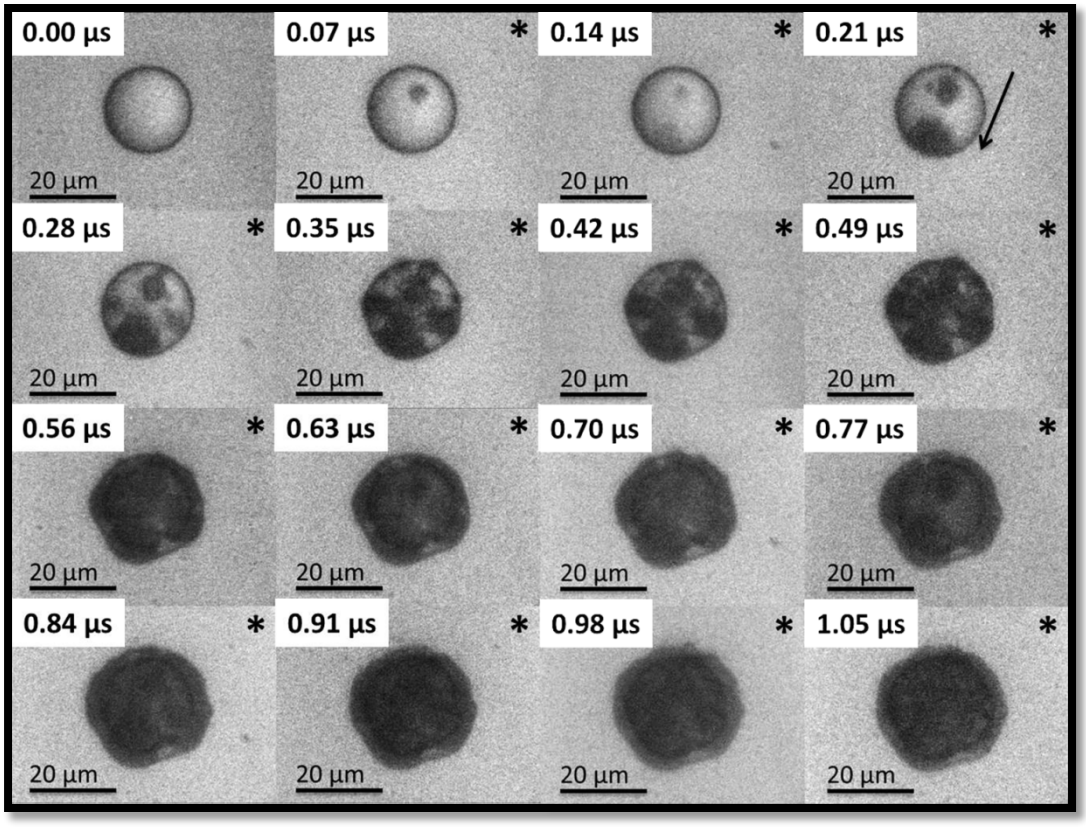

Figure 2. 5: An 18 µm PFC liquid microdroplet undergoing the ADV process due to a single 7.5 MHz pulse of 8 cycles at 3.6 MPa PNP. The "*" indicates the presence of the ultrasound pulse in the field of view and the arrow indicates the direction of the ultrasound wave. Note that the diameter is smaller than the carrier frequency (λ_{DDFP}=54 µm). The primary gas nucleus is formed in the second frame with secondary nucleation sites form in frames 3 and 5 (70 and 210 nanoseconds after the first nucleation side is formed).

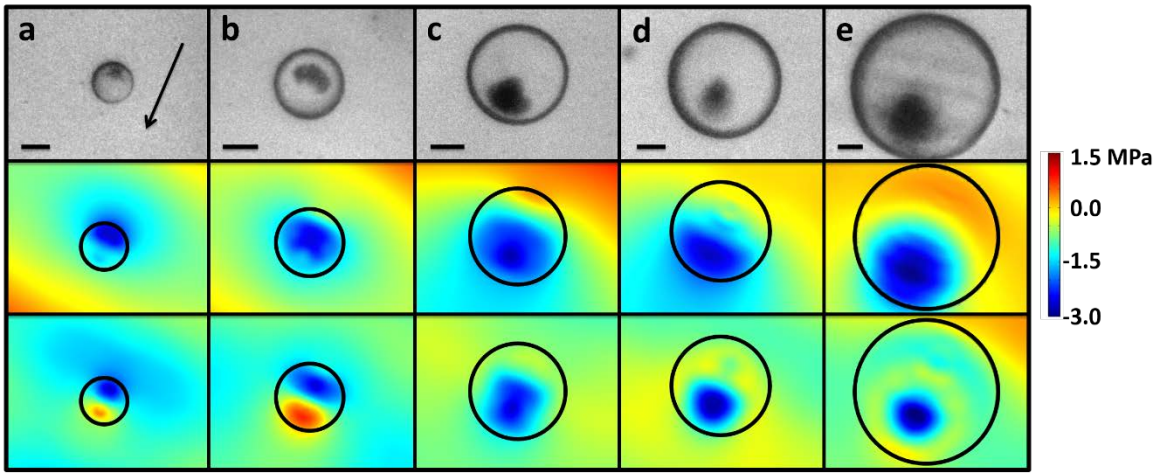

Figure 2. 6: Experimental results of the first nucleation site (top row) versus the simulated pressure field (middle and bottom row) at 7.5 MHz. Image pairs (a-e) represent 14.2, 20.2, 28.5, 41.5, and 60.1 μm diameter droplets and corresponding results. The scale bars indicates 10 μm and the arrow indicates the direction of propagation for the ultrasound wave. The middle row of images are simulation results plotted are when PNP are highest when the propagating acoustic wave travels through the droplet. Blues indicate locations of negative pressure and reds represent positive pressures. The bottom row of images are when the PNP first achieve 80% the maximum PNP.

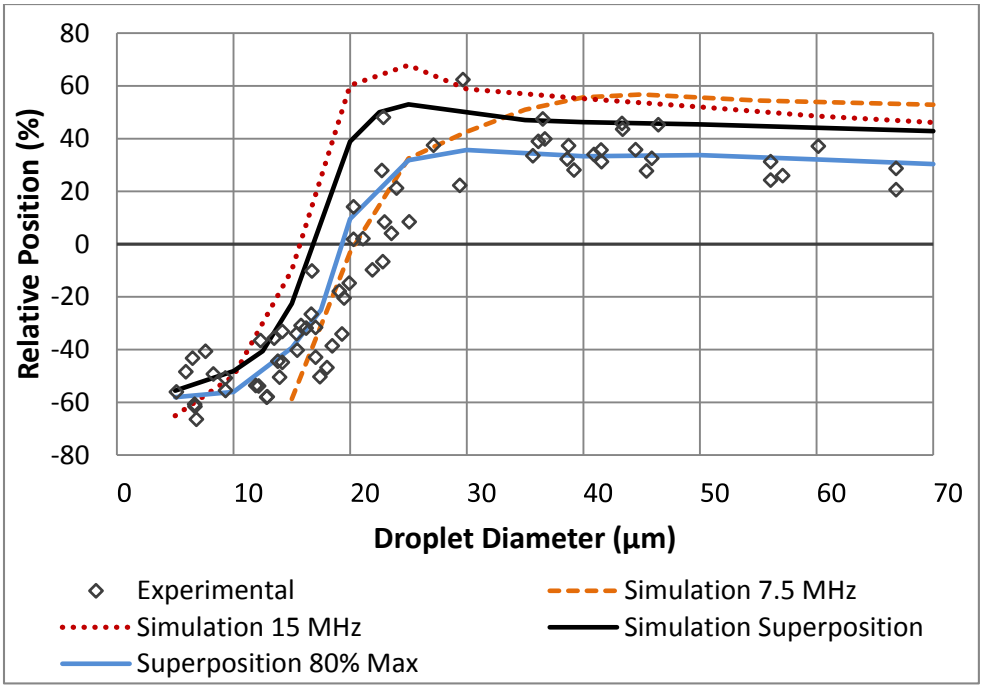

Figure 2. 7: The relative position of the first nucleation site in the microdroplet due to ADV versus simulated results of where the greatest PNP developed along the axis of acoustic propagation. Negative percentages indicates that the center of the first nucleation site formed closer to the transducer while positive percentages indicate formation further from the transducer.

Chapter II: References

[1] O. D. Kripfgans, J. B. Fowlkes, D. L. Miller, O. P. Eldevik and P. L. Carson, "Acoustic Droplet Vaporization for Diagnostic Applications," *Ultrasound in Medicine and Biology,* p. 26(7): 1177–1189, 2000.

[2] O. D. Kripfgans, M. L. Fabiilli, P. L. Carson and J. B. Fowlkes, "On the acoustic vaporization of micrometer-sized droplets," *Journal of the Acoustical Society of America,* pp. 116(1): 272-281, 2004.

[3] J. L. Bull, "Cardiovascular Bubble Dynamics," *Critical Reviews in Biomedical Engineering,* p. 33(4): 299–346, 2005.

[4] V. Vandana, D. J. Rosenthal and A. S. Teja, "The Critical Properties of Perfluoro n-Alkanes," *Fluid Phase Equilibria,* vol. 99, pp. 209-218, 1994.

[5] T. Giesecke and K. Hynynen, "Ultrasound-Mediated Cavitation Thresholds of Liquid Perfluorocarbon Droplets in Vitro," *Ultrasound in Medicine and Biology,* pp. 1359-1365, 2003.

[6] O. D. Kripfgans, C. M. Orifici, P. L. Carson, K. A. Ives, O. P. Eldevik and B. J. Fowlkes, "Acoustic Droplet Vaporization for Temporal and Spatial Control of Tissue Occlusion: A Kidney Study," *IEEE,* pp. 52(7): 1101-1110, 2005.

[7] M. Zhang, M. L. Fabiilli, K. J. Haworth, J. B. Fowlkes, O. D. Kripfgans, W. W. Roberts, K. A. Ives and P. L. Carson, "Initial Investigation of Acoustic Droplet Vaporization for Occlusion in Canine Kidney," *Ultrasound in Medicine & Biology,* pp. 1691-1703, 2010.

[8] M. L. Fabiilli, J. A. Lee, O. D. Kripfgans, P. L. Carson and J. B. Fowlkes, "Delivery of Water-Soluble Drugs Using Acoustrically Triggered Perfluorocarbon Double Emulsions," *Pharmaceutical Research,* p. 2753–2765, 2010.

[9] M. L. Fabiilli, K. J. Haworth, I. E. Sebastian, O. D. Kripfgans, P. L. Carson and J. B. Fowlkes, "Delivery of Chlorambucil Using Acoustically-Triggered Perfluoropentane Emulsion," *Ultrasound in Medicine & Biology,* vol. 36, no. 8, pp. 1364-1375, 2010.

[10] N. Rapopart, K.-H. Nam, R. Gupta, Z. Gao, P. Mohan, A. Payne, N. Todd, X. Liu, T. Kim, J. Shea, C. Scaife, D. L. Parker, E.-K. Jeong and A. M. Kennedy, "Ultrasound-Mediated Tumor Imaging and Nanotherapy Using Drug Loaded, Block Copolymer Stabilized Perfluorocarbon Nanoemulsions," *Journal of Controlled Release,* vol. 153, pp. 4-15, 2011.

[11] P. Zhang and T. Porter, "An In Vitro Study of a Phase-Shift Nanoemulsion: A Potential Nucleation Agent for Bubble-Enhanced HIFU Tumor Ablation," *Ultrasound in Medicine and Biology,* vol. 36, no. 11, pp. 1856-1866, 2010.

[12] P. S. Sheeran and P. A. Dayton, "Phase-Change Contrast Agents for Imaging and Therapy," *Current Pharmaceutical Design,* pp. 2152-2165, 2012.

[13] N. Reznik, R. Williams and P. N. Burns, "Investigation of Vaporized Submicron Perfluorocarbon Droplets as an Ultrasound Contrast Agent," *Ultrasound in Medicine and Biology,* vol. 37, no. 8, pp. 1271-1279, 2011.

[14] D. L. Frost, "Initiation of explosive boiling of a droplet with a shock wave," *Experiments in Fluids,* pp. 8: 121-128, 1989.

[15] Z. Z. Wong, O. D. Kripfgans, A. Qamar, J. B. Fowlkes and J. L. Bull, "Bubble Evolution in Acoustric Droplet Vaporization at Physiological Temperature Via Ultra-High Speed Imaging," *Soft Matter,* 2011.

[16] M. L. Fabiilli, K. J. Haworth, N. H. Fakhri, O. D. Kripfgans, P. L. Carson and J. B. Fowlkes, "The Role of Inertial Cavitation in Acoustic Droplet Vaporization," *IEEE Transactions on Ultrasonics, Ferroelectrics, and Frequency Control,* pp. 1006-1017, 2009.

[17] A. H. Lo, O. D. Kripfgans, P. L. Carson, E. D. Rothman and J. B. Fowlkes, "Acoustic Droplet Vaporization Threshold: Effects of Pulse Duration and Contrast Agent," *IEEE Transactions on Ultrasonics, Ferroelectrics, and Frequency Control,* pp. 933-946, 2007.

[18] O. Shpak, L. Stricker, M. Versluis and D. Lohse, "The Role of Gas in Ultrasonically Driven Vapor Bubble," *Physics in Medicine and Biology,* vol. 58, p. 2523–2535, 2013.

[19] O. Shpak, T. Kokhuis, Y. Luan, D. Lohse, N. de Jong, B. Fowlkes, M. Fabiilli and M. Versluis, "Ultrafast Dynamics of the Acoustic Vaporization of Phase-Change Microdroplets," *Journal of the Acoustical Society of America,* Accepted for publication.

[20] M. M. a. D. F. E.W. Lemmon, "Thermophysical Properties of Fluid Systems," in *NIST Chemistry WebBook, NIST Standard Reference Database Number 69*, Gaithersburg, MD, Febuary 10, 2013.

CHAPTER III: FORMATION OF TOROIDAL BUBBLES DURING ACOUSTIC DROPLET VAPORIZATION

Introduction

Gas embolotherapy is a novel ultrasound based cancer therapy[1,2]. The proposed treatment begins with the introduction of encapsulated liquid perfluorocarbon (PFC) microdroplets via intravenous injection. The PFC is chosen such that at body temperature (37°C) the microdroplets maintains varying degrees of liquid superheat depending on the droplet size and stabilizing surface tension from the shell. Dodecafluoropetane (DDFP, C_5H_{12}) is a commonly used PFC for gas embolotherapy microdroplets with a bulk boiling point of 29°C. DDFP microdroplets have been shown to remain in a stable liquid state even up to 65°C as they do not spontaneously vaporize until a focused ultrasound pulse is applied[3, 4]. After the liquid microdroplets are perturbed and vaporize, they undergo an expansion process to form stable gas bubbles that are approximately 125 times larger in volume than the initial droplets. The resulting bubbles can then lodge in the vasculature, diverting blood flow, and potentially causing tissue damage[5, 6]. This method could be translated into a localized treatment of vascularized tumors. The mechanism in which liquid droplets are vaporized to form gas bubbles using an acoustic pulse can be described as acoustic droplet vaporization (ADV). ADV has also been proposed as a possible platform

for drug delivery, tumor high-intensity ultrasound (HIFU) ablation, and phase-change contrast agents[7-12].

A number of studies have looked at inertial cavitation thresholds for PFC micro- and nano-emulsions[13-15]. However, few studies have directly visualized the dynamics during the initial phase change phase or the initial rapid expansion process. Kripfgans *et al.* 2004 focused primarily on the dynamics initiating vaporization and characterized the threshold dependence between droplet size and acoustic parameters for ADV[3]. Wong *et al.* 2011 experimentally measured the expansion rate of the expanding droplets after vaporization using ultra-high speed imaging[16]. Direct numerical studies related to ADV, carried out by Ye and Bull in 2004 and 2006, looked at the expansion process of bubbles in rigid and flexible channels[17, 18]. Qamar *et al.* 2010 derived a simplified model including the conversion process from liquid to gaseous DDFP in a numerical model, which matched well with experimental results[19]. Recently, Qamar *et al.* 2012 used the earlier simplified model as an initial condition for a full 2D simulation describing bubble expansion in a channel[20]. However, all of the numerical simulations assume that an initial perfectly spherical single bubble nucleus or bubble is formed at the onset of ADV and the bubble remains spherical throughout the first few microseconds. Experimental studies have focused on the events within the first microsecond with nucleation site formation or the expansion process (spanning 600 μs), which may have overlooked important dynamics during the rapid expansion period when stresses are the highest[3, 16, 21, 22]. In this investigation, the goal was to investigate the dynamics of the early time scale events (<5 μs) and observe the dynamics leading into the transition of a liquid PFC droplet to complete conversion to a gas PFC bubble.

Methods

Individual PFC microdroplets (N=112, mean=9.1 μm, and STD =1.2 μm) were isolated at the bottom of an acrylic tank filled with degassed deionized (DI) water maintained at body temperature (37°C) using a heated recirculating pump (HTP-1500, Adroit Medical Systems, Loudon, TN). The PFC microdroplets featured a DDFP (C_5F_{12}, CAS #: 678–26–2) liquid core and an albumin shell. Details on the formulation of the DDFP microdroplets can be found in Kripfgans *et al.* 2000[1]. An inverted microscope (Nikon Eclipse TE2000-S, Nikon, Melville, NY) featuring a 20x objective with 10x internal magnification was used along with an ultra-high speed camera (SIM802, Specialised Imaging Ltd, Hertfordshire, UK) equipped with a 50 mm f/1.4 Nikkor lens reverse mounted to a 70-300 mm Tamron f/4-5.6 macro, providing an addition 1.4x to 6x magnification, giving a field of view on the order of 60x45 μm^2. The ultra-high speed camera was capable of acquiring 16 frames using 8 discreet onboard CCD sensors (1360x1024 pixels) with exposures as short as 5 ns and 5 ns between frames. The ADV process was initiated using a single pulse from a 7.5 MHz single element focused (f/2) transducer (37.5 mm diameter Panametrics A321S, Olympus, Waltham, MA) driven by a function generator (HP 3314A) and a pulse amplifier (Ritec GA-2500-A) gated by a second function generator (Aligent 33120A). In order to supply sufficient light to image the ADV process, the field of view was illuminated using a 300 Joule microsecond flash lamp (Adaptec AD300, Adapt Electronics, Essex, UK) providing 15 μs burst of light. A schematic of the experimental setup is shown in figure 3.1.

Results and Discussion

Approximately 25 μs after the initial triggering of the ultrasound the pressure wave arrived in the field of view initiating the subsequent ADV event (Figures 3.2, 3.3, and 3.4).

In Figures 3.2, 3.3, and 3.4 the first frame shows an 8 μm liquid droplet immediately before vaporization. The ADV process begins with the formation of a single gas nucleation site (Figure 3.2, frame 2) followed by the occasional second nucleus (Figure 3.3, frame 2) along the axis of propagation for the ultrasound. The generation of two gas nuclei on axis with the propagating ultrasound pulse is consistent with previous experimental observations[3, 16]. After nucleation the liquid DDFP continues to convert from liquid to gas phase. Visually, complete transition from liquid to gas for the measured droplet population (9.1 ± 1.2 μm) occurred in under 0.5 μs. Throughout the study, there was no visual indication of external cavitation gas nuclei from the bulk fluid impinging on the microdroplet initiating the ADV process. This suggests that the ADV process as observed here is initiated by dynamics independent from acoustic cavitation of the bulk fluid.

Depending on the acoustic power and the number of cycles, the bubbles immediately after phase change could deform into a bubble torus (Figures 3.2 and 3.4). The toroidal bubble was unable to maintain its shape and quickly pinched off at one end of the torus forming a crescent shape (Figure 3.2, frame 4) and eventually returning to a spherical configuration. A consistent pinch off of the bubble torus was observed along the upper right quadrant of the bubble. This was likely due to the shallow angle of the ultrasound transducer in the tank (25° from horizontal) as well as the propagating direction of the ultrasound (from top to bottom in the images). Typical lifetime of the bubble torus prior to pinch off is on the order of 1 to 1.5 μs with the initial formation of the torus at 1 μs after nucleation. Formation of the torus did not always coincide with the presence of the ultrasound wave (Figure 3.2), suggesting that the dynamics are likely due to residual fluid inertia generated from ultrasound bubble interactions. Similar dynamics have been

previously observed, which includes microjets from cavitation events near boundaries[23-26]. However, unlike inertial cavitation, the bubble does not fully collapse and no rebound events were observed. This could be due to the high internal pressure seen in the PFC gas bubble immediately after phase change resisting collapse from the acoustic pressure. Using the ideal gas law and Laplace's law, it can be estimated that a 9 μm diameter DDFP microdroplet will result in an approximately 45 μm diameter bubble. For such a bubble the resonant frequency is on the order of 145 kHz, therefore it is unlikely that the formation of the torus is due to a bubble resonance[27]. However, the interaction of the field with the gas nuclei is closer to resonance size but with a correspondingly higher internal gas pressure.

The likelihood of collapsing a bubble by creating an invagination to form a toroidal bubble can be modulated by reducing the number of cycles (thus reducing pulse duration) or the acoustic pressure (Figure 3.5). By reducing the pulse duration to 4 cycles, the droplet was still able to undergo the ADV process and the possibility of forming the torus was completely avoided regardless of the pressures tested (2.2-5.1MPa peak negative pressure). Maintaining a low acoustic pressure and varying the pulse length was less effective at mitigating chances of collapsing the bubble. At 2.2 MPa, 4 and 8 cycles were sufficient to vaporize the droplets while avoiding the collapse; however the incidence rate of collapse was greatly increased after 16 cycles. The elevated chances of generating a bubble torus could be from the first several cycles inducing nucleation and phase change over the course of one microsecond (approximately 8 cycles at 7.5 MHz) and later cycles in the longer pulse lengths interacting with the gaseous bubble allowing for collapse.

Recent experiments performed by Seda (2013) have also shown that modulation of acoustic pulse length or pressure can vary the level of cellular injury due to the ADV

process[28]. Experiments using a 7.5 MHz transducer directed at DDFP microdroplets in close proximity to endothelial cells have shown that ADV with increasing pulse length or increasing pressure can denude endothelial cells from the cultured substrate (Figure 3.6). The overall trends seen in the endothelial cell experiment results are consistent with the occurrence rate of bubble torus formation. However a discrepancy between toroid occurrence rate (Figure 3.5) and relative area of cells denuded from the cultured surface (Figure 3.6) was be observed, especially when comparing results when the pulse length was 4 cycles at 7.5 MHz. The differences observed are likely from differences in droplet distribution used. During the bubble toroid occurrence studies a narrow range of droplets diameters centered at 9 μm was used. This is in contrast to the much smaller and broader droplet size distribution used for the cell experiments with a mean diameter on the order of 1 μm. It is possible that the smaller diameter and higher Laplace pressure difference allows for a lower threshold for fluid inertia to develop and eventually cause the bubble torus to form. Depending on the droplet density spot size of the transducer it is likely that the resulting bubble cloud only covers a fraction of the field of view used to measure the lost cell percentage. Because the bubble cloud area grows with increasing pulse length and acoustic pressure but does not exceed the field of view, the relative lost cell percentage in the field of view increases but never reaches 100%.

Although the bubble toroid occurrence rate and percentage of cells lost exhibit similar trends, it remains unclear if the cell damage is due to stresses associated with the bubble torus or the expansion process from ADV. With increasing pressure or pulse length, the bubble cloud size can increase in size causing a large of cells to experience high stresses

from bubble expansion. However, the relative area of bubbles exposed to higher pressures or longer acoustic pulse pressures sufficient to develop the bubble toroid will grow as well.

Conclusions

The conditions necessary to vaporize DDFP microdroplets and collapse the bubble to create a temporary bubble torus at 7.5 MHz were observed. Modulation of acoustic pressure and pulse length allowed for control over the formation of a transient bubble torus. Elevated pulse length or acoustic pressure would lead to eventual torus formation. Associated stresses from invagination of the bubble may lead to potential tissue damage similar to that seen in liquid microjets formed from HIFU bubble collapse[24, 26]. Furthermore, the final pinch off of the bubble torus leading to the eventual reformation of a spherical bubble may also generate high stresses near the endothelium. Such cellular damage has been observed in liquid plug ruptures in the lung airway models may result in sufficiently high stresses leading to epithelial lung damage[29]. However, sufficiently short pulse lengths eliminated the possibility of creating a transient bubble torus over the range of acoustic pressures tested. Additionally it was confirmed that, for the appropriate conditions, single nucleation sites can be formed and the evolution of the expanding bubbles even within the first 10 μs remain largely spherical. This suggests that previous assumptions in computational models are reasonable if acoustic pulses used are low intensity and sufficiently short. The perturbation leading to the temporary formation of a bubble torus could be due to fluid inertia or from acoustic radiation force. Although preliminary results have shown similar correlation between cell injury with increasing pulse length and pressure, it is unclear if this damage is a direct consequence strictly due to the torus formation. Further ultra-high

speed camera ADV experiments must be performed in the proximity of endothelial elucidate when in the time series of events does cell injury occur.

Chapter III: Figures

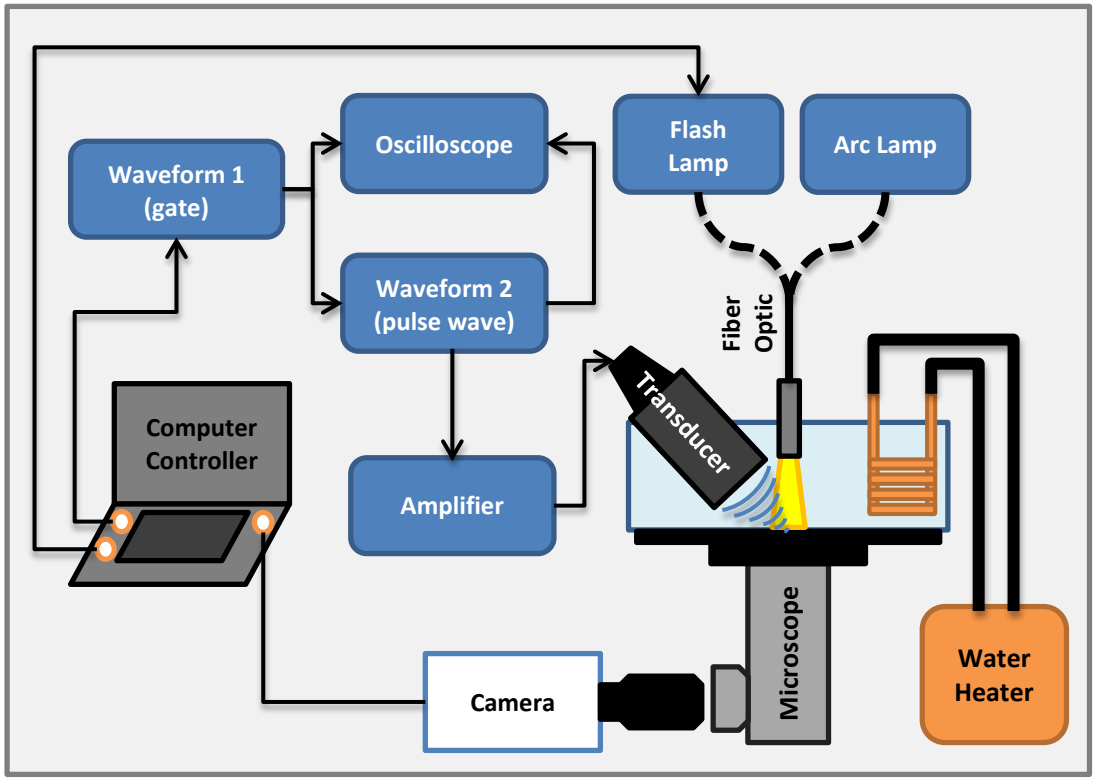

Figure 3. 1: A schematic of the experimental setup. The transducer was held confocal to the microscope objective using a custom machined bracket. Acoustic pulse length and power was modulated from a HP 3314A function generator. Timing between the transducer, amplifier gate, ultra-high speed camera, and flash lamp was accomplished using a laptop equipped with an external controller running SIM Control (Specialised Imaging Ltd, Hertfordshire, UK)

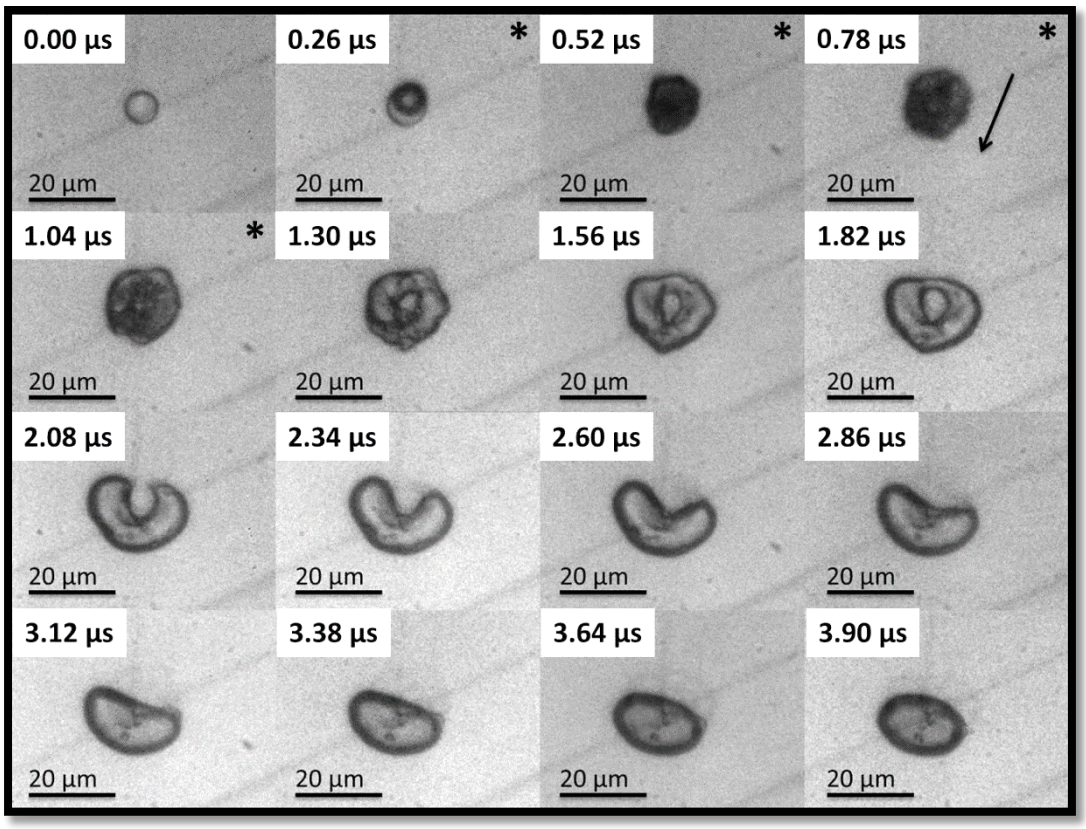

Figure 3. 2: The image sequence shows an 8.3 µm PFC liquid microdroplet undergoing the ADV process initiated by a single pulse of 8 cycles at 7.5 MHz and 3.6 MPa peak negative pressure. The "*" demarcates the presence of the ultrasound pulse in the field of view and the arrow indicates the direction of the ultrasound wave. Visually, perforation of the bubble occurs after the initial nucleation and after the ultrasound wave has passed at approximately one microsecond after the initial nucleus is seen.

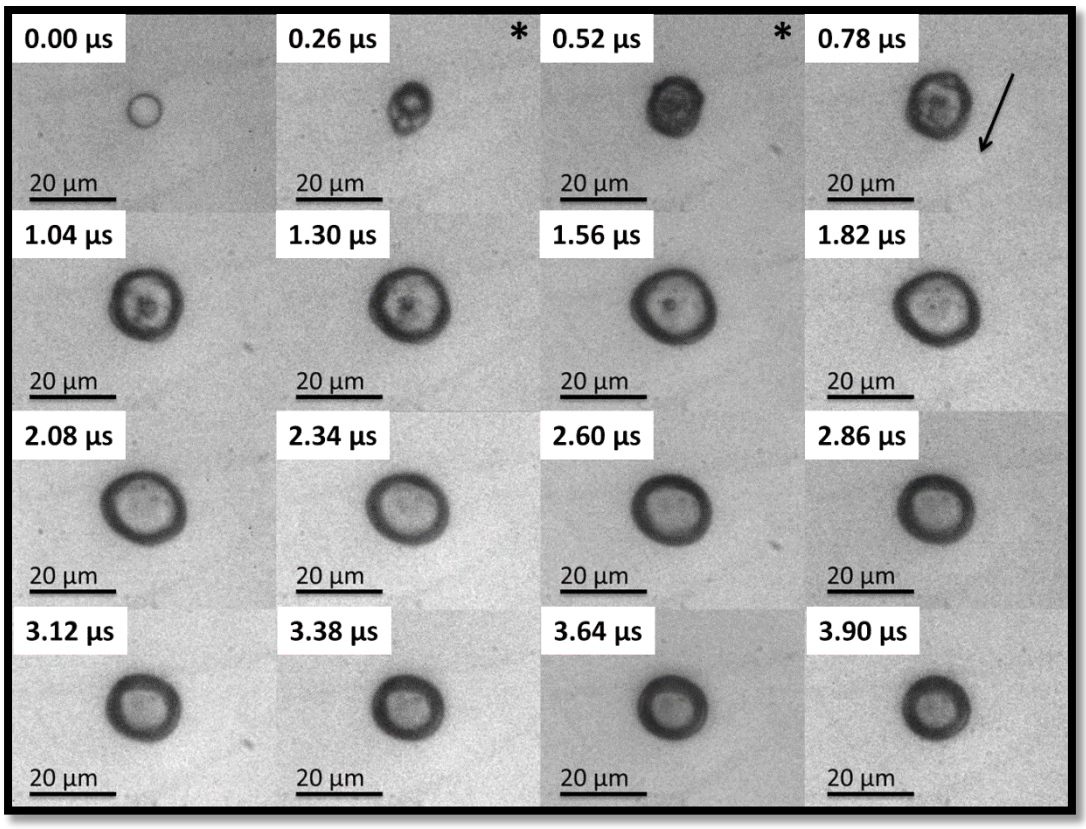

Figure 3. 3: The image sequence shows an 8.3 µm PFC liquid microdroplet undergoing the ADV process initiated by a single pulse of 4 cycles at 7.5 MHz and 3.6 MPa PNP. The "*" indicates the presence of the ultrasound pulse in the field of view and the arrow indicates the direction of the ultrasound wave. The reduction in pulse length suppresses the creation of the bubble torus and the bubble remains largely spherical throughout the early stages of ADV.

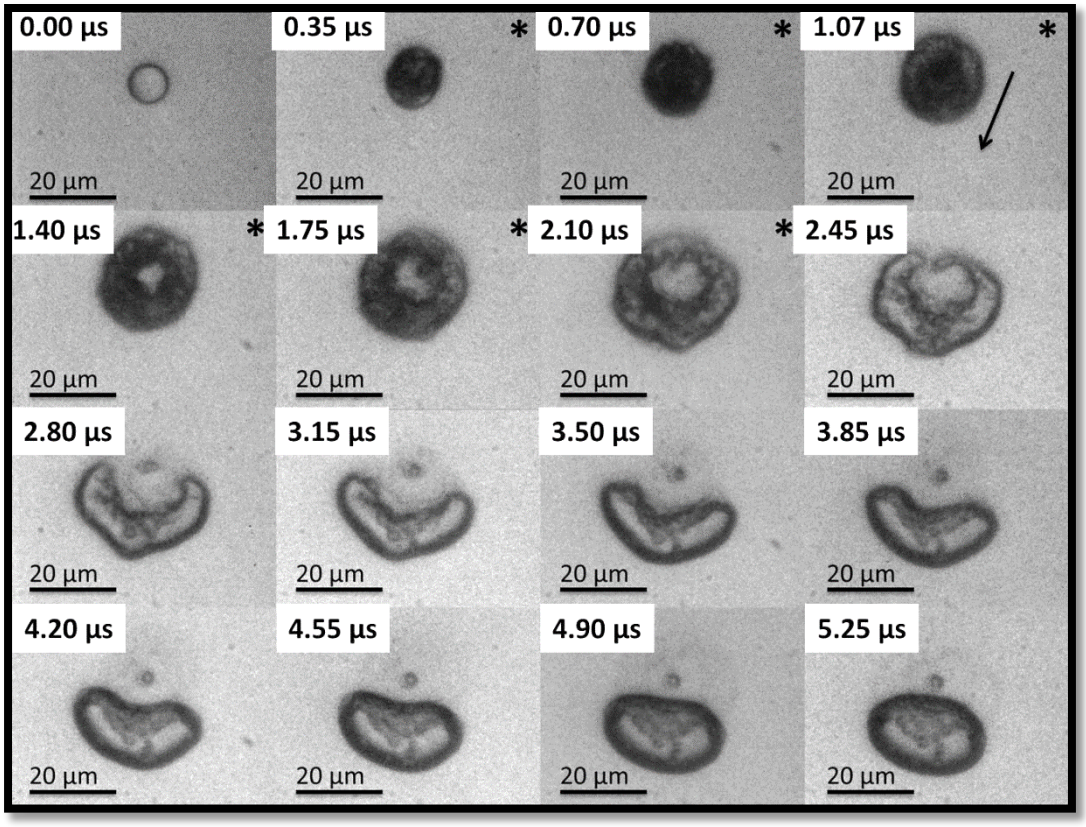

Figure 3. 4: The image sequence shows an 8.5 µm DDFP liquid microdroplet undergoing the ADV process initiated by a single pulse of 16 cycles at 7.5 MHz and 3.6 MPa PNP. The "*" demarcates the presence of the ultrasound pulse in the field of view and the arrow indicates the direction of the ultrasound wave. Visually, perforation of the bubble resulting in a bubble torus is seen approximately one microsecond after the initial nucleation. A combination of elevated pulse length and acoustic pressure results in what appears to be a violent ADV process.

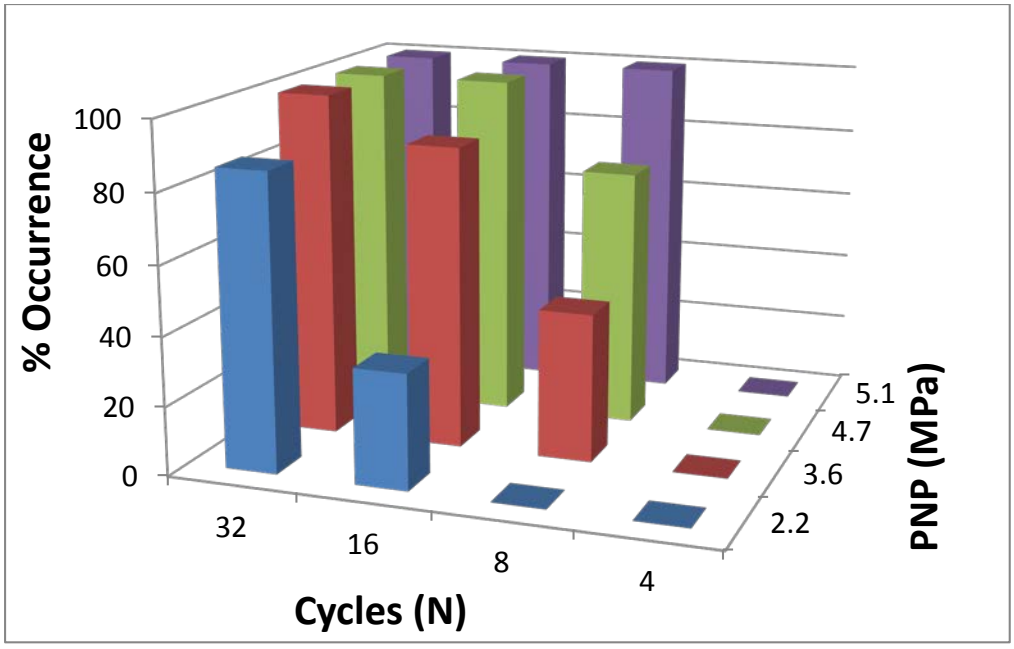

Figure 3. 5: Rate of occurrence observed in bubble torus formation as a function of number of inputted cycles and PNP for droplets of 9.1 μm (STD=1.2 μm) droplets vaporized using single pulses from a 7.5 MHz transducer.

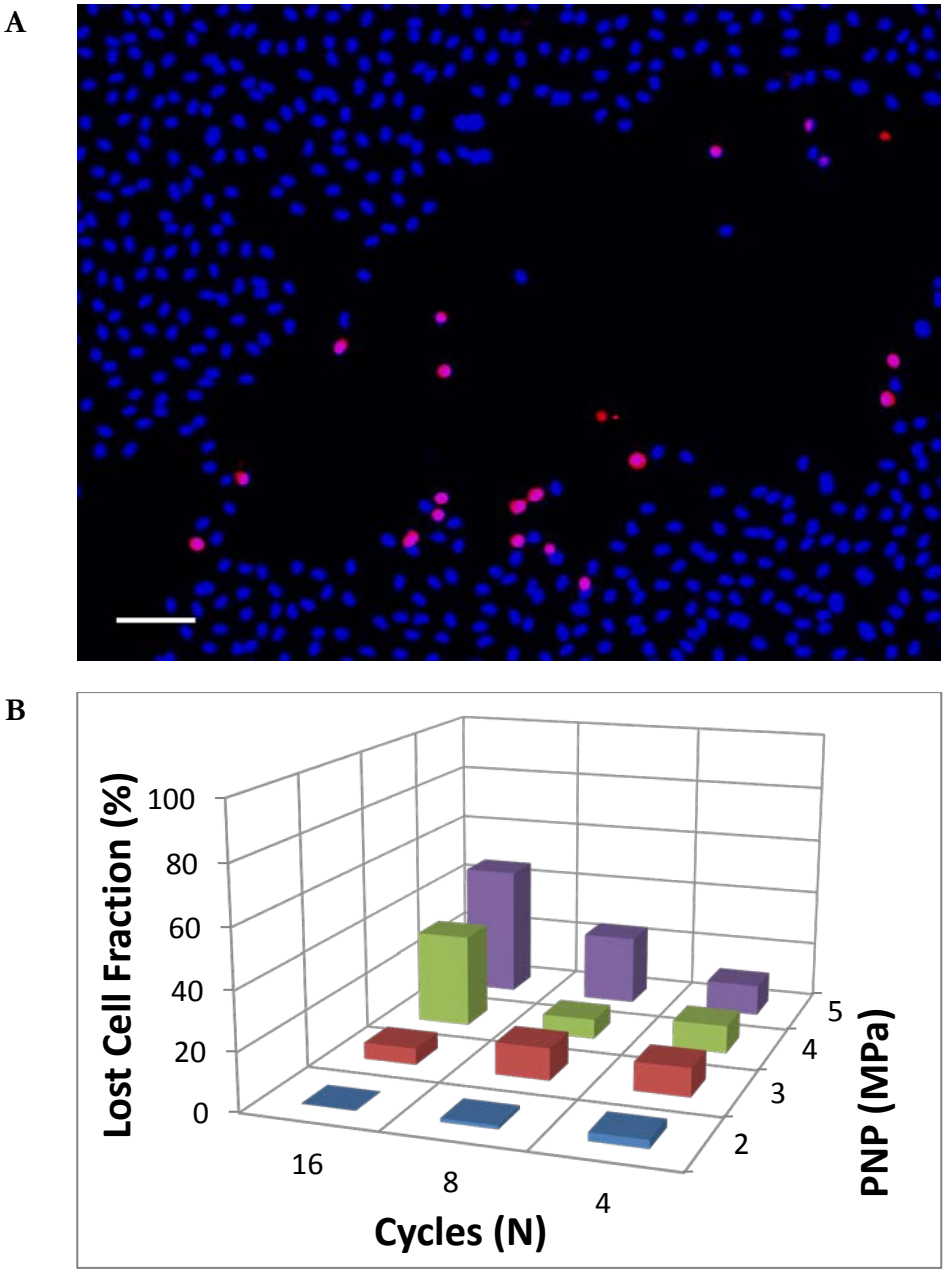

Figure 3. 6: (A) A sample fluorescent image of remaining endothelial cells after ADV and (B) the relative number of cells remaining after ADV (courtesy of Robinson Seda[28]). The blue fluorescence in (A) represent stained nuclei of cells remaining after ADV while the red and blue signify perforated nuclei. The scale bar represents 200 μm. Figure (B) shows that with increasing acoustic power or pulses length there is an increasing number of cells lost in the field of view due to the ADV process.

Chapter III: References

[1] O. D. Kripfgans, J. B. Fowlkes, D. L. Miller, O. P. Eldevik and P. L. Carson, "Acoustic Droplet Vaporization for Diagnostic Applications," *Ultrasound in Medicine and Biology,* p. 26(7): 1177–1189, 2000.

[2] J. L. Bull, "Cardiovascular Bubble Dynamics," *Critical Reviews in Biomedical Engineering,* p. 33(4): 299–346, 2005.

[3] O. D. Kripfgans, M. L. Fabiilli, P. L. Carson and J. B. Fowlkes, "On the acoustic vaporization of micrometer-sized droplets," *Journal of the Acoustical Society of America,* pp. 116(1): 272-281, 2004.

[4] T. Giesecke and K. Hynynen, "Ultrasound-Mediated Cavitation Threshols of Liquid Perfluorocarbon Droplets in Vitro," *Ultrasound in Medicine and Biology,* pp. 1359-1365, 2003.

[5] O. D. Kripfgans, C. M. Orifici, P. L. Carson, K. A. Ives, O. P. Eldevik and B. J. Fowlkes, "Acoustic Droplet Vaporization for Temporal and Spatial Control of Tissue Occlusion: A Kidney Study," *IEEE Transactions on Ultrasonics, Ferroelectrics, and Frequency Controls,* pp. 52(7): 1101-1110, 2005.

[6] M. Zhang, M. L. Fabiilli, K. J. Haworth, J. B. Fowlkes, O. D. Kripfgans, W. W. Roberts, K. A. Ives and P. L. Carson, "Initial Investigation of Acoustic Droplet Vaporization for Occlusion in Canine Kidney," *Ultrasound in Medicine & Biology,* pp. 1691-1703, 2010.

[7] M. L. Fabiilli, J. A. Lee, O. D. Kripfgans, P. L. Carson and J. B. Fowlkes, "Delivery of Water-Soluble Drugs Using Acoustically Triggered Perfluorocarbon Double Emulsions," *Pharmaceutical Research,* p. 2753–2765, 2010.

[8] M. L. Fabiilli, K. J. Haworth, I. E. Sebastian, O. D. Kripfgans, P. L. Carson and J. B. Fowlkes, "Delivery of Chlorambucil Using Acoustically-Triggered Perfluoropentane Emulsion," *Ultrasound in Medicine & Biology,* vol. 36, no. 8, pp. 1364-1375, 2010.

[9] P. S. Sheeran and P. A. Dayton, "Phase-Change Contrast Agents for Imaging and Therapy," *Current Pharmaceutical Design,* pp. 2152-2165, 2012.

[10] N. Rapopart, K.-H. Nam, R. Gupta, Z. Gao, P. Mohan, A. Payne, N. Todd, X. Liu, T. Kim, J. Shea, C. Scaife, D. L. Parker, E.-K. Jeong and A. M. Kennedy, "Ultrasound-Mediated Tumor Imaging and Nanotherapy Using Drug Loaded, Block Copolymer Stabilized Perfluorocarbon Nanoemulsions," *Journal of Controlled Release,* vol. 153, pp. 4-15, 2011.

[11] N. Reznik, R. Williams and P. N. Burns, "Investigation of Vaporized Submicron Perfluorocarbon Droplets as an Ultrasound Contrast Agent," *Ultrasound in Medicine and Biology,* vol. 37, no. 8, pp. 1271-1279, 2011.

[12] P. Zhang and T. Porter, "An In Vitro Study of a Phase-Shift Nanoemulsion: A Potential Nucleation Agent for Bubble-Enhanced HIFU Tumor Ablation," *Ultrasound in Medicine and Biology,* vol. 36, no. 11, pp. 1856-1866, 2010.

[13] M. L. Fabiilli, K. J. Haworth, N. H. Fakhri, O. D. Kripfgans, P. L. Carson and J. B. Fowlkes, "The Roe of Inertial Cavitation in Acoustic Droplet Vaporization," *IEEE Transactions on Ultrasonics, Ferroelectrics, and Frequency Control,* vol. 56, no. 5, pp. 1006-1017, 2009.

[14] A. H. Lo, O. D. Kripfgans, P. L. Carson, E. D. Rothman and J. B. Fowlkes, "Acoustic Droplet Vaporization Threshold: Effects of Pulse Duration and Contrast Agent," *IEEE Transactions on Ultrasonics, Ferroelectrics, and Frequency Controls,* pp. 933-946, 2007.

[15] E. Sassaroli and K. Hynynen, "Cavitation Threshold of Microbubbles in Gel Tunnels by Focused Ultrasound," *Ultrasound in Medicine and Biology,* pp. 1651-1660, 2007.

[16] Z. Z. Wong, O. D. Kripfgans, A. Qamar, J. B. Fowlkes and J. L. Bull, "Bubble Evolution in Acoustric Droplet Vaporization at Physiological Temperature Via Ultra-High Speed Imaging," *Soft Matter,* 2011.

[17] T. Ye and J. L. Bull, "Direct Numerical Simulations of Micro-Bubble Expansion in Gas Embolotherapy," *Journal of Biomechanical Engineering,* pp. 126: 745-759, 2004.

[18] T. Ye and J. L. Bull, "Microbubble Expansion in a Flexible Tube," *Journal of Biomechanical Engineering,* pp. 128: 554-563, 2006.

[19] A. Qamar, Z. Z. Wong, J. B. Fowlkes and J. L. Bull, "Dynamics of Acoustic Droplet Vaporization in Gas Embolotherapy," *Applied Physics Letters,* pp. 143702-1-3, 2010.

[20] A. Qamar, Z. Z. Wong, J. B. Fowlkes and J. L. Bull, "Evolution of Acoustically Vaporized Microdroplets in Gas Embolotherapy," *Journal of Biomechanical Engineering,* pp. 031010(1-12), 2012.

[21] O. Shpak, T. Kokhuis, Y. Luan, D. Lohse, N. de Jong, B. Fowlkes, M. Fabiilli and M. Versluis, "Ultrafast Dynamics of the Acoustic Vaporization of Phase-Change Microdroplets," *Journal of the Acoustical Society of America,* Accepted for publication.

[22] O. Shpak, L. Stricker, M. Versluis and D. Lohse, "The Role of Gas in Ultrasonically Driven Vapor Bubble," *Physics in Medicine and Biology,* vol. 58, p. 2523–2535, 2013.

[23] W. Lauterborn and C.-D. Ohl, "Cavitation Bubble Dynamics," *Ultrasonic Sonochemistry,* vol. 4, pp. 65-75, 1997.

[24] T. Kodama and Y. Tomita, "Cavitation Bubble Bahavior and Bubble-Shock Wave Interaction Near a Gelatin Surface as a Study of in Vivo Bubble Dynamics," *Applied Physics B: Lasers and Optics,* vol. 70, pp. 139-149, 1999.

[25] O. Lindau and W. Lauterborn, "Cinematographic Observation of the Collapse and Rebound of a Laser-Produced Cavitation Bubble Near a Wall," *Journal of Fluid Mechanics,* vol. 479, pp. 327-348, 2003.

[26] H. Chen, X. Li, M. Wan and S. Wang, "High-Speed Observation of Cavitation Bubble Clouds Near a Tissue Boundary in High-Intensity Focused Ultrasound Fields," *Ultrasonics,* pp. 289-292, 2009.

[27] C. E. Brennen, Cavitation and Bubble Dynamics, New York, New York: Oxford University Press, 1995.

[28] R. Seda, *Personal Communication,* Ann Arbor, MI, 2013.

[29] D. Huh, H. Fujioka, N. Tung, R. Paine III, J. B. Grotberg and T. Shuichi, "Acoustically Detectable Cellular-Level Lung Injury Induced by Fluid Mechanical Stresses in Microfluidic Airway Systems," *Preceedings of the National Academy of Science,* pp. 18886-18891, 2007.

CHAPTER IV: THE BUBBLE EVOLUTION FROM ACOUSTIC DROPLET VAPORIZATION IN MICROCHANNELS

Introduction

In recent years there has been increased interest in acoustically activated microdroplets in medicine. The concept behind it is that liquid microdroplets with a bulk boiling temperature below body temperature can be encapsulated such that spontaneous vaporization of the droplets is suppressed through the stabilizing effects through surface tension and can be safely introduced into the bloodstream via intravenous injection into the bloodstream[1-3]. Using an external force such as ultrasound, the droplets can be selectively targeted for vaporization subsequently creating gas bubbles. The process of selectively vaporizing super-heated liquid droplets to form gas bubbles using ultrasound is known as acoustic droplet vaporization (ADV). In gas embolotherapy, the ADV process is applied to perfluorocarbon (PFC) microdroplets to create localized gas emboli near a tumor site in order to starve the tumor from nutrient supply leading to tumor necrosis[1-3].

The ADV process begins with nucleation site formation, which has been suggested to initiate within the droplet as an independent occurrence from inertial cavitation[4-6]. Kripfgans *et al.* 2004 was the first to directly image the ADV process in PFC microdroplets at the microscale, visualizing the nucleation site formation within the droplets and quantifying the relationship between vaporization threshold as a function of droplet size,

frequency, and acoustic power[4]. Wong *et al.* 2011 later looked at bubble evolution of the PFC microdroplets due to ADV carried out in micro-dialysis tubing (D_{tube}=200 μm)[7]. Although the results collected matched well with later theoretical models developed by Qamar *et al.* 2010, the droplet to channel diameter ratios where small and bubbles were unable to make contact with the walls causing bubbles to expansion in a spherical manner[8]. Earlier theoretical work by Ye and Bull in 2004 and 2006 explored bubble expansion in rigid and flexible tubes with bubbles that initially expand radially, but in later stages expand axially because of the confining walls[9, 10]. Without earlier experimental data the model parameters used by Ye and Bull's let to expansion rates were later shown to be an underestimation of the experimentally observed expansion process collected by Wong *et al.* 2011[7]. However, the model still contains useful information behind behavior of ADV in highly confined conditions leading to bubble-wall contact. The flexible wall model developed by Ye and Bull in 2006, predicted that depending on the level of vessel resistance, significant vessel deformation to the point of vessel rupture may occur.

Samuel *et al.* 2012 was able to perform ADV and verify the bubble lodging patterns in rat cremaster vasculature[11]. These results were consistent with predicted lodging configurations initially proposed by Calderon *et al.* 2006[11]. Furthermore, Samuel *et al.* 2012 provided case evidence of capillary damage in the form of RBC extravasation due to ADV exposure[11]. Based on the imaging evidence it was unclear to conclude if the damage was due to inertial cavitation or stresses related to bubble expansion[11]. In an effort to resolve expansion rates and gain insight on the potential sources of damage, this study focused on comparing the expansion rates from the ADV process in free field environments versus idealized polydimethylsiloxane (PDMS) microvessels.

Methods

Two experimental conditions were tested: vaporization of PFC microdroplets in free-field conditions and vaporization in idealized microvessels. ADV events were recorded for 41 cases in free-field, 34 cases for 25 μm diameter, 36 cases for 50 μm diameter channels, and 28 cases in 100 μm diameter channels. During both sets of experiments liquid PFC microdroplets featuring a dodecafluoropentane (DDFP, C_5F_{12}, CAS No. 678–26–2) core and an albumin shell were isolated and vaporized using focused ultrasound. The DDFP droplets were constructed using an amalgamator and details on the procedure to produce the droplets can be found in Kripfgans *et al.* 2000[3]. In both experiments single pulses from a single element focused (f/2) transducer at 7.5 MHz (Diameter=37.5 mm, Panametrics A321S, Olympus, Waltham, MA) using 8-32 cycles at 2.2 to 5.6 MPa peak-negative pressure (PNP) were used to initiate vaporization. All experiments were performed in a degassed deionized water bath held at body temperature (37°C) using a recirculating temperature closed circuit water pump (HTP-1500, Adroit Medical Systems, Loudon, TN). Driving the transducer was a pulse amplifier (Ritec GA-2500-A) gated by function generator function generator (Aligent 33120A). The sine wave input amplified by the pulse amplifier was produced using an arbitrary waveform generator (HP 3314A). In order to capture the events of the rapidly expanding vapor bubbles an ultra-high speed camera (SIM802, Specialised Imaging Ltd, Hertfordshire, UK) attached to the side camera port of an inverted microscope (Nikon Eclipse TE2000-S, Nikon, Melville, NY) was used. On the inverted microscope 4x, 10x, and 20x objectives were used combined with a 10x internal magnification from the microscope. Paired with the ultra-high speed camera was a 50 mm f/1.4 Nikkor lens reverse mounted to a 70-300mm f/4.5-5.6 Tamron tele-macro zoom lens providing an addition 1.4-6x

magnification. Because of the short exposures and high magnification, one of two flash lamps paired with a fiber optic bundle to redirect the light to the field of the view. A 300 Joule microsecond flash lamp (Adaptec AD300, Adapt Electronics, Essex, UK) was used for imaging sequences occurring within 15 μs whereas a 500 Joule millisecond flash lamp (Adaptec AD500, Adapt Electronics, Essex, UK) was used for vaporization events occurring within two milliseconds. A schematic of the experiment setup can be seen in figure 4.1.

The straight microchannels representing idealized 25, 50, or 100 μm microvessels with a channel length to width ratio of 50:1 were constructed out of molded PDMS (Sylgard 186, Dow-Corning) mixed at a 10:1 elastomer to cross-linker ratio and plasma bonded to glass slides (Fisher Scientific) using oxygen and the RIE-2000 (South Bay Technology, Inc. San Clemente, CA, USA). The PDMS molds were constructed using standard photolithographic techniques using SU-8 2015 for the 25 μm channels, SU-8 2025 for the 50 μm, and SU-8 2075 for the 100 μm channels (MicroChem, Newton, MA, USA) on a silicon substrate (University Wafer, Boston, MA, USA)[13, 14]. The procedures used for mold manufacturing can be found in Appendix I. In order to minimize attenuation from the PDMS layer of the channel, the PDMS was degassed, dispensed at 4 ml volumes, and spun (WS-400-6NPP, Laurell Technologies Corp., North Wales, PA, USA) onto the molds to give approximately 75 μm wall thicknesses. Details on the procedures for obtaining specific wall PDMS wall thickness can be found in Appendix II. A biopsy punch was used to create openings to introduce the droplets and droplets were introduced individually using a 1 ml syringe.

Results and Discussion

In both free-field and channel confined conditions approximately 25 μs after initial triggering of the ultrasound, the ADV process began in the microdroplet by forming the first nucleation site (Figure 4.2). The time delay was expected considering the focal length and speed of sound in water. A negligible time difference was expected between the channel confined vaporization and the free-field case because the wall thickness was thin relative to the focal length creating little change to the time of flight for the acoustics. The beginning of ADV always began with an initial gas nucleus forming within the droplet and on many occasions a second nucleation site forming within the droplet within 100 nanoseconds after the first nucleation sites formed. When two nucleation sites are formed they consistently form in line with the axis of propagating acoustic wave, which is consistent with findings from previous studies[4, 7]. The presence of microchannel walls had no effect on the formation of the nucleation sites. This observation did not come as a surprise because the channel dimensions were smaller than the wavelength in water and standing waves should not have been presence in influencing nucleation site formation. After the first nucleation sites form the liquid DDFP continues to convert to its gas phase by feeding into the gas nucleation sites until a high-pressure gas bubble is formed, usually on the order of one microsecond after nucleation has occurred.

The observed pattern of nucleation sites forming in line with the axis of acoustic propagation suggests that the ADV process is initiated by the acoustic wave interacting with the droplet. Previous experimental observations investigating location of the primary nucleation site formed due to ADV is due to lensing effect of the acoustic wave within the droplet causing a high peak negative pressure to develop within the droplet[15]. A possible

explanation for the secondary gas nuclei formed can be borrowed from Frost 1989, looking at shock-induced explosive boiling, who concluded that a second pressure wave released from the first nucleation site is refocused on the opposing side of the droplet[16]. Considering the sound speed in DDFP is 406 m/s[17], the time of flight for a pressure wave to propagate across the droplets 10-12 microns in diameter (Figure 4.2) should be 25-30 nanoseconds. However, the first visible indication of the second nucleation site forming in figure 4.2 is 100 nanoseconds after formation of the second nucleation. Although Frost's explanation does not fit perfectly with the results shown, it does not rule out the possibility that additional acoustic interactions from the propagating ultrasound pulse could be augmenting the field within the bubble, interacting with possible pressure waves from the first nucleation site, and causing the second nucleation site to form.

Once the high pressure gas bubble was formed, the bubble underwent a rapid expansion. It was observed that in during the free-field cases the bubble takes on an irregular shape that is non-spherical (Figures 4.3 and 4.5). Similar observations were made by Wong *et al.* 2011 when the vaporization took place in 200 μm diameter channels[7]. Once vaporization and expansion events were constrained to the microchannels, the bubbles remained much more spherical in shape, until wall contact (Figures 4.4 and 4.5). Under extreme acoustic conditions, when either acoustic power or acoustic pulse length is increased bubble toroids have been shown to form regularly in free-field conditions[15]. However, ADV constrained by a channel prevent these toroid bubbles to form (Figure 4.5). Numerical studies performed by Ye and Bull 2004 and 2006[9, 10] as well as with Qamar *et al.* 2010[8] investigating bubble expansion in channels all have concluded that channel diameter plays a significant role in damping bubble expansion due to viscous resistance from the

channel. Therefore, it is likely that the inability to pull fluid into the domain to deform the bubble and create the depression leading to toroidal bubble configurations is likely from viscous resistance from small channel diameters. The previous study's observations of non-spherical bubbles during the rapid expansion are likely due to the larger channel to droplet diameter ratio used.

The interface and effective volume of the bubble could be tracked as the bubble expanded over time. An image contrast threshold based method (using MATLAB) was used to identify and estimate the bubble dimensions in the ultra-high speed images. An effective radius was calculated by measuring the visualized area of the bubble in the images, projecting it to an estimated spherical or cylindrical volume (depending on vaporization conditions), and back-calculating an equivalent spherical volume. For bubble expansion in a channel, it was assumed that up until wall contact the expansion was in the radial direction and in later time points assumed to expand cylinder as a lengthening cylinder. In figure 4.7, the effects of viscous resistance from the channel on bubble expansion are evident. During free-field expansion between 17 and 25 μs the bubble is close to the equilibrium diameter (Figure 4.4). Looking at a similarly sized droplet (Figure 4.5) expanding in a channel, 25 μs after onset of ADV the bubble continues to expand and does not reach equilibrium until 75 μs after ADV first begins. The vaporization events in channels can be separated into two conditions, bubbles that contact the wall and continue to expand in a cylindrical fashion and moderately sized bubbles that remain spherical throughout the vaporization process (Figure 4.7). Comparing the wall contact and no wall contact results to the free field ADV results, it can be concluded that as the relative diameter of the channel increases compared to the droplet

diameter, viscous resistance from the presence of the channel walls diminishes and the bubble expansion rates increase.

The greatest expansion rates occurred during the initial microseconds of bubble expansion follow immediately after the initial phase change. According to Wong *et al.* 2011 the initial rapid expansion is driven by the high internal pressures of the newly converted gas bubble. During the early stages of the expansion, up until the bubble reaches an expansion ratio of 1.5 or during the 1.5 μs, maximum expansion rates are achieved. During that initial period, the maximum expansion rate is maintained at a constant rate and can be approximated through a linear model[7]. A linear model was used during to estimate the maximum expansion rates for the free-field condition over the course of the first 1.5 μs. Because of the much slower expansion rates observed during the channel constrained expansion the definition of linear expansion up until an expansion ratio of 1.5 was used to estimate the constant maximum expansion rates achieved during the expansion in constrained channels. Subsequent time points for the free-field and channel constrained expansion deviated from the projected linear model and therefore were omitted from the linear model. The two droplet populations observed had a mean diameter of 7.2 μm (STD=0.52 μm) for free-field vaporization and 8.0 μm (STD=0.58 μm) for the channel case. The resulting linear regressions revealed an estimated interface velocity of 7.96 m/s during free field conditions and 0.57 m/s during expansion in a channel. Using conservation of mass and assuming that bubble remains spherical during free field expansion, the radial stress component given by:

$$\sigma_{rr} = -\frac{4\mu R_b^2}{r^3} V_b \tag{1}$$

Where μ is viscosity, r is radial position, R_b is the bubble radius, and V_b is the velocity of the bubble interface during expansion. The stress component clearly decays to zero and damage would likely be limited to areas immediately next to the expanding bubble. Alternatively, if it is assumed that a bubble remains spherical in the early stages of expansion in a channel, a wall shear is experienced throughout the channel due to the displaced volume of fluid. Depending on the bubble and vessel dimensions an estimate for the limit of wall shear experienced far from the bubble during the spherical expansion can be expressed by:

$$\tau_{wall} = -\frac{8\mu}{R_v}\left(\frac{R_b}{R_v}\right)^2 V_b \tag{2}$$

where R_v the radius of the bubble. In the limit that the bubble expands at the same interface velocity as the free-field case and the bubble radius matches the vessel radius, the entire vessel will experience a wall shear equal if not greater than the two times the stress normally experienced at the gas/fluid interface of an equivalently sized bubble in free-field. The finite limit of stress that is observed in an entire vessel branch during ADV exposure could potentially explain the vessel damage and RBC extravasation observed by Samuel *et al.* 2012[11]. Clinically, so long as the droplet populations are designed to be small compared to the intended ADV exposed vessel, the level of stresses imposed on the vessel can be suppressed.

Conclusions

The nucleation events in addition to bubble expansion events under both free-field and microchannels constrained ADV conditions were observed. It was found that the pattern in nucleation site formation was in good agreement with previous studies. The effects of the presence of channel walls were observed in two ways during the expansion

process. First, the presence of the channel walls ensured the bubble remain spherical throughout the early stages of the expansion process. Previous experimental results elucidating conditions that ensured bubble collapse creating toroidal bubbles in free-field conditions could not be reproduced when constrained in a microchannel[18]. Furthermore trends first predicted from numerical models suggesting that the presence of the channel would result in a dampening effect on bubble expansion were observed experimentally. Although the bubble expansion is slower, there is still a possibility that stresses developed stresses along the entirety of the vessel may result in possible vessel damage. Fortunately the expected levels of wall shear diminish with decreasing droplet diameter versus vessel diameter during expansion. By using select droplet populations that are smaller than the intended insonation vessel diameter, stresses from ADV expansion can be mitigated. Additional work quantifying cellular damage due to ADV in small vessels must be performed in the future in order to understand the safety limitations of gas embolotherapy applied to microcirculation.

Chapter IV: Figures

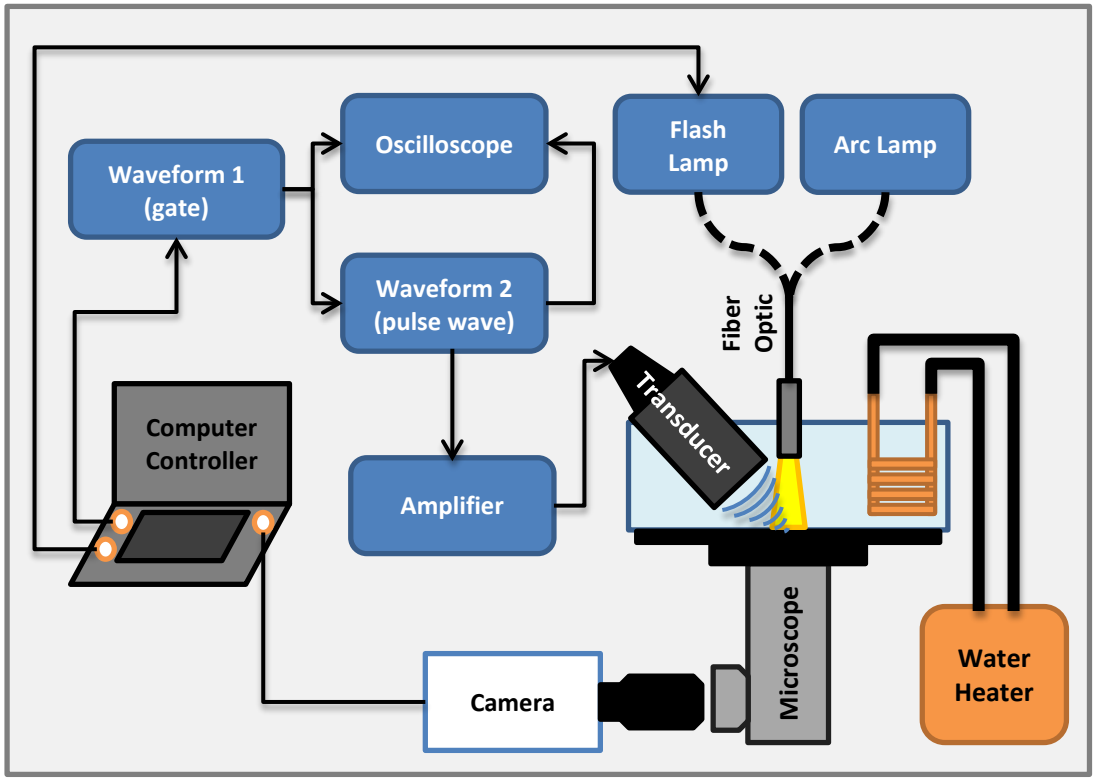

Figure 4. 1: Vaporization events occurred in a degassed DI water bath held at body temperature using a recirculating water heater. The vaporization event was activated through the triggering of a single element 7.5 MHz transducer driven by a pulsed amplifier fed by an N cycle sine wave from a function generator both gated by a second waveform generator. A laptop was used to synchronize triggering of the acoustics along with an ultra-high speed camera and flash lamp.

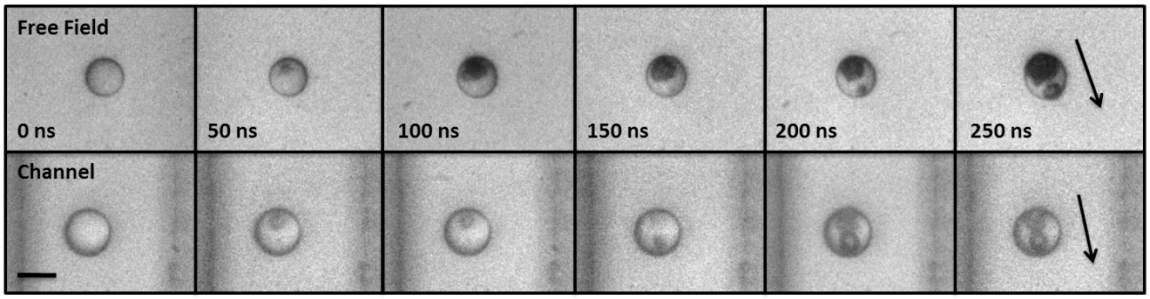

Figure 4. 2: Nucleation process observed in free field conditions (top row) versus constrained in a channel (bottom row). The arrows indicate the direction of propagation of ultrasound. The scale bar represents 10 μm.

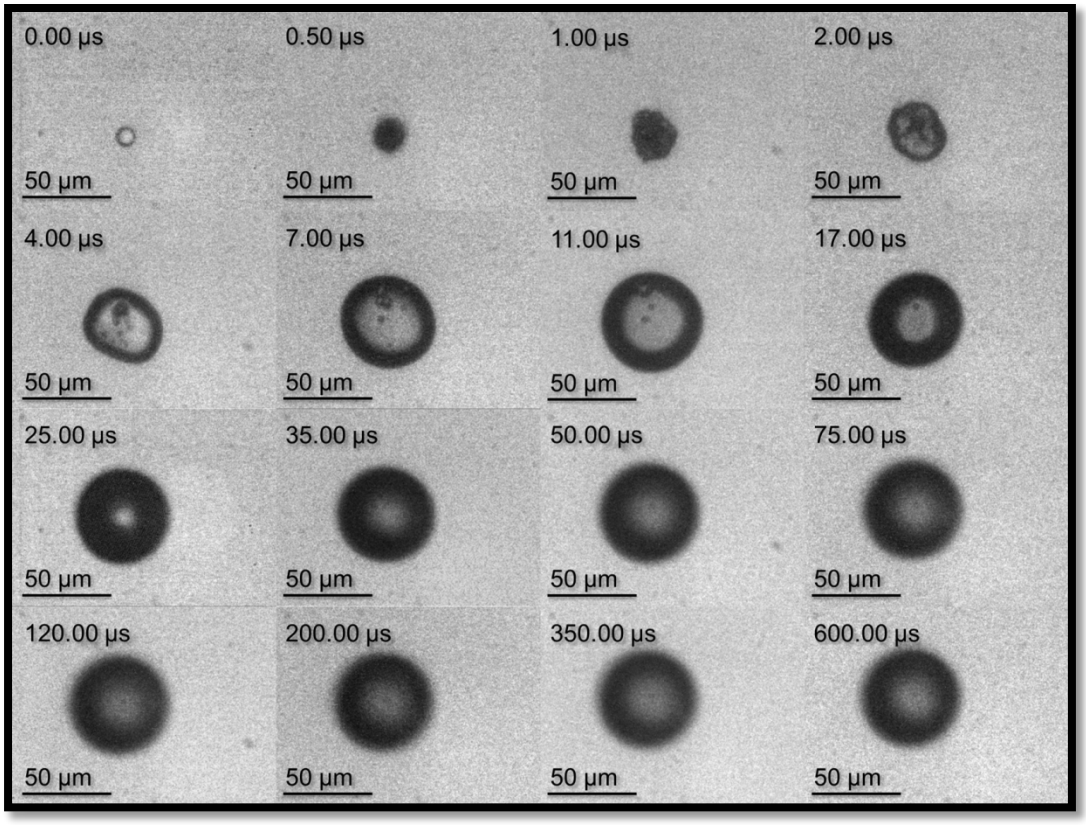

Figure 4. 3: The expansion process in free field conditions for an 11.3 µm diameter microdroplet. At time zero an isolated PFC microdroplet is seen prior to the ultrasound pulse arrives (8 cycles at 7.5 MHz and PNP = 3.9 MPa). The ultrasound is present over the first microsecond and 0.5 µs into the ADV process it appears that all the DDFP liquid is converted to the gas phase. Between times 1.0 to 4.0 µs bubble interface is non-spherical, but begins to returns to spherical shape 7 microseconds in. By 25 µs most of the expansion is complete and the interface blurs because the bubble interface begins to leave the plan of focus.

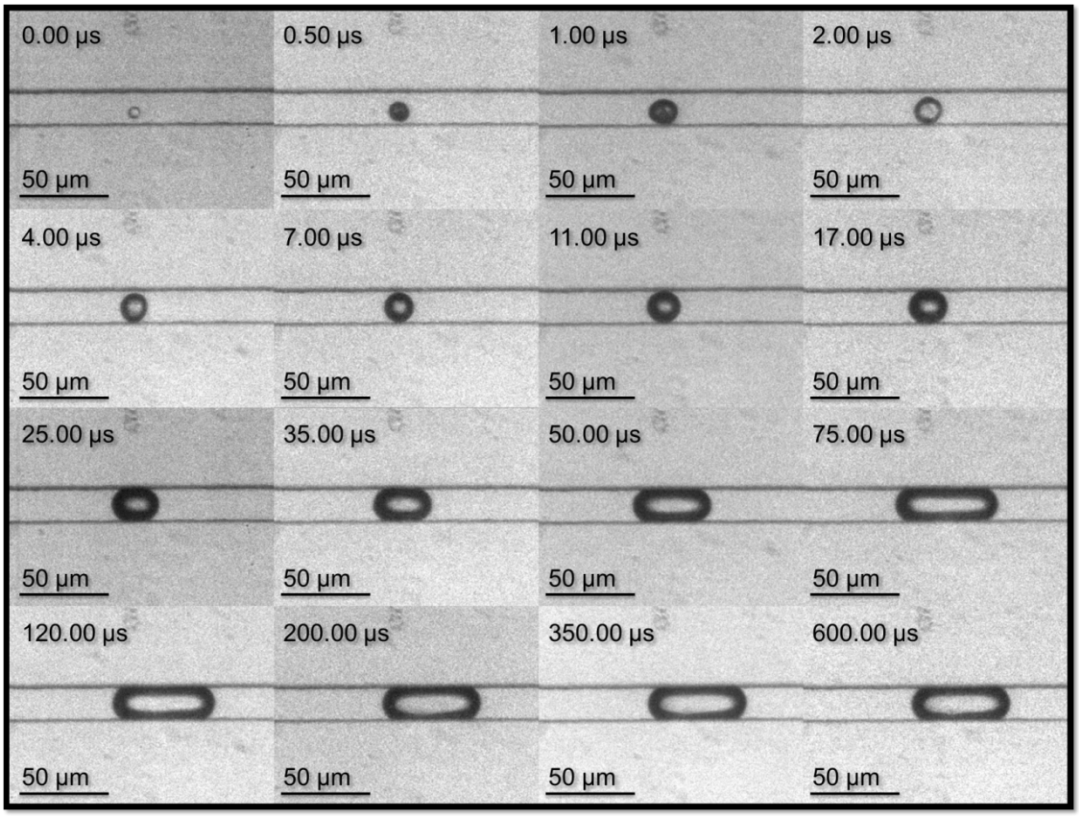

Figure 4. 4: The expansion process of an 8.4 micron diameter microdroplet within a 25 µs diameter channel. At time zero the droplet is just before initiation of the ADV process. Immediately afterwards the ultrasound pulse arrives (8 cycles at 7.5 MHz and PNP= 4.3 MPa) and remains on through frame 3 (1 µs). In frame 2 (0.5 µs) the DDFP liquid is converted to gas phase. Throughout the earlier times of the expansion process, before contacting the walls, the bubble remains largely spherical. However, once the bubbles contacts the walls the bubble continues growth axially in line with channel ad no wall deformation is apparent.

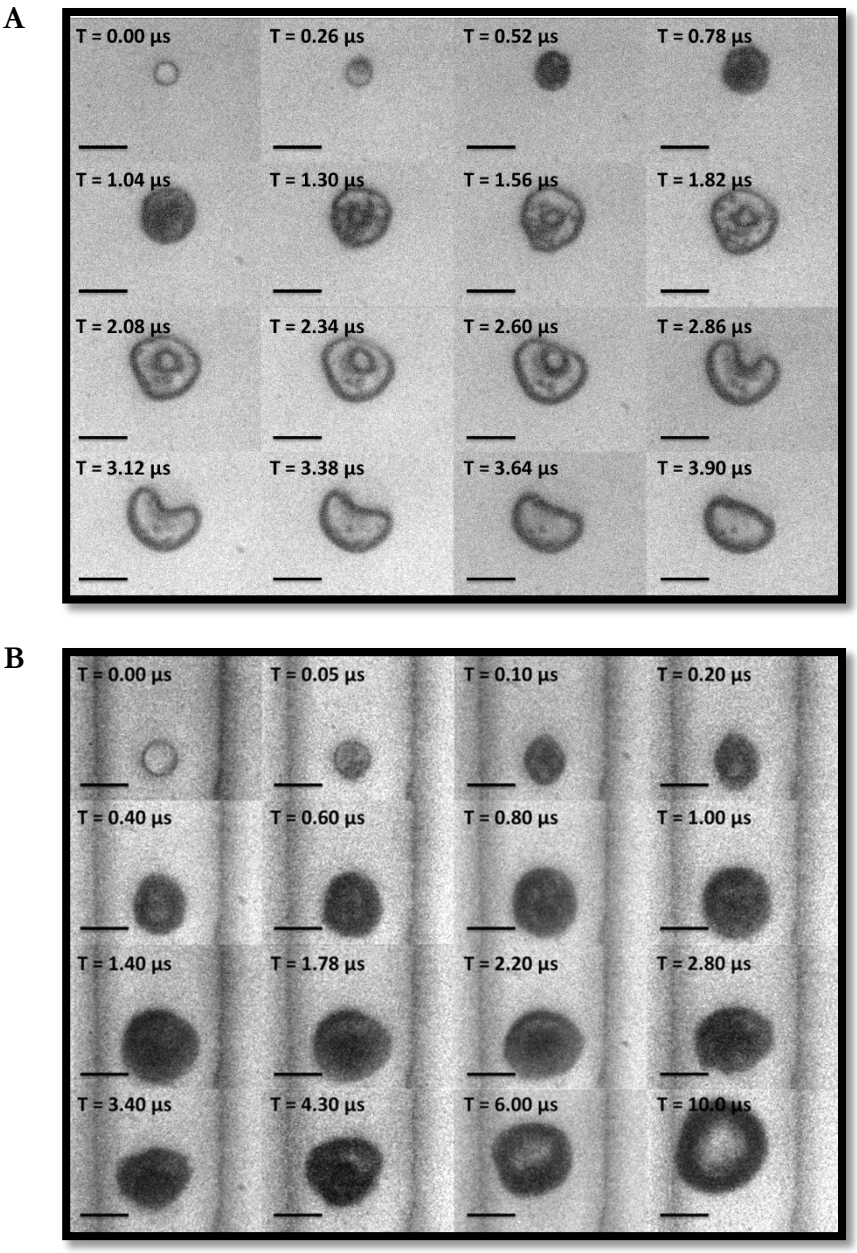

Figure 4. 5: The vaporization process under acoustic conditions that result in toroidal bubbles during free-field expiation. Figure (A) shows an 11.4 µm droplet undergoing expansion to form the toroidal bubble due to a 3.6 MPa PNP pulse at 8 cycles. Figure (B) shows a 13.9 µm droplet undergoing expansion in a 50 µm channel due to a 5.1 MPa PNP pulse at 32 cycles. The resulting bubble is unable to deform to form the toroidal bubble due to viscous resistance from the channel. The scale bars represents 20 µm.

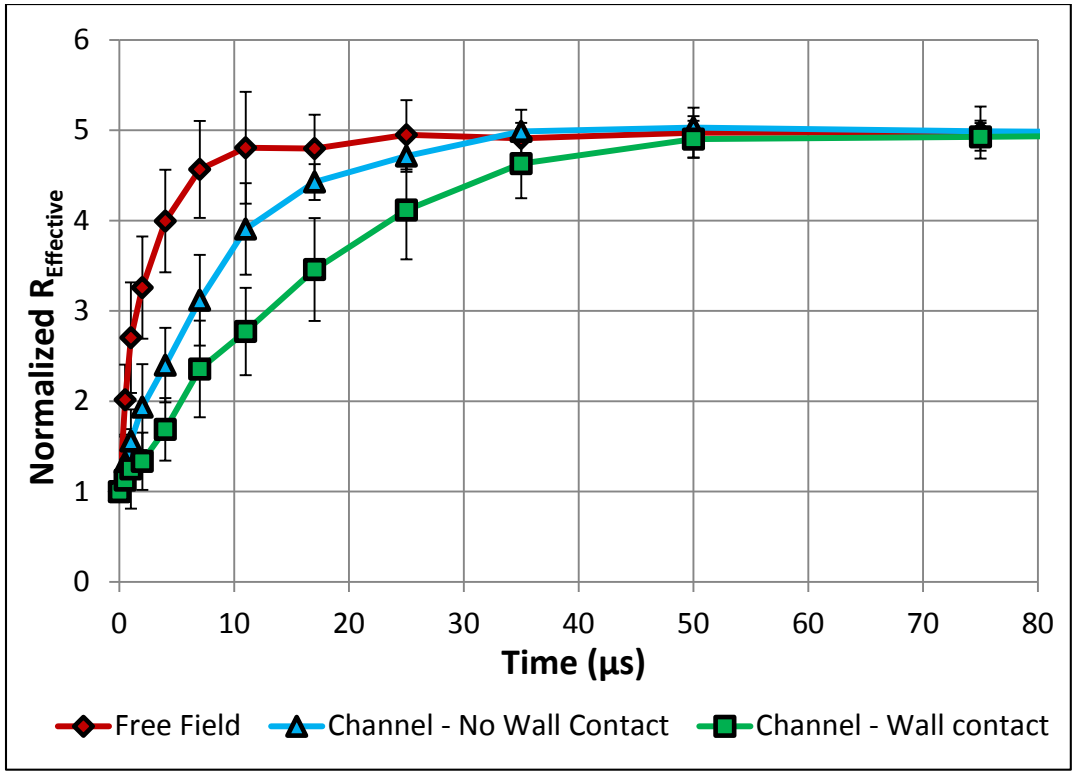

Figure 4. 6: Normalized effective bubble radius expansion of PFC microdroplets due to ADV in free-field conditions versus confined in a microchannel. Channel constrained droplet expiation were separated into bubbles that made wall contact versus those that did not. Viscous effects from the presence of the channel walls severely damped bubble expansion.

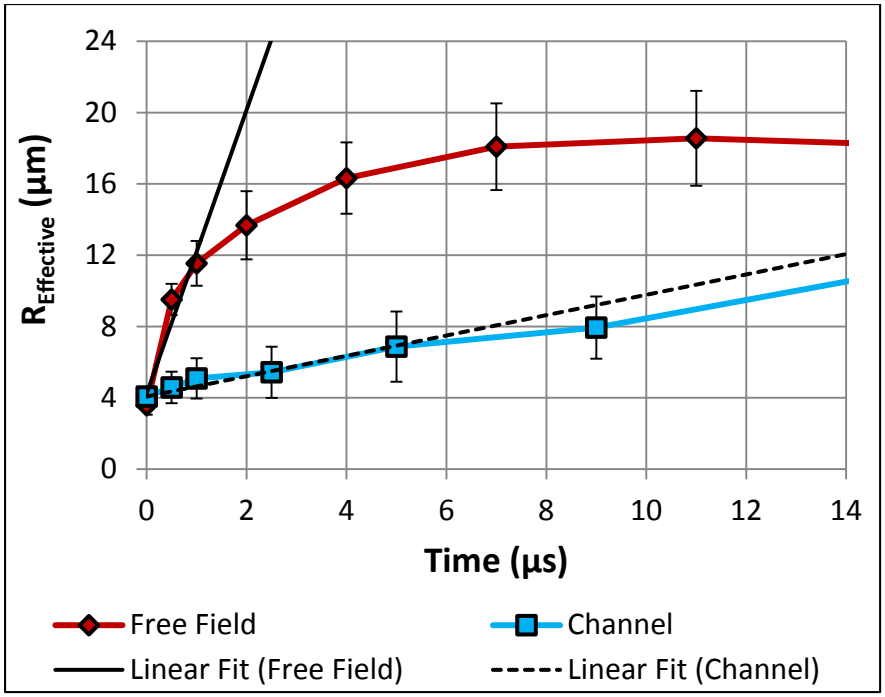

Figure 4. 7: Expansion ratios early in the vaporization process when the bubbles double in size. By using a linear fit to describe the data, the expansion velocities in free conditions over the first microsecond and confined conditions over the first 5.5 microseconds were estimated. Interface velocities of vaporized droplets with a mean diameter of 7.2 µm (STD=0.52 µm) expanded at an estimated peak interface velocity of 7.96 m/s in free field conditions. Droplets with a mean diameter of 8.0 µm (STD=0.58 µm) confined in 25 µm channels meanwhile expanded at a radial velocity of 0.57 m/s. R-squared values of the linear regressions over the free field expansion and channel constrained expansions were 0.79 and 0.81 respectively.

Chapter IV: References

[1] R. E. Apfel, "Activatable Infusible Dispersions Containing Droplets of a Superheated Liquid for Methods of Therapy and Diagnosis". United States of America Patent 5,840,276, 24 November 1998.

[2] J. L. Bull, "Cardiovascular Bubble Dynamics," *Critical Reviews in Biomedical Engineering,* p. 33(4): 299–346, 2005.

[3] O. D. Kripfgans, J. B. Fowlkes, D. L. Miller, O. P. Eldevik and P. L. Carson, "Acoustic Droplet Vaporization for Diagnostic Applications," *Ultrasound in Medicine and Biology,* p. 26(7): 1177–1189, 2000.

[4] O. D. Kripfgans, M. L. Fabiilli, P. L. Carson and J. B. Fowlkes, "On the acoustic vaporization of micrometer-sized droplets," *Journal of the Acoustical Society of America,* pp. 116(1): 272-281, 2004.

[5] A. H. Lo, O. D. Kripfgans, P. L. Carson, E. D. Rothman and J. B. Fowlkes, "Acoustic Droplet Vaporization Threshold: Effects of Pulse Duration and Contrast Agent," *IEEE Transactions on Ultrasonics, Ferroelectrics, and Frequency Control,* pp. 933-946, 2007.

[6] O. Shpak, T. Kokhuis, Y. Luan, D. Lohse, N. de Jong, B. Fowlkes, M. Fabiilli and M. Versluis, "Ultrafast Dynamics of the Acoustic Vaporization of Phase-Change Microdroplets," *Journal of the Acoustical Society of America,* Accepted for publication.

[7] Z. Z. Wong, O. D. Kripfgans, A. Qamar, J. B. Fowlkes and J. L. Bull, "Bubble Evolution in Acoustric Droplet Vaporization at Physiological Temperature Via Ultra-High Speed Imaging," *Soft Matter,* 2011.

[8] A. Qamar, Z. Z. Wong, J. B. Fowlkes and J. L. Bull, "Dynamics of Acoustic Droplet Vaporization in Gas Embolotherapy," *Applied Physics Letters,* pp. 143702-1-3, 2010.

[9] T. Ye and J. L. Bull, "Direct Numerical Simulations of Micro-Bubble Expansion in Gas Embolotherapy," *Journal of Biomechanical Engineering,* pp. 126: 745-759, 2004.

[10] T. Ye and J. L. Bull, "Microbubble Expansion in a Flexible Tube," *Journal of Biomechanical Engineering,* pp. 128: 554-563, 2006.

[11] S. Samuel, A. Duprey, M. L. Fabiilli, J. L. Bull and J. B. Fowlkes, "In Vivo Microscopy of Targeted Vessel Occlusion Employing Acoustic Droplet Vaporization," *Microcirculation,* vol. 19, pp. 501-509, 2012.

[12] A. J. Calderon, Y. S. Heo, D. Huh, N. Futai, S. Takayama, J. B. Fowlkes and J. L. Bull, "Microfluidic Model of Bubble Lodging in Microvessel Bifurcations," *Applied Physics Letters,* vol. 89, pp. 244103-1-3, 2006.

[13] MicroChem, "SU-8 2000 Permanent Epoxy Negative Photoresist Processing Guidelines For: SU-8 2000.5, SU-8 2002, SU-8 2005, SU-8 2007, SU-8 2010 and SU-8 2015," [Online]. Available: http://microchem.com/pdf/SU-82000DataSheet 2000_5thru2015Ver4.pdf. [Accessed 10 May 2013].

[14] MicroChem, "SU-8 2000 Permanent Epoxy Negative Photoresist Processing Guidelines for: SU-8 2025, SU-8 2035, SU-8 2050 and SU-8 2075," [Online]. Available: http://microchem.com/pdf/SU-82000DataSheet2025thru2075Ver4.pdf. [Accessed 10 May 2013].

[15] D. S. Li, O. D. Kripfgans, M. L. Fabiilli, J. B. Fowlkes and J. L. Bull, "Initial Nucletion Site Formation due to Acoustic Droplet Vaporization".

[16] D. L. Frost, "Initiation of explosive boiling of a droplet with a shock wave," *Experiments in Fluids,* pp. 8: 121-128, 1989.

[17] "NIST Chemistry WebBook," 2008. [Online]. [Accessed 9 December 2009].

[18] D. S. Li, O. D. Kripfgans, M. L. Fabiilli, J. B. Fowlkes and J. L. Bull, "Formation of Toroidal Bubbles from Acoustic Droplet Vaporization," *Applied Physics Letters,* p. Submitted, 2013.

CHAPTER V: A BOUNDARY ELEMENT MODEL OF A MICROBUBBLE SLIDING THROUGH A BIFURCATION

Introduction

Gas embolotherapy is a novel variation on more traditional embolotherapy methods, which rely on strategic catheter based delivery of solid or semi-solid embolizing agents to serve as a vessel occlusion for therapeutic purposes[1-4]. In gas embolotherapy, intravenously injected liquid encapsulated microdroplets are strategically vaporized using focused ultrasound to form larger localized gas bubbles that can serve as embolizing agents to limit nutrient supply to a vascularized tumor[3, 4]. The liquid microdroplets feature a perfluorocarbon (PFC) core and are normally encapsulated using an albumin or lipid membrane[5]. The process of using acoustic energy to selectively vaporize gas bubbles can be referred to as acoustic droplet vaporization (ADV). The use of these PFCs are ideal for gas embolotherapy not only because PFCs have been FDA approved for clinical use as contrast agents, but also because several chemical forms of PFCs have bulk boiling temperatures below body temperature (37˚C) allowing the resulting bubbles to remain stable in its gas phase and not recondensing after the initial vaporization[5]. The most common PFC chosen is dodecafluoropentane (DDFP, CAS No. 678–26–2) with a boiling point of 29˚C, but shorter carbon chain PFCs such as perfluorobutane (CAS No. 355-25-9) or perfluoropropane (CAS No. 76-19-7) with boiling points of -2˚C and -39˚C have also been

use[5-9]. Gas embolotherapy has been shown to be effective in reducing local blood perfusion in the vasculature during *in vivo* studies performed on canines[2, 10].

In contrast to gas embolotherapy, air embolism in the vasculature has long since been known to result in undesired consequences, which are potentially fatal if untreated[11-13]. In order to make the gas embolotherapy and other bubble based therapies more effective and safer in application, understanding the conditions that allow microbubbles to stick to vessel walls and lodge or dislodge in vessels will allow for more improved strategic approaches to reduce perfusion in a desired vessel of a given size and flow rate. In previous work relevant to bubble transport through vessels bench top model experiments using idealized vessel bifurcations followed by reduced order theoretical models were carried out to investigate the conditions required for bubble splitting and lodging[14, 15]. Recently, Samuel, *et al.* 2012 carried out *in vivo* studies using rat models investigating bubble lodging patterns after ADV exposure in microvasculature. The lodging patterns and conditions previously predicted and experimentally observed in microchannels from Calderon, *et al.* 2006[16] and the *in vivo* results from Samuel *et al.* 2012 [17] were in good agreement.

In the context of ADV and gas embolotherapy, the inability to extract details on bubble evolution, velocity fields, and wall stresses from the simplified models motivated the direct numerical simulations from Ye and Bull 2004 and 2006 investigating the velocities and stresses associated with the rapid bubble expansion from an ADV event in a rigid and flexible vessel environment[18, 19]. Following this work was development of boundary element models of finite sized bubbles attached to a vessel wall sliding through a vessel as well as a semi-infinite bubble approaching a bifurcation[20, 21]. From these numerical models, it was

concluded that endothelial damage could occur due to elevated wall shears due to the moving contact line.

Although previous numerical models have investigated the dynamics and stresses incurred at the bifurcation due to bubble motion or the influences of bubble adhesion forces on bubble motion in straight channels, no simulations to date have investigated geometric influences of the bifurcation combined with contact line adhesion on bubble lodging. This study focused on the transport of a small microbubble in contact with the wall initially near a bifurcating vessel exposed to a pressure gradient. This circumstance is possible in a variety of situations after ADV exposure or introduction of micro-/nanobubbles in microvessels. For example, if a vaporization event occurs near a vessel wall and the expanding bubble may come into contact and adhere to the vessel wall. Another possibility is a freely circulating bubble contacts and adheres to a vessel wall due to fluid momentum or acoustic radiation and the preexisting flow in the vessel pushes the bubble down the vascular tree. Additionally, differences in functionalized or uncoated bubbles and droplets will result in varying degrees of adhesion between the bubble interface and the vessel wall translating into to bubble sliding or sticking along the wall. The Boundary Element Method (BEM) was implemented to model bulk fluid surrounding the bubble under 2D Stokes flow conditions and the bubble was considered as an ideal gas and described using the ideal gas law. Tanner's law was used to describe the velocity the three-phase contact line between the bubble, vessel wall, and blood. Furthermore, two scenarios were considered: (1) proportional slip and (2) slip hysteresis where the bubble is allowed to stick.

Methods

The model presented considers the transient motion of a finite sized bubble approaching a geometrically symmetric two-dimensional bifurcating channel (Figure 5.1). The model consisted of two liquids (1) the bulk fluid surrounding the bubble, which is modeled as an incompressible Newtonian fluid, and (2) the gas bubble phase, which was assumed to act as ideal gas. For an incompressible Newtonian fluid mass and momentum must be conserved, and can be described using the following dimensionless equations:

$$\nabla \cdot \vec{u} = 0 \tag{1}$$

$$Ca \cdot Re\left\{\frac{\partial \vec{u}}{\partial \vec{t}} + \vec{u}(\nabla \vec{u})\right\} - \nabla p + Ca \cdot \nabla^2 \vec{u} \tag{2}$$

These equations the represent the (1) continuity and (2) Navier-Stokes equations. In the equations p and $\vec{u}$ represents the dimensionless pressure and velocity vector. Additionally, Ca and Re represent the dimensionless quantities known as the capillary number and the Reynolds number, given by $Ca = \frac{\mu^* U^*}{\sigma^*}$ and $Re = \frac{U^* L^* \rho^*}{\mu^*}$ where U^*, P^*, and L^* serve as our velocity, pressure, and length scales and μ^*, σ^*, and ρ^* represent our the viscosity, surface tension and viscosity of the bulk fluid. The velocity and pressure scales are given by $U^* = \frac{\sigma^*}{\mu^*}$ and $P^* = \frac{\sigma^*}{L^*}$.

Anatomic studies have shown that small venules and arterioles with radii on the order 50 μm have peak velocities on the ranging from 0.5 to 3 cm/s giving a Reynolds number of on the order of 0.06 to 0.38 [22]. Because of the small vessel diameters and low flow rates observed in the microcirculation, the Reynolds number was considered low

(Re<1) and the bulk fluid motion was reduced to Stokes flow. The updated dimensionless equations governing the bulk fluid are described by:

$$-\nabla p + \nabla^2 \vec{u} = 0 \tag{3}$$

Because of the Stokes flow condition and utilizing the fact that the partial differential equation is linear, symmetric, and homogenous in 2D, the differential equation describing the bulk fluid can be rewritten in the following boundary integral form[23, 24]:

$$c_{kj} u_k(\vec{x}_0) = \frac{-1}{4\pi \mathrm{Ca}} \int_C f_i(\vec{x}, \vec{x}_0) G_{ij}(\vec{x}, \vec{x}_0) dl(\vec{x}) + \int_C u_i(\vec{x}) T_{ijk}(\vec{x}, \vec{x}_0) n_k(\vec{x}) dl(\vec{x}) \tag{4}$$

The integrals are only required to be evaluated along the boundaries of the domain. f_i represents the Cartesian stress components, n is the unit normal pointing into the domain, c_{kj} represents a constant that is equal to $\frac{\delta_{kj}}{2}$ for smooth boundaries. Additionally, G_{ij} and T_{ijk} represent the Green's functions commonly referred to as the Stokeslet and the Stresslet, which are defined as:

$$G_{ij} = -\delta_{ij} \ln|\vec{x} - \vec{x}_0| + \frac{(x_i - x_{0i})(x_j - x_{0j})}{(\vec{x} - \vec{x}_0)^2} \tag{5}$$

$$T_{ijk} = -4 \frac{(x_i - x_{0i})(x_j - x_{0j})(x_k - x_{0k})}{(\vec{x} - \vec{x}_0)^4} \tag{6}$$

This formulation can be solved discretely using the numerical method known as the BEM[23, 24]. The boundary of the domain along with the bubble is discretized into quadratic elements to solve the integral in equation (4) numerically. An example of the discretized boundary domain is shown in figure 5.1. $\vec{x}_0$ is a point where the singularity exists and $\vec{x}$ is any point of interested away from the singular point. Gaussian quadrature was used to

evaluate the discrete boundary integrals along each boundary element. For elements where the singular functions G_{ij} or T_{ijk} existed outside the element on integration a traditional 10 point Gauss-Legendre quadrature method was used. However if the singular point was along the element of integration, a logarithmic form of the 10 point Gaussian quadrature was used instead[23]. By moving the singular point, $\vec{x}_0$, from node to node, a system of equations with mixed boundary conditions are generated that can be solved using Gauss elimination with partial pivoting to obtain the unknown velocities or stresses along the boundaries.

The simulations all began with a circular profiled bubble attached to the lower wall of the parent channel upstream of the bifurcation point. The bubble was offset such that the initial contact angles were at the equilibrium static contact angle of 70°. The starting position of the bubble was set to 1.5 times the channel diameter upstream of the carina of the bifurcation. The bifurcation was a symmetric splitting angle of 78° with a daughter to parent channel diameter ratio of 0.78. An initial pressure of 1, 2, 4, or 8 was specified inside the bubble. A constant pressure condition was set with the parent channel set to P=3 and the daughter channel P=1. The remaining walls had a zero velocity no slip boundary conditions imposed. At the two contact lines present, where the bubble attaches to the wall, contact line velocities are imposed using Tanner's law[20, 21, 25-27]. Tanner's law defines the leading contact line (the trailing edge only differs in sign) by:

$$u_{cl} = -k(\theta_D - \theta_S) \tag{7}$$

Where θ_D is the dynamic contact angle and θ_S is the static contact angle (the equilibrium contact angle for a stationary bubble). Tanner's law states that the speed the contact line is linearly proportional by a constant k to the deviation in the contact angle

when it is stationary. A sticking condition can be included through the addition of a contact hysteresis described by the following modified form of Tanner's law[20]:

$$u_{cl} = -k(\theta_D - \theta_A) \quad \text{for} \quad \theta_D < \theta_A \tag{8}$$

$$u_{cl} = -k(\theta_D - \theta_R) \quad \text{for} \quad \theta_D > \theta_R \tag{9}$$

$$u_{cl} = 0 \quad \text{for} \quad \theta_A < \theta_D < \theta_R \tag{10}$$

Where θ_A and θ_R represent the advancing and receding contact angles. In the numerical simulations presented, the parameters used were $k = 2$, $\theta_S = 70$, $\theta_A = 50°$, and $\theta_R = 70°$, which was shown to representative of conditions found in polydimethylsiloxane microchannels[16]. A discontinuity in boundary conditions is present where the contact line velocities are imposed. At these locations the contact line is expected to move according to Tanner's law, however adjacent to the contact line we have the no slip condition which contradicts such motion from occurring. In order to prevent singularities from occurring and maintaining stable solutions the contact line velocity was to decay linearly to no slip over a short distance away from two contact lines, which was held constant at 5% the length of the parent channel diameter[20, 21, 26, 27].

The internal pressure of the bubble was translated into a stress boundary condition through the jump boundary condition which in non-dimensional form is given by:

$$\Delta\vec{f} = \kappa \cdot \vec{n} \tag{11}$$

Where $\Delta\vec{f}$ is the difference in stress across the bubble interface, κ is the local curvature over the element, and $\vec{n}$ is the unit normal. The local curvature is computed through the cubic spline interpolant. Using the ideal gas law and integrating the volume of

the bubble, the bubble pressure at any given time can be calculated given the bubble pressure the stresses just within the bulk liquid domain using equation (11).

Although the Stokes flow equation (11) suggests that the fluid domain has no time dependency, quasi-steady motion can be enforced at the bubble interface [20, 21]. Once the flow field has been obtained from the boundary integral equation, the interface can be advanced in time through the following kinematic boundary condition along the bubble interface through a simple Euler integration:

$$\frac{\partial \vec{Y}}{\partial t} \cdot \vec{n} = \vec{u} \cdot \vec{n} \tag{12}$$

This suggests that the motion of a given point along the bubble interface,$\vec{Y}$, must move according to the local velocity, $\vec{u}$. Once the interface has been advanced in time the volume of the bubble can be recomputed and the bubble pressure is updated through the use of the ideal gas law. Next, the newly updated bubble pressure is translated to a stress condition through the jump boundary condition. Additionally, the contact angles must be recomputed and translated to contact line velocities through the use of Tanner's law. The flow field is then solved through the boundary integral equations, where once again the velocities at the bubble interface can be extracted to advance the nodes along the interface and the process is repeated in time. Over time there is a tendency for the nodes in front of the bubble to compress and elements behind the bubble to elongate. Furthermore, elements along the bubble interface also prone to compressing and stretching over time. For that reason, at each time step nodes along the bubble interface are redistributed to maintain equal spacing and elements along the channel interface are eliminated in front of the bubble and added behind the bubble as the bubble slides along the channel in an effort to maintain

equal node spacing over time. Time and grid convergence revealed that a time step of 0.05 and 600-800 quadratic grid elements provided ample solution accuracy (Figure 5.2). Convergence rates for time stepping and grid convergence were 1.39 and 2.33 respectively.

Results and Discussion

In all simulations the initial response for the bubble was to rapidly change size to maintain an equilibrium pressure with the surrounding pressure. Bubbles with initial pressure of 1 and 2 had initially exerted a pressure much lower than the local bulk fluid pressure, causing the bubble to initially decrease in size (Figure 5.3). Conversely, the bubbles with initial pressures of 4 and 8 had internal pressures higher than the local bulk fluid pressures, causing the bubbles to initially expand (Figure 5.3). Inversely proportional to the bubble volume was the bubble pressure over time (Figure 5.4). As expected, all the bubble pressures increased or decreased in an effort equilibrate with the local fluid pressure minus the difference in Laplace pressure. Because of the viscous pressure drop across the channel as the bubbles slowly moved downstream the bubbles would slowly expand regardless of initial bubble pressure. As a consequence of this, bubbles as they move across the microcirculation from the arteriole end to the venous end would experience a decreasing local pressure imposed on the bubbles. This would allow bubbles to increase in size as it moves downstream and thus assistance in bubbles lodging in the vasculature downstream from the initial vaporization site (Figure 5.4). However, once the bubble entered the daughter channel there was a slightly reduction in pressure and little change in bubble volume. Comparing the sticking condition to the slip scenarios, the rate of volumetric increase over time appeared to decrease due to a reduced bubble sliding velocity.

The left and right contacting points of the contact line are referred to as the trailing and leading contact lines. Because of the background flow imposed through the ambient pressure gradient of the bifurcation, the bubble naturally travels downstream resulting in an overall positive contact line velocity (Figures 5.5 and 5.6). However during the initial change in bubble volume to equilibrate bubble pressures, contact line velocities can be temporarily negative. For the low bubble pressures ($P_{initial}$=1 or 2) in the slip cases the leading contact line recedes as the bubble volume decreases (Figure 5.5). This is in contrast to the equivalent sticking cases whose leading edges are stuck with a zero velocity until the bubble has reached a near pressure equilibrium and deformed sufficiently to advance towards the bifurcation. The trailing edge of the high pressure bubbles, $P_{initial}$=8, for both slip and sticking cases and only the slip case of $P_{initial}$=4 have a trailing contact line that moves backwards towards the parent channel (Figure 5.6).

Once the bubbles make contact with turn leading into the lower daughter channel the bubble leading edge velocities immediate reduce (Figure 5.5). This is likely due to augmenting rolling angular velocity of the bubble. The moment of inertia for bubble as it travels in a linear fashion is near the center of the bubble. However, when the bubble is expected to rotated and enter the lower channel, the center of rotation is likely shifted closer to the plane of bubble wall contact. Another way of justifying the sudden decrease in contact line velocity is if the velocities along the outer periphery of the bubble are similar when traveling through a straight versus a curved section, the points closer to the wall and including the contact points must travel slower to maintain angular velocity. If not, the bubble would subsequently elongate and potentially detach. After the leading contact line passes over the curved section and enters the lower daughter channel, the leading contact

line immediately begins to accelerate. For sufficiently small bubbles ($P_{initial}$=1) under sticking conditions, the bubble is unable to advance past the turn and the bubble remains pinned at the turn of the bifurcation (Figure 5.10).

Effects on the trailing edge velocities due to a reduced leading edge velocity from the curved segment are not always apparently (Figure 5.6). The reduction in trailing edge velocity is most evident for small bubbles ($P_{initial}$=1) and is less apparent as bubble volume increases. Once the bubble leading edge cleared the curved section of the domain, trailing edge velocities increased to match leading edge velocities until the trailing edge contacted the curved portion of the lower wall. Once the trailing edge traverses over the curved section of the channel, a similar reduction in trailing edge velocity is seen as previously with the leading edge (Figure 5.5 and 5.6). After the bubble has completely cleared the turn and enters the daughter channel, the trailing edge velocities accelerates to match the leading edge velocity and the bubble slowly moves through the daughter channel at a constant velocity.

The relative change in forward motion of the bubble can be quantified through the overall torque acting on the bubble due to the stresses imparted on the bubble (Figure 5.7), where torque is defined as:

$$\vec{T} = -\vec{F}_{bubble} \times \vec{l}_{bubble} \tag{12}$$

Where $\vec{T}$ is the torque, $\vec{F}_{bubble}$ is the force acting along the bubble interface, and $\vec{l}_{bubble}$ is the lever arm. The negative sign in equation 12 was to define the sign convention of clockwise rotation of the bubble as positive and the counterclockwise rotation as negative. The lever arm vector used was defined as the vector length from the leading edge of the bubble to the node along the bubble interface. As expected for most of the bubbles the

torque acting on the bubble is positive, suggesting that the bubble is normally in forward motion. Looking at the torque during the sticking $P_{initial}$=1 scenario where the bubble is adhered to the bifurcation point in the channel (Figure 5.10), it can be seen that the torque remains non-zero even though the bubble contact line velocities are zero. It can be concluded that the torque acting on the bubble is unable to overcome the adhesion forces resulting from the sticking conditions originating from the contact line velocity hysteresis imposed through equations 8, 9, and 10. Furthermore, decreases in torque should be used as an indicator of likelihood of the bubble lodging. It can be seen that all bubbles appear to have a reduction in overall torque at the bifurcation point, suggesting increased probability of lodging. Once the bubble has completely cleared the bifurcation torque remains constant, suggesting that the bubble is moving forward at a constant velocity, which can be verified with the contact line velocities (Figures 5.5 and 5.6). Curiously, three cases investigated have torques that are negative in value, corresponding to $P_{initial}$=8 for both sticking and slip scenarios and for the sticking scenario of $P_{initial}$=4. Looking at the bubble evolution (Figures 5.14, 5.15, and 5.16) these bubble all elongate and come into close contact with the carina of the bifurcation. As a result of this, two forces may be causing this reversal in sign of torque. First, the physical interaction between the bubble and the carina of the bifurcation provides a physical obstruction to the forward momentum of the bubble. If the surface of the bubble has a tendency to roll in a tank treading motion downstream, this would provide a clockwise motion. This is in contrast to the scenario where the periphery of the bubble is pinned to the carina of the bubble but the contact line continues to move downstream. This interaction would result in an overall reversal in torque and a counterclockwise motion of the bubble even though the bubble continues to move downstream in bifurcation. The

second factor limiting the forward momentum of the bubble and contributing to the negative torques observed is due to the different in the Laplace pressure in the parent and daughter channel facing halves of the bubble. Because of the reduction in channel diameters of the daughter channels relative to the parent channel, the bubble must deform to fit into the bifurcation. As a consequence of this, curvature of the section of bubble in the daughter channel is greater than that in the parent channel, thus the Laplace pressure jump is higher on the daughter channel facing portion of the bubble than the parent channel facing half. In the model, the possibly development of addition contact points for the bubble was neglected, allowing these bubbles to continue deforming and eventually entering the daughter channel. However, physically it is most likely that the bubble would contact the wall at the carina and adhesion forces from wall contact would be greater for the larger bubbles (i.e. $P_{initial}$=4 and 8) than observed, promoting bubble lodging.

Looking at flow rates entering and exiting the domain through the parent and two daughter channels, positive flow rates were defined as mass exiting the domain while negative values suggested mass entering the domain. As expected, once the bubble volume and pressure equilibrate flow entering the channel through the parent channel was balanced with the flow exiting the domain through the two daughter channels (Figure 5.8). In the earlier time scales, the expansion from the high pressure bubbles ($P_{initial}$=4 and 8) resulted in overall fluid mass being pushed out of the domain, while the shrinking of the low pressure bubbles ($P_{initial}$=1 and 2) caused initial flow to enter the domain from all channels. Curiously, there was a slight decrease in flow exiting the upper daughter channel at approximately T=100 for the high pressure bubbles ($P_{initial}$=4 and 8) that is not observed in the lower channel. This is likely a result of the combined elongated profile of the bubble in the

bifurcation area and the bubble contact lines moving downward and entering the lower daughter. The combination of these two effects may result in overall tension on the fluid that would enter the upper daughter channel and drag more fluid along with the bubble into the lower channel.

Wall stresses along the lower wall, upper wall, and the bifurcation wall was monitored as a function of bubble location. Figures 5.9 through 5.16 plot the initial bubble geometry along with five additional time points during the transport process. The wall shear stresses plotted were superimposed over the corresponding geometry of the domain and bubble and plotted as a function of spatial X-position for the top and bottom walls or Y-position for the bifurcation wall. Overall, stress profiles between equivalent initial bubble pressures for sticking versus slip scenarios had little difference in magnitude or location. The largest difference observed between the slip and sticking cases was bubble position over time, which was determined by the slip velocities from Tanner's law. For all cases, with exception for $P_{initial}$=4, the greatest shear stresses observed were during the initial expansion or compression of the bubble. The increase in shear stress can be seen in along all boundaries, with the parent channel walls typically experiences the highest shear stresses. The parent channel likely experiences the highest shear due to having a lower cross-sectional area than the combined daughter channels. Therefore the relative flow that is displaced from the respective daughter channels is likely lower than that in the parent channel, thus the higher stresses seen. The $P_{initial}$=4 condition (Figures 5.13 and 5.14) initially experiences the lower shear stress in the parent channel because the flow that would typically enter the parent channel is negated by the expansion of the bubble. This can be confirmed by the low initial mass transfer from the parent channel shown in figure 5.8. The wall stress far from

the bubble is also relatively constant as expected from fully developed Poiseuille flow. During the bubble transport process, there were four locations that appeared to have locally high wall shears: contact lines, the carina, the turn prior to entering the upper daughter channel, and wall sections opposing the upper boundary of the bubble where a fluid film can exist. Elevated stresses along the upper boundary as well at the contact lines has been previously documented in contact line bubble transport problems. At the carina, a stagnation point exists which may explain the sign change in observed sign changes at Y=0. The carina and the turn along the upper wall likely experience these locally high stresses due to geometric divergences in the flow. Additionally, the fluid at the carina as the bubble approaches the bifurcation may develop a thin film as the bubble comes into near contact with the boundary (Figures 5.13 through 5.16). As the fluid is squeezed out of the film a high velocity gradient is developed between the non-moving wall and the bubble interface. In a similar manner the fluid film separating large bubbles from the boundary appear to develop a high shear near the front of the bubble along the upper wall (Figure 5.15 and 5.16). This is likely due to increased velocities from the acceleration of the fluid from the nose of the bubble to the body of the bubble as the cross section area for the fluid to pass through narrows. These locations are sites where the endothelium may receive damage. Damage to the endothelium at the bifurcation may not necessarily be a bad bioeffect in the context of ultrasound therapies, such as gas embolotherapy. If the damage is limited to near the insonation area where occlusion is wanted, clotting cascades may enhance bubble occlusion, thereby enhancing therapeutic efficacy for gas embolotherapy. Additionally, damage from the bubble motion could also result in a compromised endothelial lining promoting enhancing vessel permeability and improving drug delivery across the vessel wall.

Conclusions

The results presented were derived from a boundary element model of a bubble sliding along a wall due to a pressure gradient in a 2D bifurcating channel under Stokes flow conditions. The quasi-steady model developed is a reasonable model of idealized conditions found in small microvessels where the small bubble may originate from bubble based ultrasound therapy, such as gas embolotherapy, or from other sources that may result in gas emboli. Two forms of Tanner's law was employed to compare a bubbly slipping condition to sticking conditions, modeling through a contact like hysteresis condition. Results show that due to the adhesion forces, bubble sliding velocities were lower but wall shear stresses observed were similar for equal pressure bubbles. Sticking scenarios were concluded to promote bubble lodging of small bubbles at bifurcation points as well promoting bubble interaction with the bubble and the carina for larger bubbles. Because the bubbles were not allowed to make additional contact points with the wall, the largest bubbles ($P_{initial}$=8) simulations were ended before completely entering the daughter channel due to colliding boundary points of the bubble to carina. Conceivably, theses bubbles along with the $P_{initial}$=4 bubbles may actual rupture the thin film separating the bubble and the carina promoting greater adhesion forces enhancing bubble lodging. The results presented in this model appear suggest that because of the geometry of the bifurcation, bubble lodging is enhanced at bifurcation points, which falls in line with experimental observations carried out in bench top microchannel experiments as well as in *in vivo* experiments[16, 17].

Chapter V: Figures

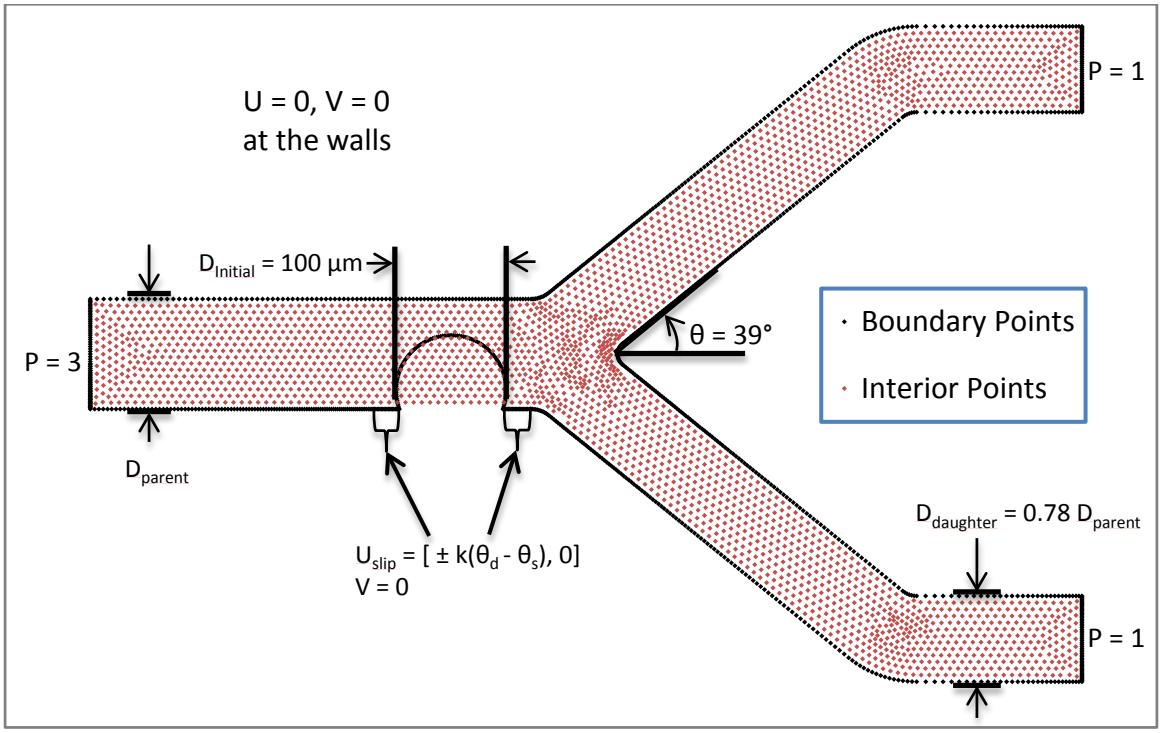

Figure 5. 1: Above is a representative image of both the boundary elements nodes as well as the interior nodes. In order to evolve the bubble over time, only information regarding stress and velocity are needed along the interface walls. Solving for fluid velocities and stresses in the interior of the fluid domain is only necessary for plotting purposing. The bubble was initialized as a circular bubble with contact angles at the static contact angle. A small pressure gradient was imposed forcing the bubble to travel through the vessel. Because of the discontinuity in boundary conditions at the vessel wall and along the bubble interface, a short slip region was imposed before and after the bubble. In the slip velocity of the bubble was allowed to linearly decay to zero over the slip region.

A

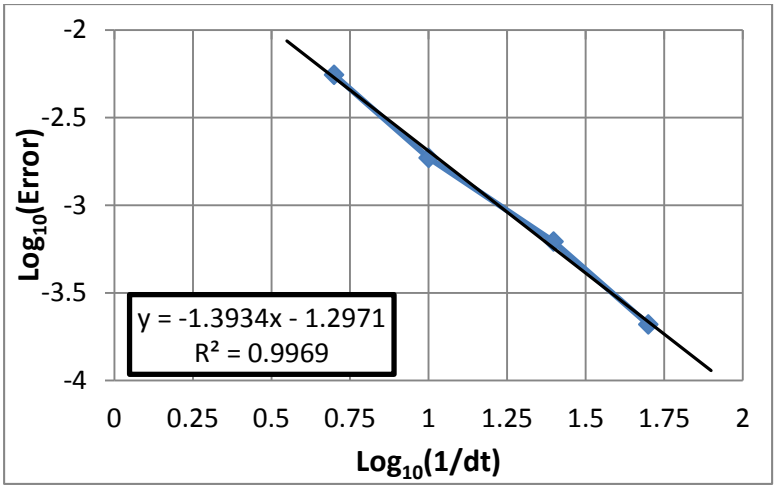

B

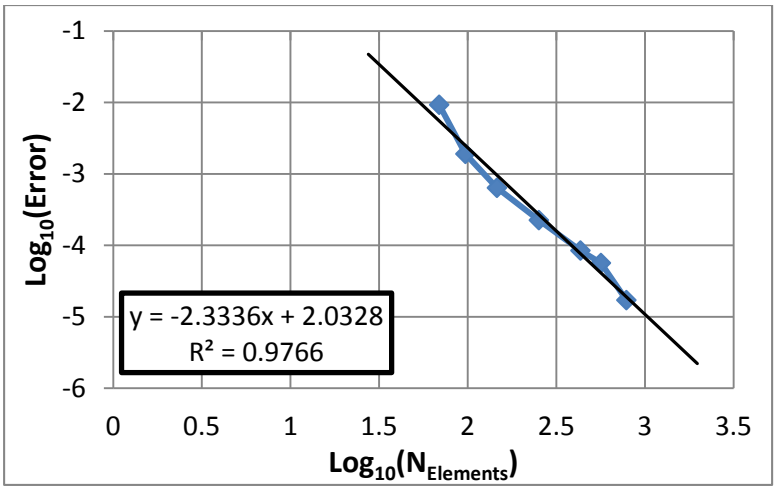

Figure 5. 2: Time and convergence analysis reveals convergence rates of 1.39 and 2.33 respectively. Time step sizes of $\Delta t = 0.05$ and approximately 600 to 800 quadratic boundary elements were considered to provide sufficient solution accuracy.

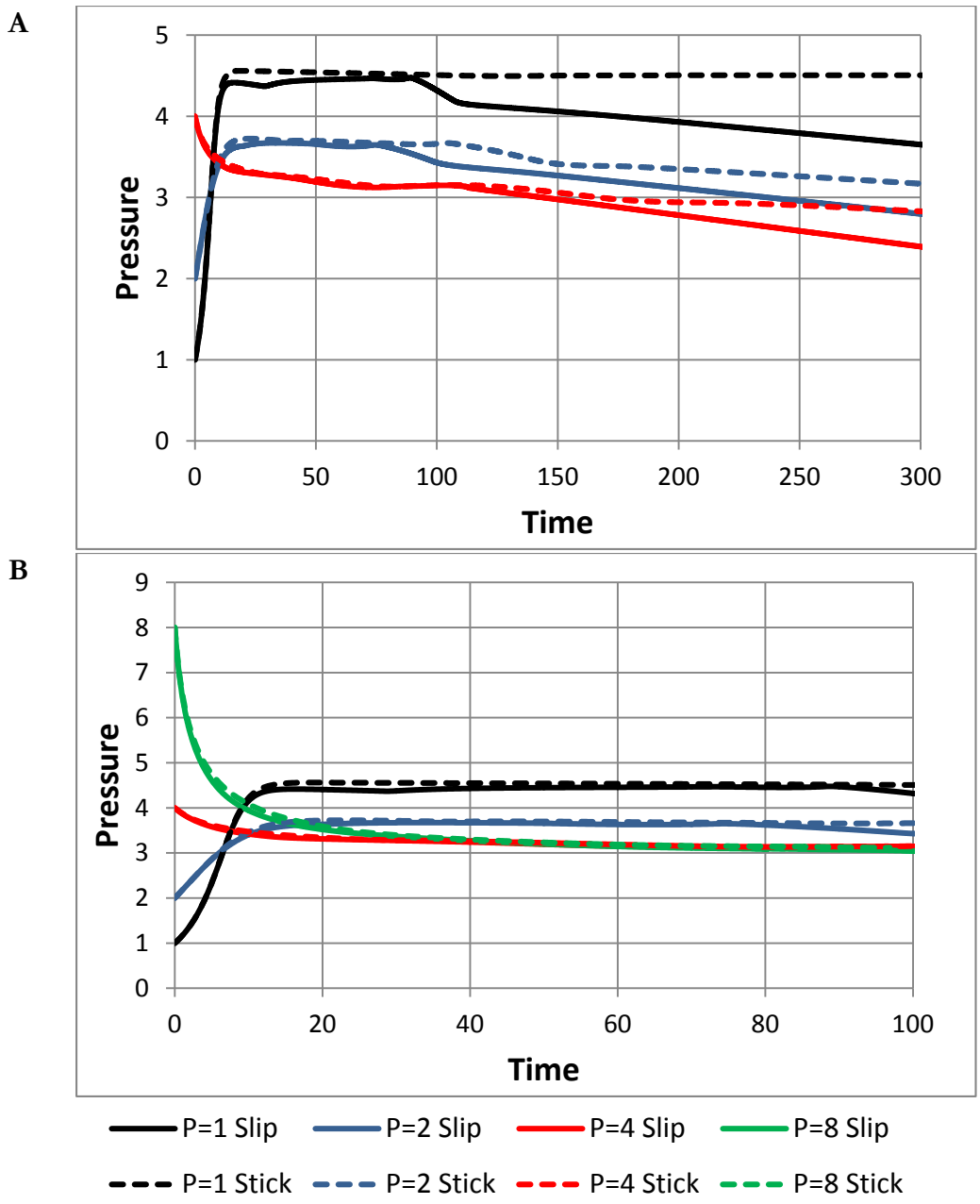

Figure 5. 3: Pressure over time as the bubble travels through the bifurcation. (A) Presents the longer time scale results excluding the initial pressure of P=8, while (B) presents the shorter time scale results. The bubbles initially increase ($P_{initial}$= 1 or 2) or decrease ($P_{initial}$= 4 or 8) to reach an equilibrium with the local fluid pressure. As the bubble travels through the channel bubble pressure decreases due to the decreasing local pressure from viscous pressure losses. Rate of pressure change is lower for the sticking cases due to a slower bubble sliding velocity

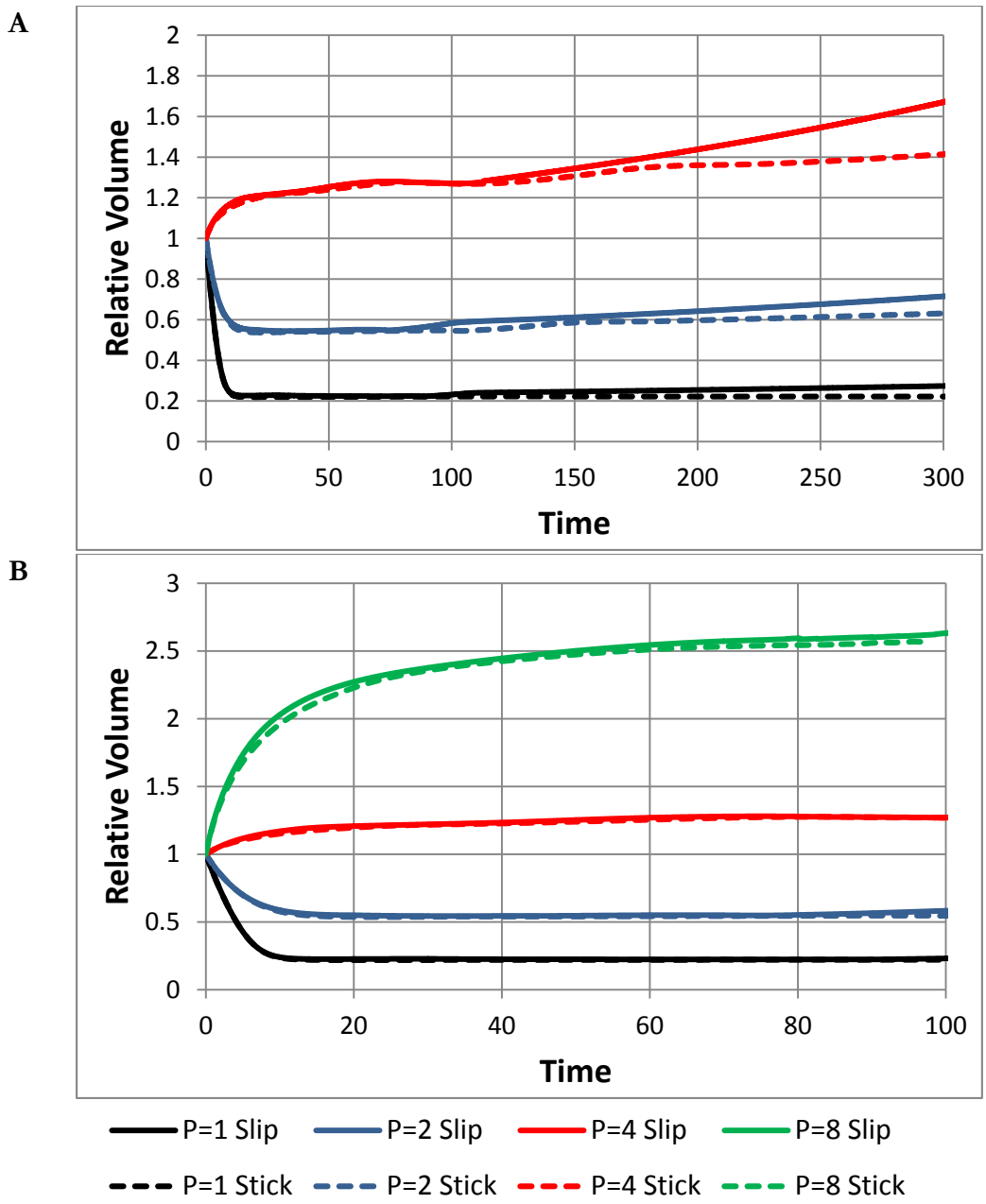

Figure 5. 4: Relative volume of the bubble over time as the bubble travels through the bifurcation. (A) Presents the longer time scale results excluding the initial pressure of P=8, while (B) presents the shorter time scale results. There is an initial rapid change in pressure resulting in a change in volume of the bubble. Naturally, low initial pressure bubbles ($P_{initial}$=1 or 2) decrease in size while large bubble increase in size ($P_{initial}$=4 or 8)

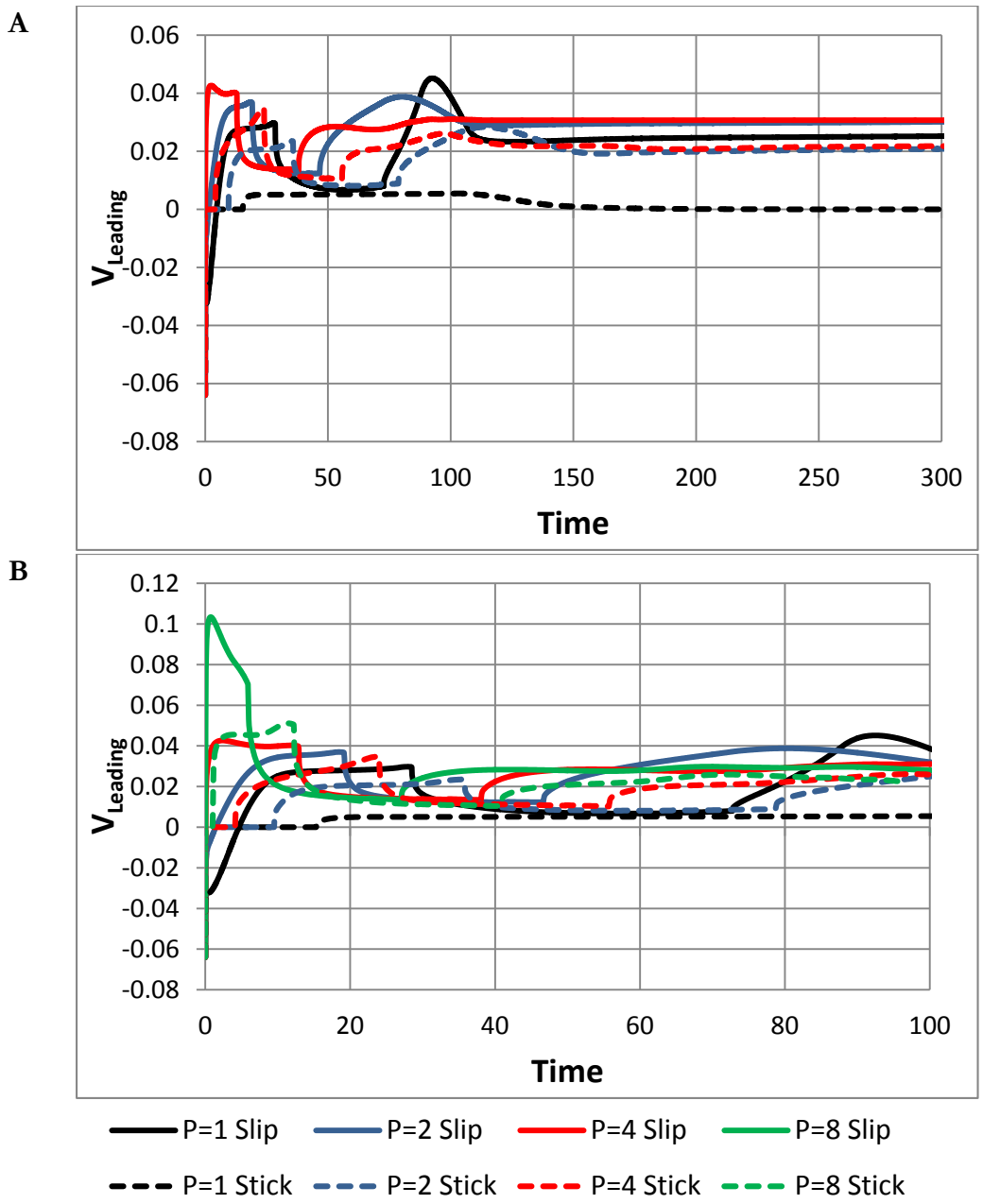

Figure 5. 5: Leading edge velocity of the bubble over time. (A) Presents the longer time scale results excluding the initial pressure of P=8, while (B) shows the shorter time scale results. Leading edge velocities for the low bubble pressure are initially negative due to the decrease in bubble size. The initial exponential decay in leading edge velocities correspond to when the leading edge of the bubble contacts the turn before entering the daughter channel. Once the leading edge passes the turn the leading edge accelerates. Overall, leading edge velocities for sticking bubble cases are lower than the slip condition counterparts.

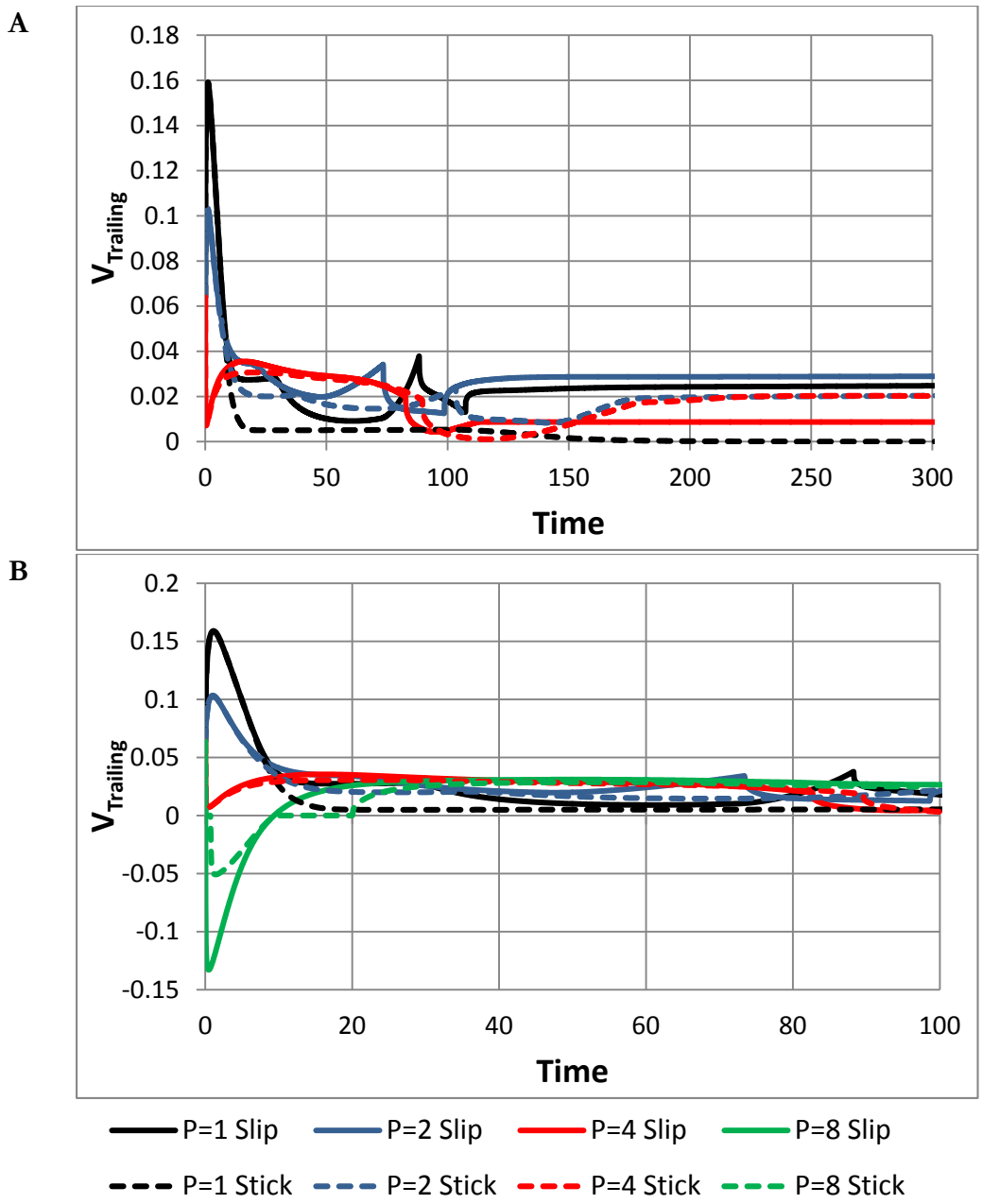

Figure 5. 6: Trailing edge velocity of the bubble over time. (A) Presents the longer time scale results excluding the initial pressure of P=8, while (B) shows the shorter time scale results. Trailing edge velocities for the highest bubbles pressure are initially negative due to the increase in bubble size. As the trailing edge of the bubble passes over the turn, the trailing edge velocities decrease until it completes the turn. For small bubbles ($P_{initial}$=1 or 2) there is a noticeable increase in trailing edge velocity corresponding to the acceleration of the leading edge once it passes the turn prior to entering the lower daughter channel. Overall, trailing edge velocities for sticking bubble cases are lower than the slip condition counterparts.

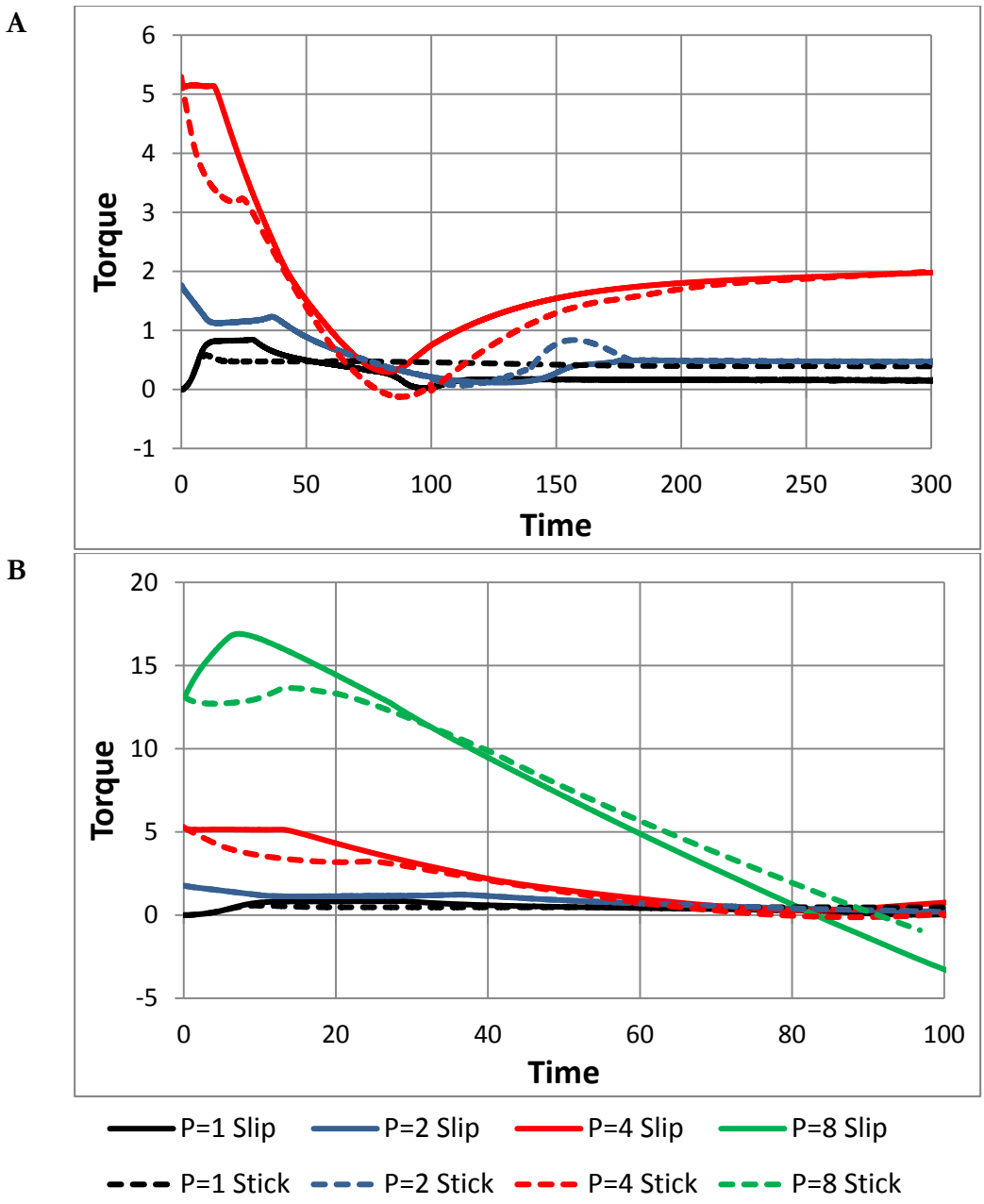

Figure 5. 7: Torque acting on the bubble over time. (A) Presents the longer time scale results excluding the initial pressure of P=8, while (B) shows the shorter time scale results. Bubble torque is positive due to the forward rolling motion of the bubble. If the bubble is sufficiently large, the torque on the bubble near the bifurcation point can be negative. The negative torque is due to the bubble possibly reversing in direction or momentarily lifting off of the channel wall.

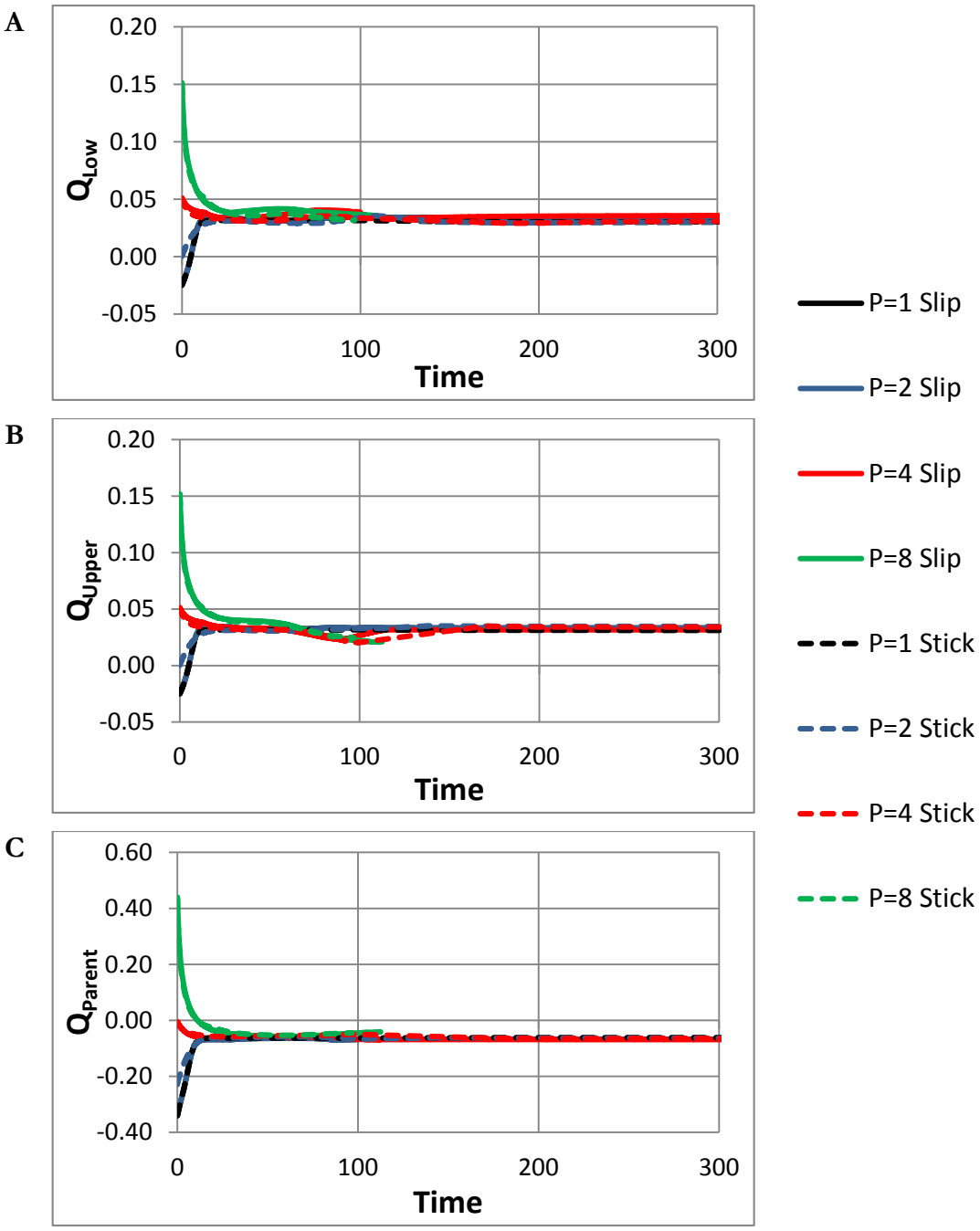

Figure 5. 8: Flow in the three respective channels: (A) the lower daughter channel, (B) the upper daughter channel, and (C) the parent channel. Positive flow rates for represents flow exiting the domain while negative values represent flow entering the domain. For sufficiently large bubbles ($P_{initial}$= 4 or 8) there is a temporary decrease in flow in the upper daughter channel that is not observed in the lower channel. This temporary decrease in flow corresponds to the bubble expanding or lifting from the attached wall and obscuring flow to the upper channel. However, due to the moving contact line the bubble is dragged into the lower channel resulting in little change to the flow rate in the lower channel.

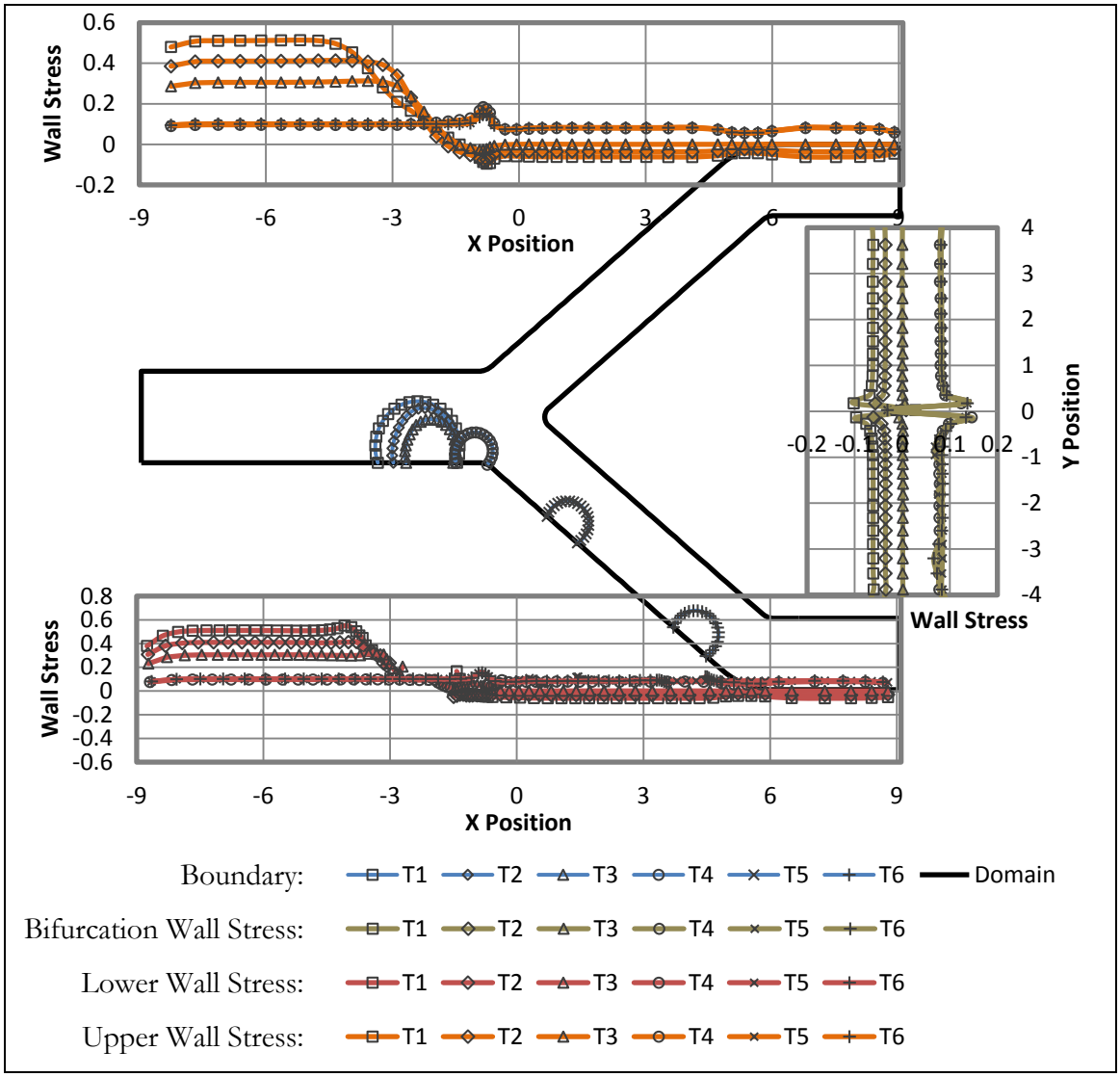

Figure 5. 9: Corresponding bubble positions and wall shears at times T1=0, T2=2.5, T3=5, T4=50, T5=200, and T6=400 for the $P_{initial}$=1 slip scenario. Wall shears are highest as the bubble contracts. Locally high shears are also observed near the carina of the bifurcation as well as the turn on the upper wall as the bubble passes the two locations. 1 dimensionless unit of stress equates to 1.4 kPa.

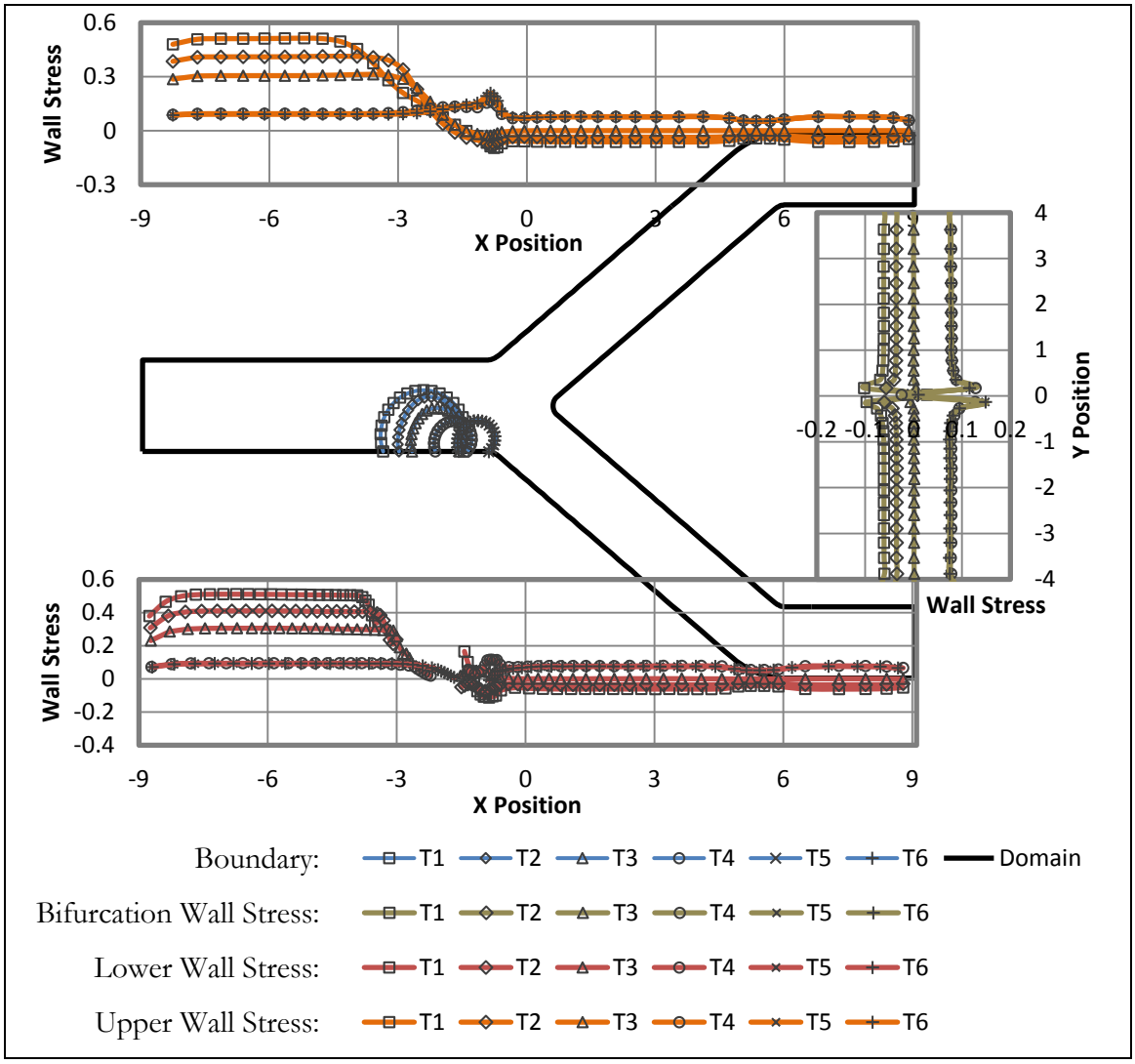

Figure 5. 10: Corresponding bubble positions and wall shears at times T1=0, T2=2.5, T3=5, T4=50, T5=200, and T6=400 for the $P_{initial}$=1 sticking scenario. Wall shears are highest as the bubble contracts. Because of the sticking, the bubble does not advance past the bifurcation. 1 dimensionless unit of stress equates to 1.4 kPa.

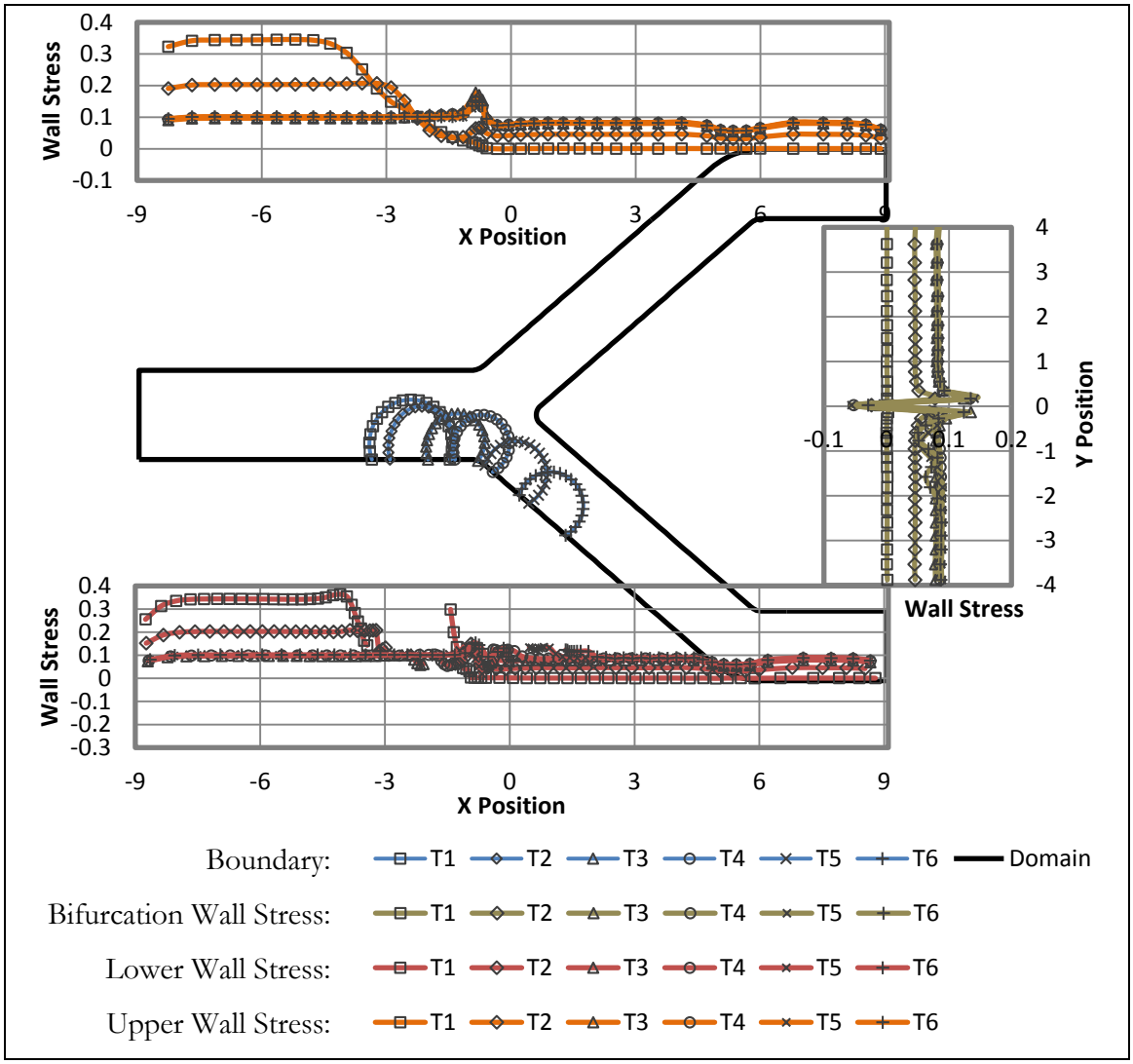

Figure 5. 11: Corresponding bubble positions and wall shears at times T1=0, T2=5, T3=30, T4=60, T5=100, and T6=150 for the $P_{initial}$=2 slip scenario. Wall shears are highest as the bubble contracts. Locally high shears are also observed near the carina of the bifurcation as well as the turn on the upper wall as the bubble passes the two locations. 1 dimensionless unit of stress equates to 1.4 kPa.

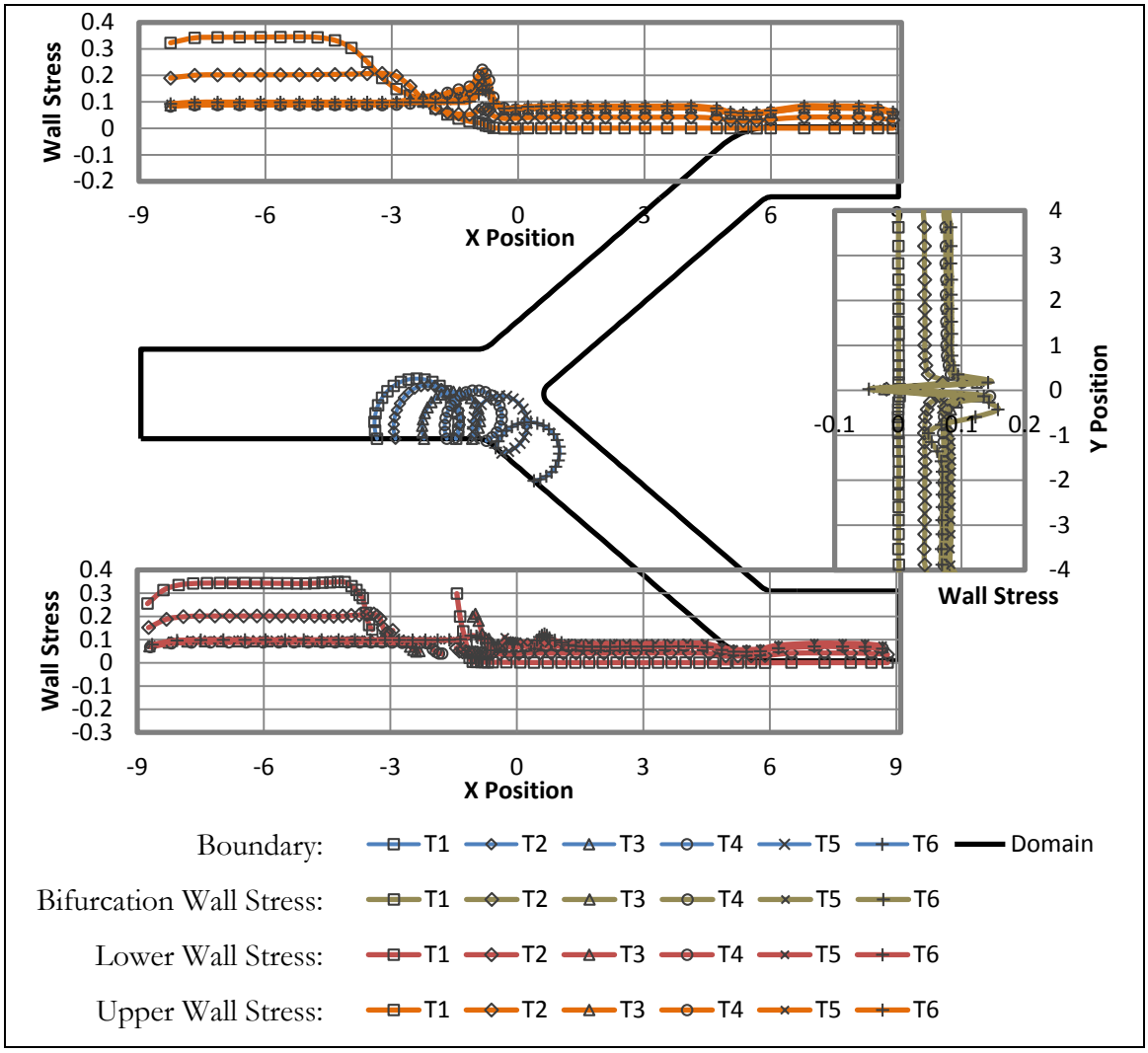

Figure 5. 12: Corresponding bubble positions and wall shears at times T1=0, T2=5, T3=30, T4=60, T5=100, and T6=150 for the $P_{initial}$=2 sticking scenario. Wall shears are highest as the bubble contracts. Locally high shears are also observed near the carina of the bifurcation as well as the turn on the upper wall as the bubble passes the two locations. 1 dimensionless unit of stress equates to 1.4 kPa.

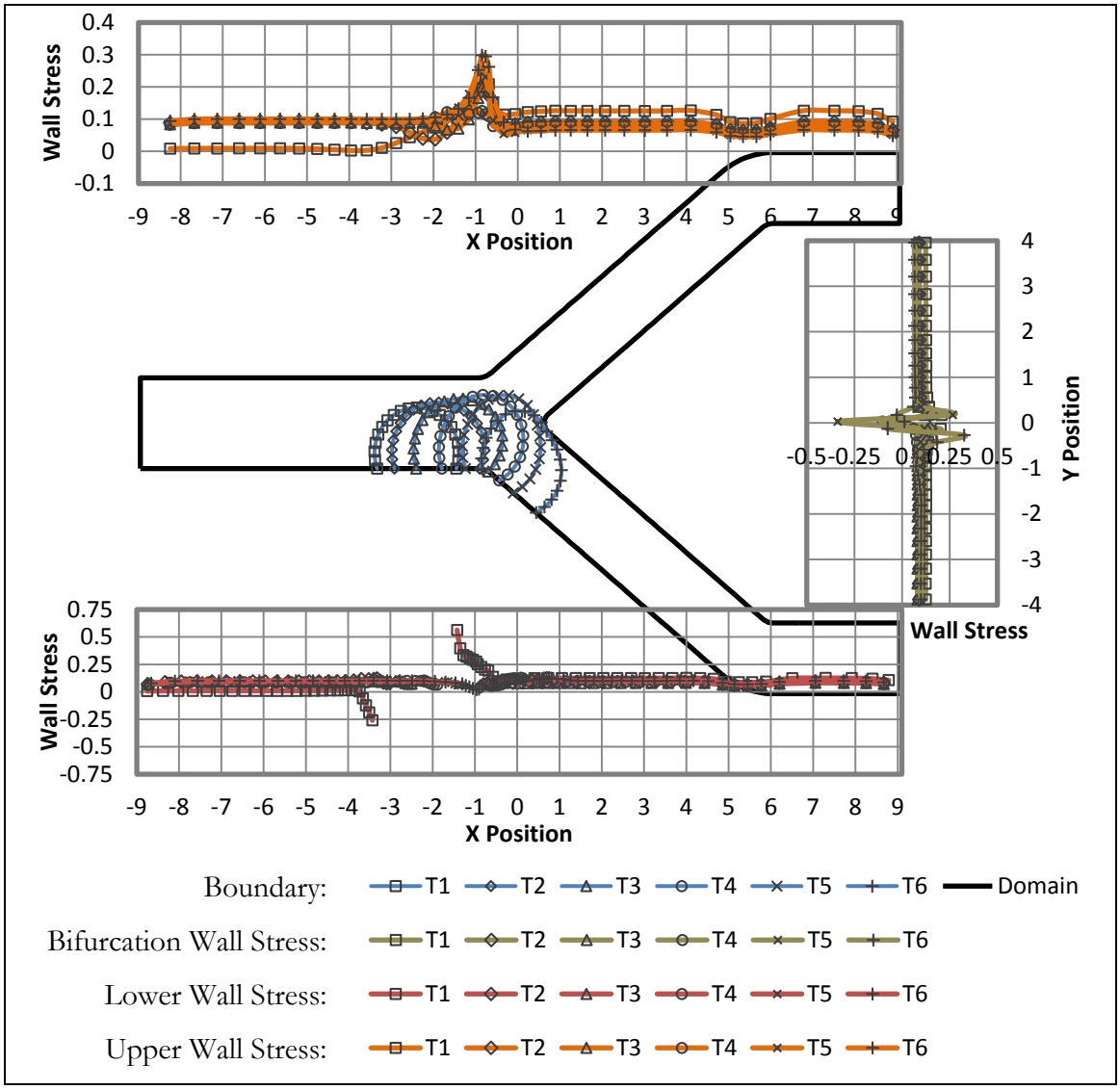

Figure 5. 13: Corresponding bubble positions and wall shears at times T1=0, T2=15, T3=30, T4=50, T5=70, and T6=100 for the $P_{initial}$=4 slip scenario. The highest local wall shears also observed near the carina of the bifurcation as well as the turn on the upper wall as the bubble passes the two locations. Because the bubble is expanding, it counters the pressure from the parent channel and limits the flow entering the domain. This results in the near zero shear observed along the parent channel walls, with exception of the region near the bubble. 1 dimensionless unit of stress equates to 1.4 kPa.

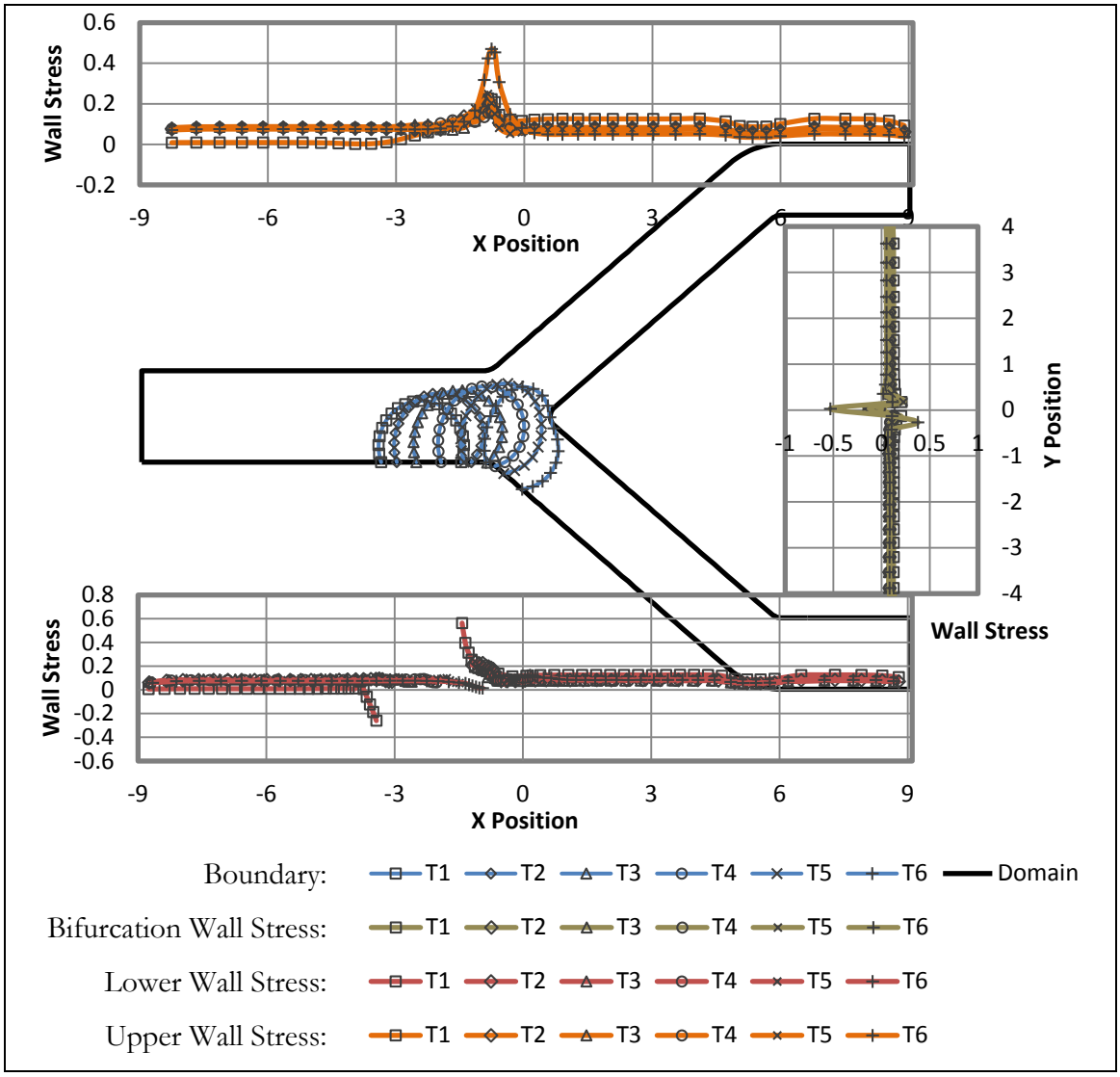

Figure 5. 14: Corresponding bubble positions and wall shears at times T1=0, T2=15, T3=30, T4=50, T5=70, and T6=100 for the $P_{initial}$=4 sticking scenario. The highest local wall shears also observed near the carina of the bifurcation as well as the turn on the upper wall as the bubble passes the two locations. Because the bubble is expanding, it counters the pressure from the parent channel and limits the flow entering the domain. This results in the near zero shear observed along the parent channel walls, with exception of the region near the bubble. 1 dimensionless unit of stress equates to 1.4 kPa.

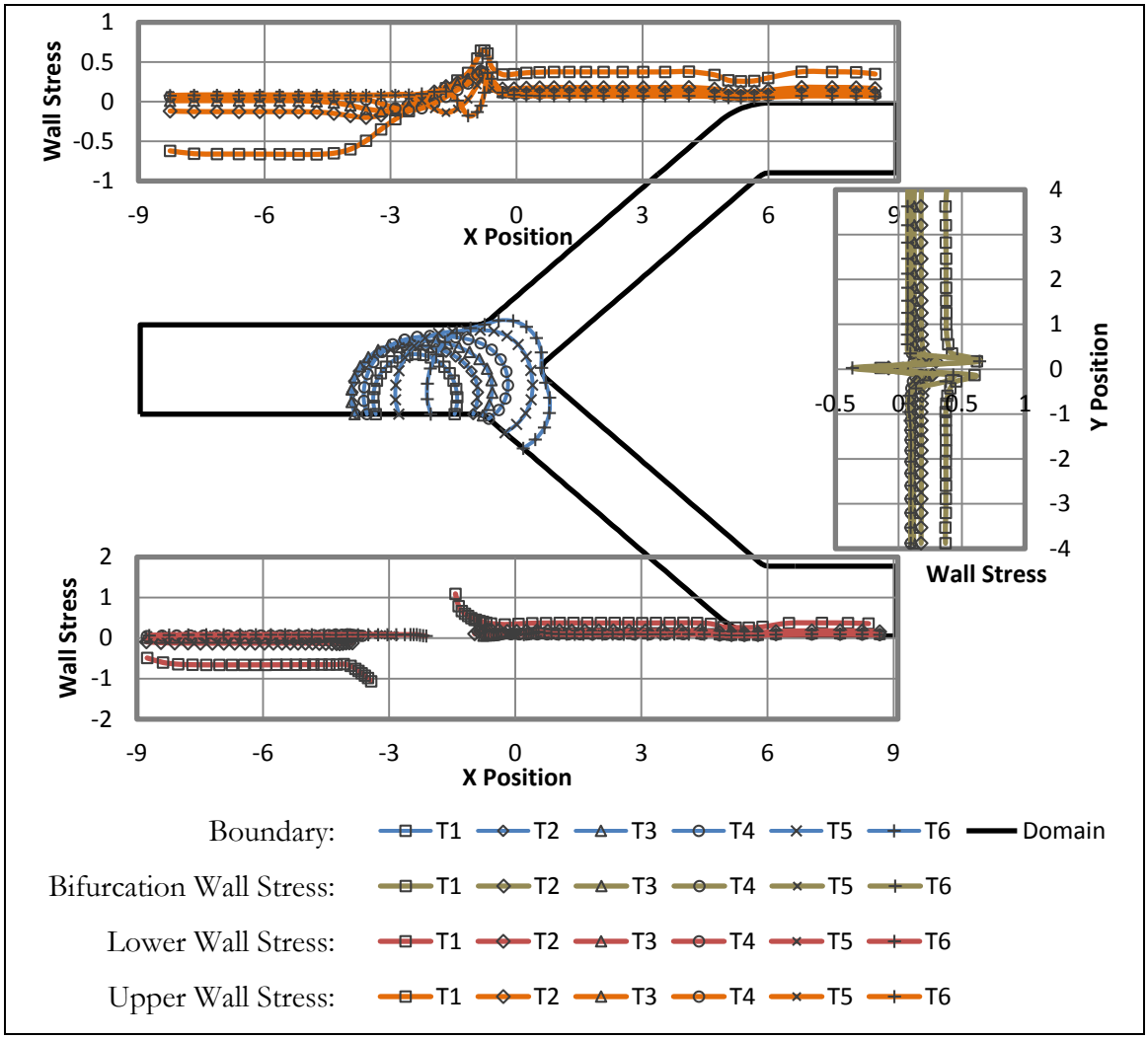

Figure 5. 15: Corresponding bubble positions and wall shears at times T1=0, T2=5, T3=12.5, T4=25, T5=50, and T6=75 for the $P_{initial}$=8 slip scenario. Wall shears are highest as the bubble expands, forcing fluid out of the parent and daughter channels. Locally high shears are also observed near the carina of the bifurcation as well as the turn on the upper wall as the bubble passes the two locations. 1 dimensionless unit of stress equates to 1.4 kPa.

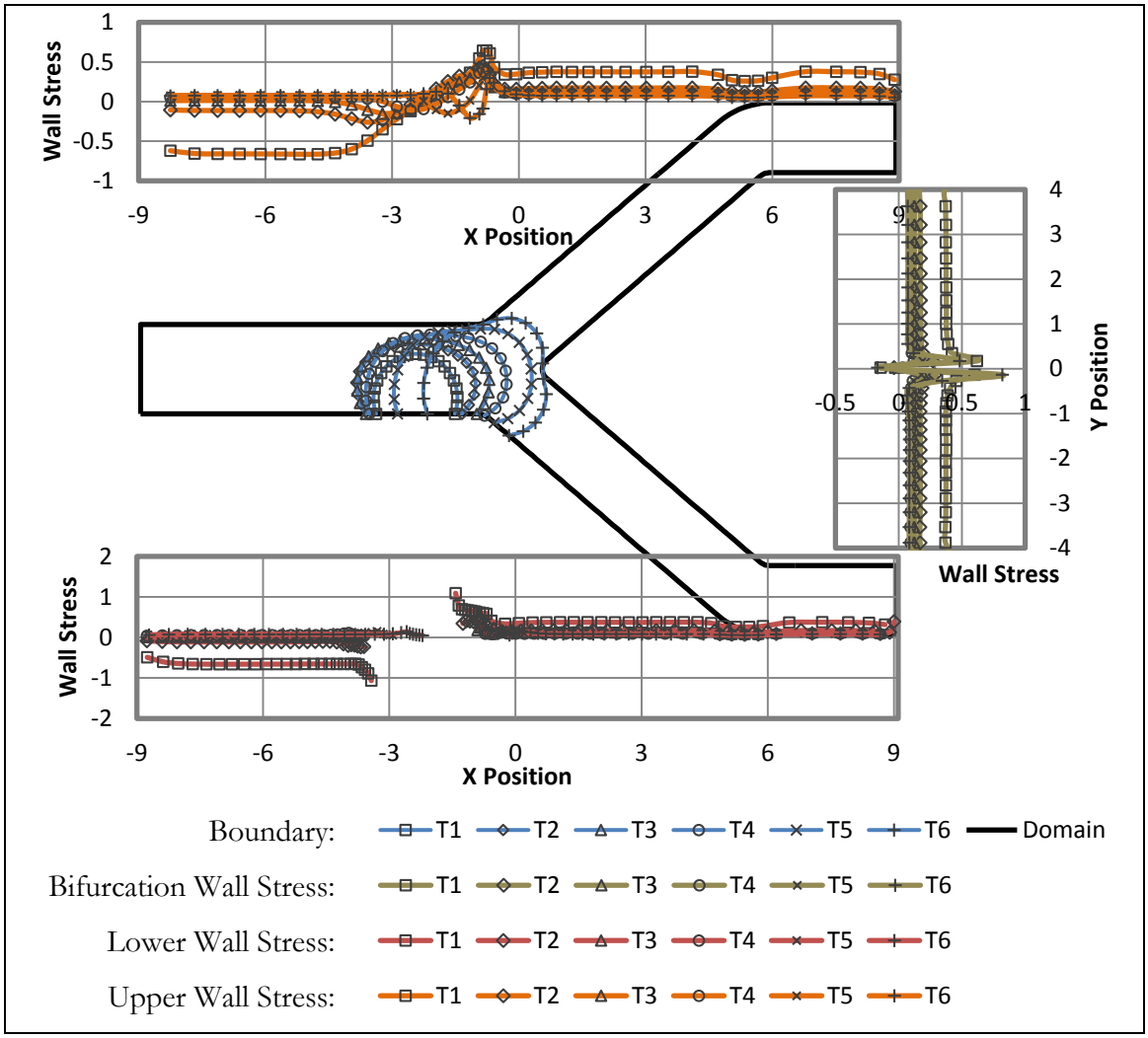

Figure 5. 16: Corresponding bubble positions and wall shears at times T1=0, T2=5, T3=12.5, T4=25, T5=50, and T6=75 for the $P_{initial}$=8 sticking scenario. Wall shears are highest as the bubble expands, forcing fluid out of the parent and daughter channels. Locally high shears are also observed near the carina of the bifurcation as well as the turn on the upper wall as the bubble passes the two locations. 1 dimensionless unit of stress equates to 1.4 kPa.

Chapter V: References

[1] R. E. Apfel, "Activatable Infusible Dispersions Containing Droplets of a Superheated Liquid for Methods of Therapy and Diagnosis". United States of America Patent 5,840,276, 24 November 1998.

[2] O. D. Kripfgans, C. M. Orifici, P. L. Carson, K. A. Ives, O. P. Eldevik and B. J. Fowlkes, "Acoustic Droplet Vaporization for Temporal and Spatial Control of Tissue Occlusion: A Kidney Study," *IEEE,* pp. 52(7): 1101-1110, 2005.

[3] O. D. Kripfgans, J. B. Fowlkes, D. L. Miller, O. P. Eldevik and P. L. Carson, "Acoustic Droplet Vaporization for Diagnostic Applications," *Ultrasound in Medicine and Biology,* p. 26(7): 1177–1189, 2000.

[4] J. L. Bull, "Cardiovascular Bubble Dynamics," *Critical Reviews in Biomedical Engineering,* p. 33(4): 299–346, 2005.

[5] O. D. Kripfgans, M. L. Fabiilli, P. L. Carson and J. B. Fowlkes, "On the acoustic vaporization of micrometer-sized droplets," *Journal of the Acoustical Society of America,* pp. 116(1): 272-281, 2004.

[6] M. L. Fabiilli, K. J. Haworth, I. E. Sebastian, O. D. Kripfgans, P. L. Carson and J. B. Fowlkes, "Delivery of Chlorambucil Using Acoustically-Triggered Perfluoropentane Emulsion," *Ultrasound in Medicine & Biology,* vol. 36, no. 8, pp. 1364-1375, 2010.

[7] M. L. Fabiilli, J. A. Lee, O. D. Kripfgans, P. L. Carson and J. B. Fowlkes, "Delivery of Water-Soluble Drugs Using Acoustically Triggered Perfluorocarbon Double Emulsions," *Pharmaceutical Research,* p. 2753–2765, 2010.

[8] P. S. Sheeran and P. A. Dayton, "Phase-Change Contrast Agents for Imaging and Therapy," *Current Pharmaceutical Design,* pp. 2152-2165, 2012.

[9] T. D. Martz, P. S. Sheeran, D. Bardin, A. P. Lee and P. A. Dayton, "Precision Manufacture of Phase-Change Perfluorocarbon Droplets Using Microfluidics," *Ultrasound in Medicine and Biology,* vol. 37, no. 11, pp. 1952-1957, 2011.

[10] M. Zhang, M. L. Fabiilli, K. J. Haworth, J. B. Fowlkes, O. D. Kripfgans, W. W. Roberts, K. A. Ives and P. L. Carson, "Initial Investigation of Acoustic Droplet Vaporization for Occlusion in Canine Kidney," *Ultrasound in Medicine & Biology,* pp. 1691-1703, 2010.

[11] H. K. Chang, L. Delaunois, R. Boileau and R. R. Martin, "Redistribution of Pulmonary Blood Flow During Experimental Air Embolism," *The American Physiological*

Society, vol. 51, no. 1, pp. 211-217, 1981.

[12] H. Chang, M. Weber, J. Thompson and R. Martin, "Hydrodynamic Features of Pulmonary Air Embolism: A Model Study," *Journal of Applied Physiology,* vol. 47, p. 539–543, 1981.

[13] C. M. Muth and E. S. Shank, "Gas Embolism," *The New England Journal of Medicine,* vol. 342, no. 7, pp. 476-482, 2000.

[14] A. J. Calderon, J. B. Fowlkes and J. L. Bull, "Bubble Splitting in Bifurcating Tubes: A Model Study of Cardiovascular Gas Emboli Transport," *Journal of Applied Physiology,* vol. 99, pp. 479-487, 2005.

[15] D. T. Valassis, R. E. Dodde, B. Eshpuniyani, J. B. Fowlkes and J. L. Bull, "Microbubble Transport Through a Bifurcating Vessel Network with Pulsatile Fow," *Biomedical Microdevices,* vol. 14, pp. 131-143, 2012.

[16] A. J. Calderon, Y. S. Heo, D. Huh, N. Futai, S. Takayama, J. B. Fowlkes and J. L. Bull, "Microfluidic Model of Bubble Lodging in Microvessel Bifurcations," *Applied Physics Letters,* vol. 89, pp. 244103-1-3, 2006.

[17] S. Samuel, A. Duprey, M. L. Fabiilli, J. L. Bull and J. B. Fowlkes, "In Vivo Microscopy of Targeted Vessel Occlusion Employing Acoustic Droplet Vaporization," *Microcirculation,* vol. 19, pp. 501-509, 2012.

[18] T. Ye and J. L. Bull, "Direct Numerical Simulations of Micro-Bubble Expansion in Gas Embolotherapy," *Journal of Biomechanical Engineering,* pp. 126: 745-759, 2004.

[19] T. Ye and J. L. Bull, "Microbubble Expansion in a Flexible Tube," *Journal of Biomechanical Engineering,* pp. 128: 554-563, 2006.

[20] B. Eshpuniyani, J. B. Fowlkes and J. L. Bull, "A boundary element model of microbubble sticking and sliding in the microcirculation," *International Journal of Heat and Mass Transfer,* p. 51: 5700–5711, 2008.

[21] A. J. Calderon, B. Eshpuniyani, J. B. Fowlkes and J. L. Bull, "A Boundary Element Model of the Transport of a Semi-Infinite Bubble Through a Microvessel Bifurcation," *Physics of Fluids,* vol. 22, no. 061902, pp. 1-11, 2010.

[22] C. E. Riva, J. E. Grunwalk, S. H. Sinclair and B. L. Petrig, "Blood Velocity and Volumetric Flow Rate in Human Retinal Vessels," *Ingestigative Ophthalmology & Visual Science*, vol. 26, no. 8, pp. 1124-1132, 1985.

[23] C. A. Brebbia, Boundary Elements: An Introductory Course, UK: WIT Press, 1992.

[24] C. Pozrikidis, Boundary Integral and Singularity Methods for Linearized, Cambridge University Press, 1992.

[25] H. P. Greenspan, "On the Motion of a Small Viscous Droplet That Wets a Surface," *The Jounal of Fluid Mechanics,* vol. 84, no. 1, pp. 125-143, 1978.

[26] C. A. Powell and M. D. Savage, "Numerical Simulation of Transient Free Surface Flow with Moving Contact Lines," *Communications in Numerical Methods in Engineering,* Vols. 581-588, p. 17, 2001.

[27] C. A. Powell, M. D. Savage and J. T. Guthrie, "Computational Simulation of the Printing of Newtonian Liquid from a Trapezoidal Cavity," *International Journal of Numerical Methods for Heat and Fluid Flow,* vol. 12, no. 4, pp. 338-355, 2002.

CHAPTER VI: ACOUSTIC ATOMIZATION PROCESS WITHIN BUBBLES ATTACHED TO A SOLID BOUNDARY

Introduction

The coupling of ultrasound and micro/nano-emulsions is a growing area of interest in biomedical applications. Examples of ultrasound and micro/nano-bubbles applied to biomedical applications currently include histotripsy, lithotripsy, contrast agents, drug delivery, and gas embolotherapy[1-9]. In all of these applications control over acoustic parameters to elicit or limit a specific bubble response is integral to controlling bioeffects and designing an effective treatment. The complex behavior of bubble dynamics due to an acoustic field includes bubble oscillation, resonance, jet formation, inertial cavitation, and etc. all of which have direct impact on the safety and efficacy of treatments[10-14]. Furthermore, processes occurring at fluid interfaces that are excited by acoustic energy may help probe phenomena such as sonoporation, which is when the permeability of the cell is transiently increased through the use of ultrasound often times enhanced using contrast agents[5, 15, 16].

The study of free-surfaces responding to an oscillating pressure field has a rich history dating back to Faraday 1831[17] and Rayleigh 1896[18]. These early studies focused on surface wave patterns formed and prediction of wavelength to oscillating frequency. Lang in 1962 was the first to experimentally observe that at sufficient oscillation amplitudes the

cresting formed by such waves resulted in droplet atomization[19]. Empirically, Lang 1962 was able to find that the droplet diameter, D, ejected scaled according to

$$D = 0.34\left(\frac{8\pi\sigma}{\rho f^2}\right)^{1/3} \quad (1)$$

where ρ is the density, σ is surface tension, and f is the driving frequency[19]. Since Lang's work several other studies have expanded on the topic of droplet atomization and several theoretical analyses have also been carried out[20-23]. Typically investigations of these atomization processes are limited to liquid films or large droplets on a vibrating plate. More recent work by Simon *et al.* 2012 have shown that similarly to Faraday waves, the generation of capillary waves along an air/tissue interface from the shock scattering of acoustic waves may serve as the mechanical driving force behind tissue fractionation observed in histotripsy[24]. Simon *et al.* 2012 was able to show in planar conditions comparing an air/tissue versus an air/water interface the atomization processes shared similar characteristics[24]. Furthermore, the tissue atomization process was found to be not geometrically limited and can be reproduced when a tissue cavity (simulating the curved interface from a bubble in tissue) is present[24]. Limited experimental data exists on conditions required to initiate the atomization event within a bubble in a liquid environment. The purpose of this investigation was to study a secondary instability that results in an atomization of the bulk fluid within a bubble initiated by single acoustic pulses. This instability occurs at lower acoustic pressure than the pressure threshold necessary to cause jet formations and inertial cavitation. Understanding the dynamics of this atomization process may provide further insight into the driving mechanism behind histrotripsy or other bioeffects related to ultrasound with micro-/nanobubble therapies.

Methods

Experimental Setup

Isolated bubbles were carefully placed on the base of an acrylic tank containing degassed bulk fluid. The tank was mounted on an inverted microscope stage (Nikon Eclipse TE2000-S, Nikon, Melville, NY) to provide a bottom up view looking through the bubble. The single element focused transducers used were mounted confocal to the microscope objected and held at a 40° from the horizontal plane using a custom machined micro-positioning system fixed to the microscope. A Photometrics camera (Roper Scientific, Tuscon, AZ, USA) was used in combination with 2x, 4x, 10x, 20x, and 40x objectives with an additional 10x internal microscope magnification to record images.

High Speed Camera Setup

A side view was used for many of the high-speed camera experiments of the spray forming (Figure 6.1). A bubble was carefully placed on a side mounted sheet of acrylic (evergreen scale models, Woodinville, WA, USA). The ultrasound transducer was positioned using micro-positioners and held at a 40° from the horizontal plane, which provided the same arrangement as the aforementioned setup. The Photometrics microscope camera was replaced by a Phantom v210 high speed camera (Vision Research Inc., Wayne, NJ, USA) which provided frame rates up to 128,000 FPS using a cropped field of view. The ultrasound trigger was synced with the high-speed camera in order to resolve events relative to the firing of the transducer. In order to provide sufficient light for high speed imaging, an arc lamp (MB01, Techniquip Corp., Pleasanton, CA, USA) coupled to a fiber optic bundle was used to illuminate the field of view.

Acoustics

Two geometrically similar transducers were used throughout the experiments to help characterize the effects of frequency on the dynamics of the system. Both transducers used were f/2, 0.75 in (19 mm) diameter single element transducers with. The driving frequencies of the two respective transducers were 3.5 MHz (Panametrics A381S) and 7.5 MHz (Panametrics A321S, Olympus, Waltham, MA, USA). Unless otherwise specified, single pulses of 15 cycles were used to cause the atomization event. The transducers were driven using a function generator (HP 3314A, Hewlett-Packard, Palo Alto, CA, USA) producing a N-cycle sine wave pulse amplified by a Ritec GA-2500-A amplifier (RITEC Inc., Warwick, RI, USA) and monitored using a WaveSurfer 44MXs oscilloscope (Teledyne LeCroy, Chestnut Ridge, NY, USA). An Aligent 33120A (Agilent Technologies, Santa Clara, CA, USA) was used as a gate for the amplifier and trigger for the HP 3314A function generator and oscilloscope. A schematic of the electronics can be seen in figure 6.1.

Both single element transducers were calibrated to obtain acoustic pressure data at the focal point using a fiber optic hydrophone designed according to Parsons *et al.* 2006[25] on an optical isolating table. Hydrophone measurements indicated noticeable elevated peak positive pressure (PPP) relative to (PNP). The asymmetry in the acoustic output is due to the non-linear acoustic behavior from the f/2 geometry and relatively high pressure amplitudes. As a result of this non-linear output, high order harmonics are present at the focal spot and are most concentrated along the centerline of the focal spot. In order to better understand the contributing acoustic factors to the atomization process, acoustic filters were added to see the effects of augmenting the acoustic field. Single sheets of 25 μm thick aluminum (McMaster-Carr Co., Elmhurst, Illinois) and 75 μm thick brass rolled sheets

(McMaster-Carr Co., Elmhurst, Illinois) were placed 5 mm away from the focal spot on a custom holder attached to the transducer. This approach has been used to reduce peak positive pressures (PPP) by filtering higher harmonics and maintaining peak negative pressures (PNP) by Maxwell *et al.* 2011 during the investigation of contributions of PPP relative to PNP during the initiation of bubble cloud formation during histotripsy[4]. Hydrophone measurements confirmed that the use of the holder with no filter in place had no effect on acoustic field.

Test Fluids

A combination resulting in three fluid conditions were used to elucidate the factors that influence the onset of atomization. The primary condition tested was an air bubble in a degassed deionized (DI) water bath at room temperature. The second condition used to investigate used dodecafluoropentane (DDFP, C_5F_{12}, CAS #: 678–26–2) gas bubbles in degassed DI water held at body temperature (37°C) and air bubbles in a DI water/Tween 20 solution at room temperature. DDFP bubbles were generated by using the ultrasound transducer to vaporizing liquid DDFP microdroplets to form DDFP bubbles. The DDFP microdroplets were generated through high speed shaking liquid DDFP with a bovine serum albumin and saline solution using an amalgamator. Details on the droplet formulation can be found in Kripfgans *et al.* 2000 [1]. The last combination used was air bubbles in the Tween 20 (CAS No. 9005-64-5, Sigma-Aldrich, St. Louis, MO). The solution was mixed at a 3.3 mM to ensure that the concentration of Tween 20 at the free surface of the bubble was well beyond the saturation point[26, 27]. The Tween 20 and DI water solution was degassed by using a vacuum pump. The surface tension at the gas liquid interface was assumed to be 72,

70, and 37 dynes/cm for air/water[26], PFC/water[28], and air/Tween 20 solution[26, 27] respectively.

Results and Discussion

Using single pulses from a 3.5 and 7.5 MHz transducer an atomization process was observed within bubbles attached to a solid boundary. A common bubble response to a high intensity acoustic pulse is similar to what is shown in figure 6.2A, the bubble responses to the propagating wave by creating an invagination that impinges on the rigid surface. These liquid jets (Figure 6.2A, frames 4-8) have been known to travel at velocities on the order of meters per second causing pitting or erosion[6, 14]. If the acoustic pulse is reduced from 120 cycles (Figure 6.2A) to 15 cycles (Figure 6.2B) the formation of the jet can be suppressed. In Figure 6.2B frames 3-8 a spray of small water microdroplets are visible. The plume of droplets travels downward in the direction of the acoustic pulse. The mist of droplets generated from the acoustic pulse continue to propagate in a narrow stream until it approaches near the boundary 218 microseconds (Figure 6.2B, frame 7) after the acoustics are activated at which the mist near the boundary begins to spread out and move outward radially and continues to do so until gravity forces the droplets to settle down. In both short (15 cycle) and long (120 cycle) pulses, the deformation of the bubble is minimal and fragmentation of the bubble was never observed. During the investigation a similar atomization process was brought to our attention and has been proposed as a mechanism behind the emulsification of tissue during HIFU ablation of soft tissue[24]. Simon *et al.* 2012 concluded that formation of a drop chain in the gas phase was required prior to atomization from taking place[24]. Furthermore, the drop chain was on the order of 2 mm in length when atomization was observed. However, because of the light distortion from the mismatch in

refractive index, it is unclear if a drop chain must be present for atomization to occur as documented by Simon *et al.* 2012[24]. Regardless, the atomization events observed in our gas bubble/liquid environment results in a narrow band of propagating droplets, as opposed to the explosive erosion events observed in tissue erosion. Furthermore, the bubble diameters where atomization was observed covered a range from single micrometer bubbles up to millimeter sized bubbles. These bubble were much smaller than Simon *et al.* 2012 proposed requirement of a millimeter scale acoustic fountain to form prior to atomization[24]. These differences in observations were likely due to the much shorter acoustics pulses used in this study lasting 2-4 microseconds versus millisecond long pulses used by Simon *et al.* 2012[24].

The threshold for an array of bubble diameters for a single acoustic pressure of 15 cycles at 3.5 MHz and 7.5MHz were determined by incrementally increasing input voltage to the transducer and using hydrophone data to estimate the equivalent pressure at the focal spot. Results consistently show a trend that threshold pressures to generate the spray are relatively constant for larger bubbles and as bubble diameters decrease the threshold decreases in a logarithmic fashion (Figure 6.3A). Using PNP as a metric for acoustic pressure required for threshold for atomization, it was observed that the threshold was lower using the 3.5 MHz transducer than the 7.5 MHz. Furthermore, the ability to generate the spray was not limited to a condition for bulk fluid wavelength to bubble diameters. Indications of generation of the spray were observed over a wavelength in water to bubble diameter range covering 0.04-6 wavelengths.

The logarithmic behavior in the threshold for smaller bubbles (Figure 6.3A) is likely due to curvature of the bubble and contributions from the Laplace pressure. This is a logical conclusion considering that as bubble diameter increases, contributions from the Laplace

pressure diminishes with 1/R until the limit of an infinitely large bubble which would simulation a flat interface. The diminishing effect from curvature would explain why for larger bubbles the threshold appears to approach a finite limit. If one attempts to normalize the threshold to collapse the data by scaling the acoustic pressure threshold according to Laplace threshold and rescaling bubble diameter according to wavelength (Figure 6.3B) it is seen that the logarithmic behavior seen in the raw measurements is eliminated and the data is linearized, confirming that bubble curvature could be the primary contributing factor in the logarithmic behavior in the threshold in figure 6.3A. However, the scaling fails to pull the data into a single predictable trend line. Alternatively, if the data is scaled according to mechanical index, MI=PNP/$f^{0.5}$ where PNP is peak negative pressure and f is the carrier frequency, divided by curvature ($\varkappa$) (Figure 6.3C) the data is linearized and collapses to a single line. A linear regression of all the data can be plotted through the MI/$\varkappa$ scaled results providing slope of 0.4225, an R-squared of 0.99. The scaling suggests that the actual values of surface tension used had minimal effect on the threshold of atomization.

Due to the narrowness of the atomized spray (Figure 6.2B), a question arose of whether PPP and the presence of higher harmonics may have been the driving force behind the atomization versus PNP. In order to help answer this question the acoustic field at the focus was augmented using a thin sheet of aluminum or brass. Both materials had an effect on the higher harmonics and PPPs of the 3.5 MHz transducer which could be seen in both the transient signal and the FFT (Figure 6.4). Although the use of brass had a substantial effect on PNP and the carrier frequency, increasing input power could easily compensated and a greater reduction of relative PPP and higher harmonics could be maintained at an equivalent PNP. The results of the threshold for atomization in free field and acoustic

filtered conditions were plotted according to PPP and PNP as well as the normalized forms according to Laplace pressure (Figure 6.5). Multiple linear regression was used in MATLAB (MathWorks, Natick, MA) to obtain pairwise comparison across the aluminum versus free field and brass versus free field results for both PNP and PPP. The presences of the two respective filters were treated as categorical data for the statistical analysis. The regression revealed that the use of aluminum or brass compared to free field measurements had no effect on the PNP threshold with P-values of 0.6422 and 0.7332. However, significance was observed when comparing the PPP values for brass versus free field with a P-value of <2E-16 but not for aluminum versus free field with a P-value of 0.1137. The data in Figure 6.5 show that although the PPP aluminum threshold is appears to be lower than the free field measurements the free-field PPP and aluminum PPP thresholds are still statistically similar. Because of the statistically equivalent PNP thresholds with and without the acoustic filters and the statistical difference between PPP threshold measurements under free-field and brass filtering, it was concluded that PNP amplitudes are the dominating force driving atomization. Because the carrier frequency is the dominant frequency component and the higher harmonics have little influence on PNP amplitudes, it is likely that PNP is providing a lower limit for energy required to exciting capillary waves along the bubble/liquid interface.

After isolating a large bubble on the order of 1 mm in diameter, sequences of images were taken at high magnification to image the droplets created from the atomization process using both the 3.5 and 7.5 MHz transducer. Using MATLAB an image threshold based edge detect script was used to measure the size of the droplets generated from atomization. Threshold consistency was verified by manually measuring droplet diameters for a subpopulation of droplets in the images collected. Plotting the resulting mean droplet

diameter versus acoustic power (Figure 6.6) indicates that the droplet diameter does not vary with acoustic power but rather with frequency. Linear regressions of the data yield lines of essentially zero slope and R-square <1E-4 for both frequencies. The low R-squared is a result of the low correlation between acoustic power and resulting droplet diameter suggesting that atomized droplet diameters are constant for a given driving frequency. The mean diameters generated from the 3.5 and 7.5 MHz transducers across the pressures tested were 2.06 μm (STD=0.63 μm) and 1.24 μm (STD=0.42 μm) respectively. According to Lang's empirically derived relationship, the mean population at 3.5 MHz should be 1.80 μm and 1.08 μm at 7.5 MHz[19]. The 13% discrepancy falls within one standard deviation of measured droplet diameters. Considering the consistency between the mean diameters of droplets ejected using the two frequencies and Lang's empirical results, it appears that the phenomena could be a result of Faraday waves forming along the gas-liquid interface. A K-S test for normality of the droplet distributions (Figure 6.7) measured from the atomization concluded that both transducers generate droplets can be considered a normal distribution. A T-test of the distribution of droplets produced from two transducer frequencies (Figure 6.7) concluded that the two samples are independent. The coefficients of variation of the two populations are 30.7% for the 3.5 MHz transducer and 33.7% for 7.5 MHz, therefore the resulting populations may not be considered monodisperse.

Conclusions

The threshold for atomization of bulk fluid into a gas bubble attached to a solid boundary due to short acoustic pulses was shown to occur linearly with bubble diameter after compensating for bubble curvature. After measuring acoustic thresholds for the atomization after augmenting the acoustic field it was found that the event scales more

consistently using PNP rather than PPP. The resulting droplets distributions do not vary with acoustic power, but rather fit reasonably against the empirical results from Lang 1962[19]. This suggests that the phenomena may be a result of Faraday waves forming along the bubble interface causing droplets from the bulk fluid to pinch off and form the droplets seen within the bubble. Although the environment is vastly different from histotripsy, the atomization process does share similarities to the tissue fraction results documented by Simon *et al.* 2012[24]. In lieu of Simon *et al.* 2012 results, it is conceivable that the oscillation or capillary waves along the bubble interface resulting in the observed atomization may play a role in the mechanism driving sonoporation. Several groups have suggested that sonoporation is driven by the inertial cavitation of contrast agents[5, 15, 16]. From the high speed imaging results, the atomization event can be generated independent of the class bubble jet impinging on an interface. If a microbubble is attached to a vessel one can imagine that one mechanism resulting in a temporary perforation of the vessel resulting in increased permeability could be due to a high intensity pulse generating a jet that perforates the vessel wall and drives material in the bulk fluid into the interstitium, which is similar to the mechanisms often described[5, 15, 16]. Alternatively, perhaps sonoporation can be driven by small amplitude oscillations of the bubble attached to the wall causing wall shear along the endothelium, allowing for increased vessel permeability, combined with the atomization process independent of the jet delivering smaller droplets of the bulk fluid which can then contact the transiently more permeable vessel wall.

Chapter VI: Figures

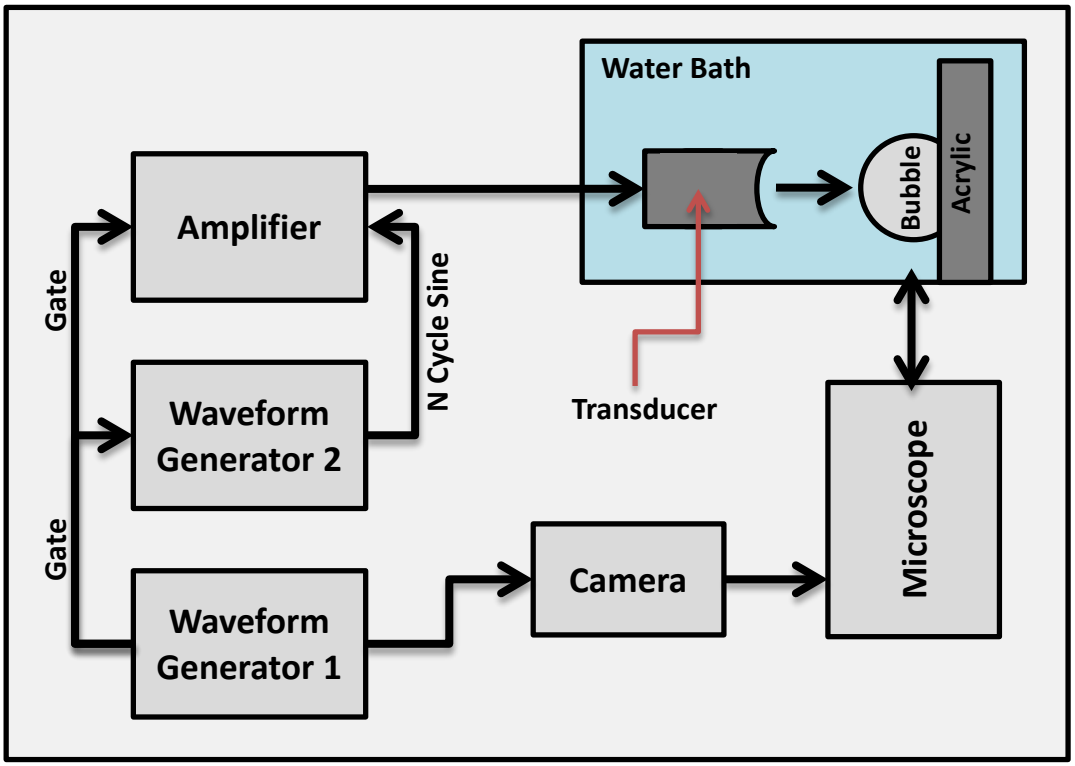

Figure 6. 1: Basic schematic of the experimental setup. An N-cycle sine wave input was generated by a waveform generator and amplified using a pulse amplifier prior to transmission to the focused transducer. Triggering of a high speed camera, waveform generator, and the pulse amplifier was controlled with a waveform generator. An inverted microscope had a degassed water bath containing the attached bubble mounted on the viewing stage.

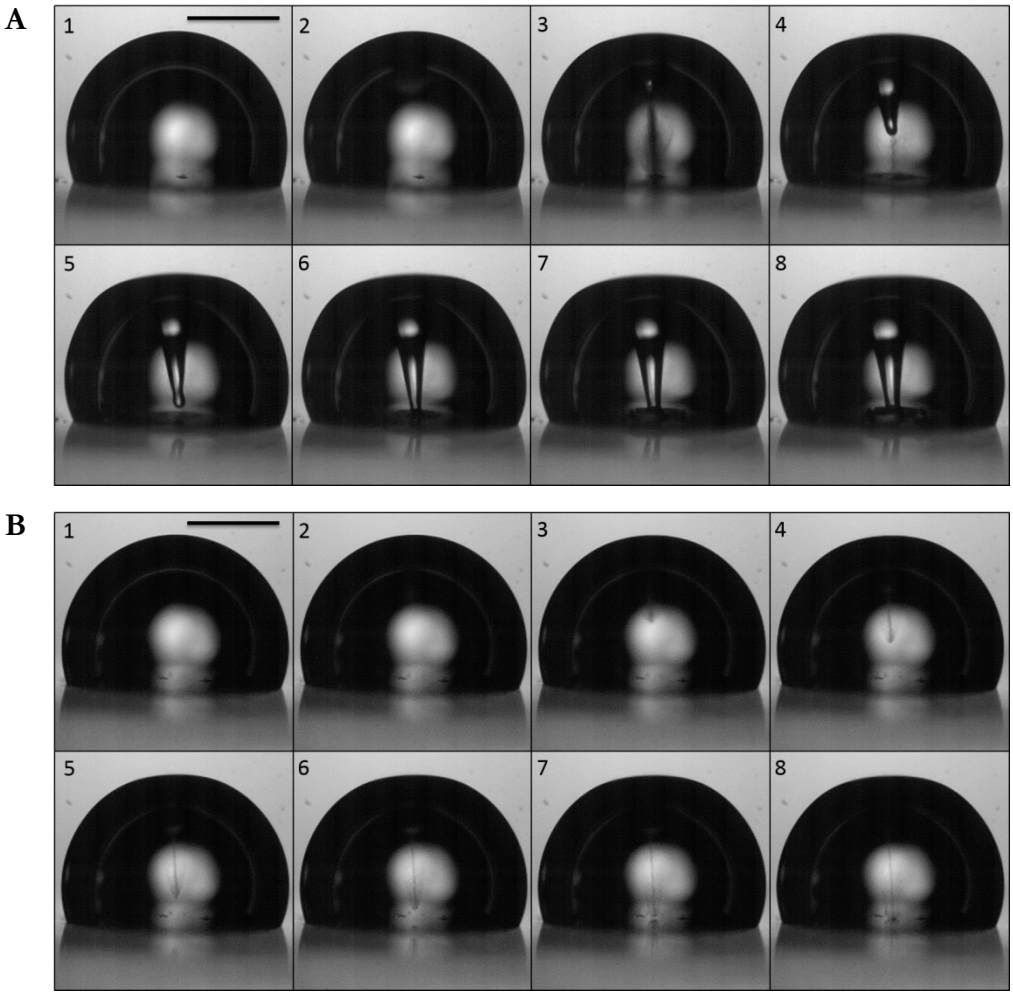

Figure 6. 2: A 1.2 mm diameter bubble in water is responding to a single acoustic pulse generated from a 7.5 MHz transducer at 4.4 MPa peak negative pressure with (A) 120 cycles and (B) 15 cycles. Frames 1 through 8 correspond to T=0, 36, 72, 108 144, 180, 216, and 288 μs after the acoustics have arrived to the bubble. The scale bar in frame 1 represents 500 μm. (A) In frame 3 the spray is generated followed by a microjet, shown in frames 4-8. (B) In frame 3 a spray of small water microdroplets are visible. The plume of droplets travels downward in the direction of the acoustic pulse.

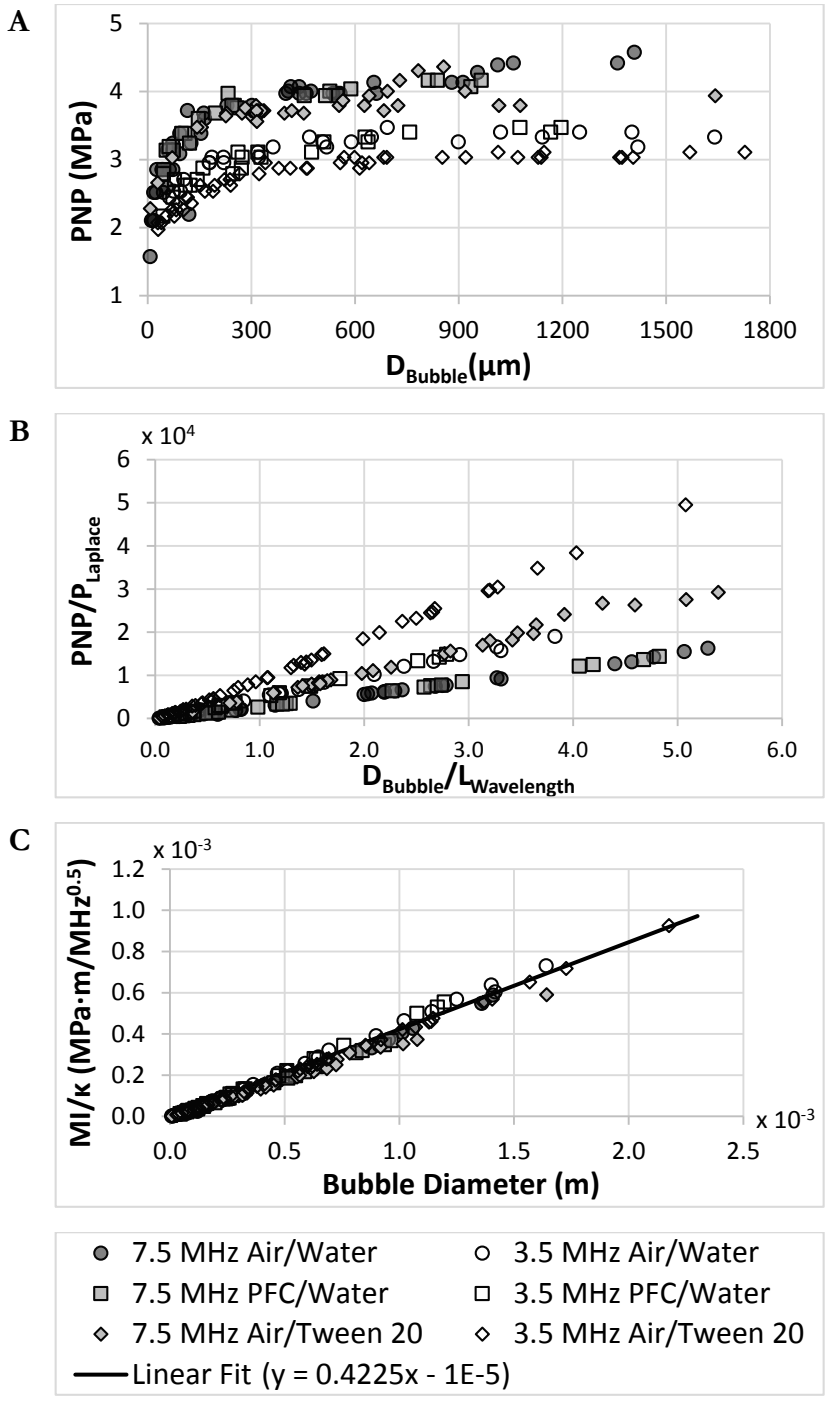

Figure 6. 3: Threshold to initiate atomization (A) PNP versus bubble diameter (B) non-dimensional pressure versus non-dimensional length and (C) MI/$\varkappa$ versus bubble diameter. Acoustic pressure or MIs greater than the measured threshold for a given bubble diameter resulted in atomization. Lower acoustic energies delivered resulted in oscillation of the bubble. The data can be collapsed and linearized if the threshold is scaled according to MI/$\varkappa$. The linearly is likely due to the Laplace pressure. However, the actual surface tension appears to have little influence on threshold.

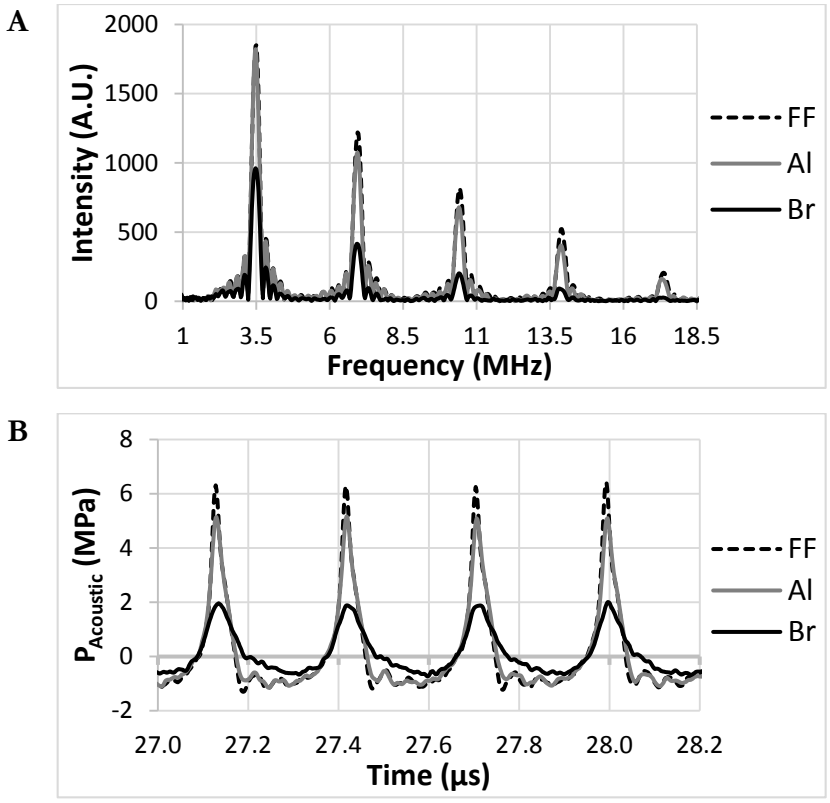

Figure 6. 4: (A) Frequency and (B) time response of the 3.5 MHz transducer in free field (FF) conditions as well as with a single sheet of Aluminum (Al) or Brass (Br) 5mm from the focal spot. The addition of the aluminum or brass promoted reduction in the higher harmonics thus reducing the amplitude of the peak positive pressures.

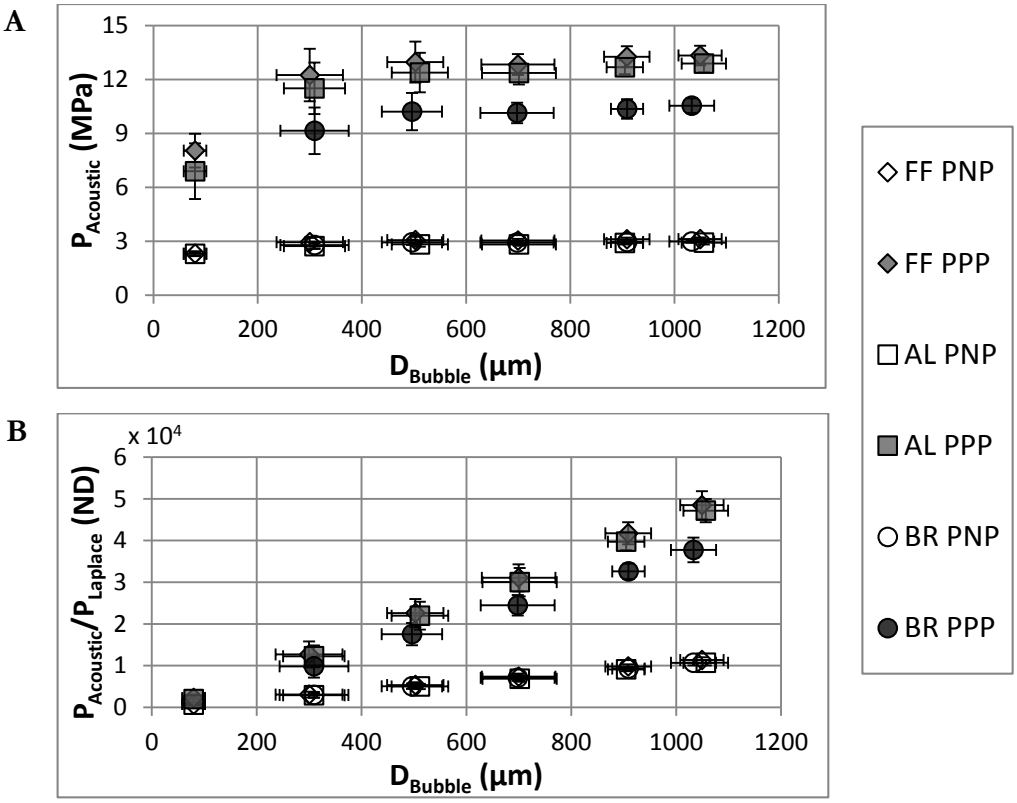

Figure 6. 5: Positive and negative acoustic pressures at threshold of atomization as a function of bubble diameter. Threshold for atomization scales more consistently with negative pressures rather than positive pressures.

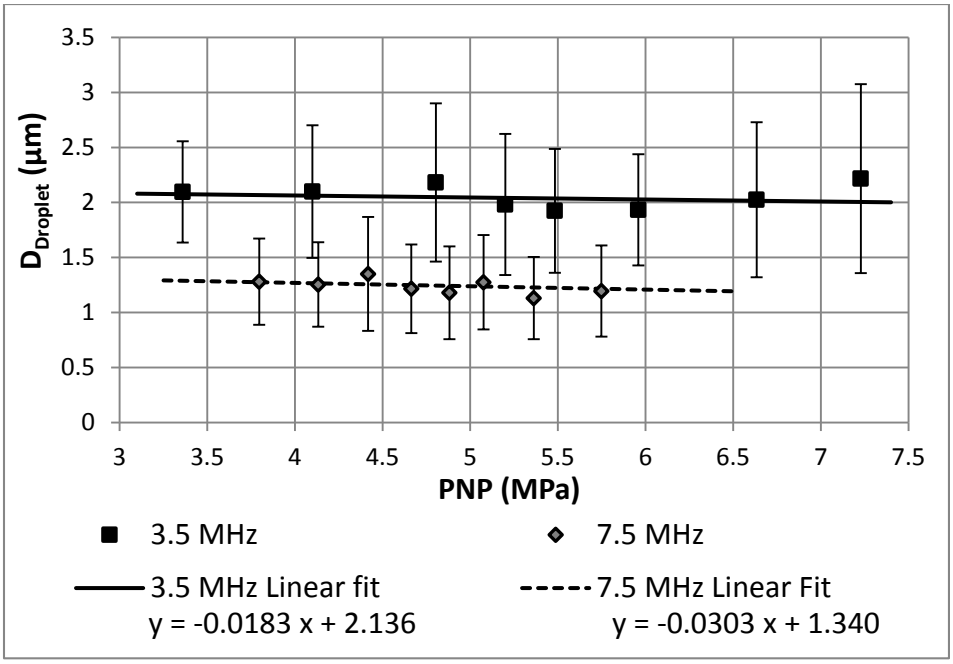

Figure 6. 6: Atomized droplet distribution as a function of power using single pulses from the 3.5 and 7.5 MHz transducer as a function of PNP. Both transducers show low correlation between acoustic power and droplet distribution created which can be confirmed through the low R-squared, both of which were <1E-4.

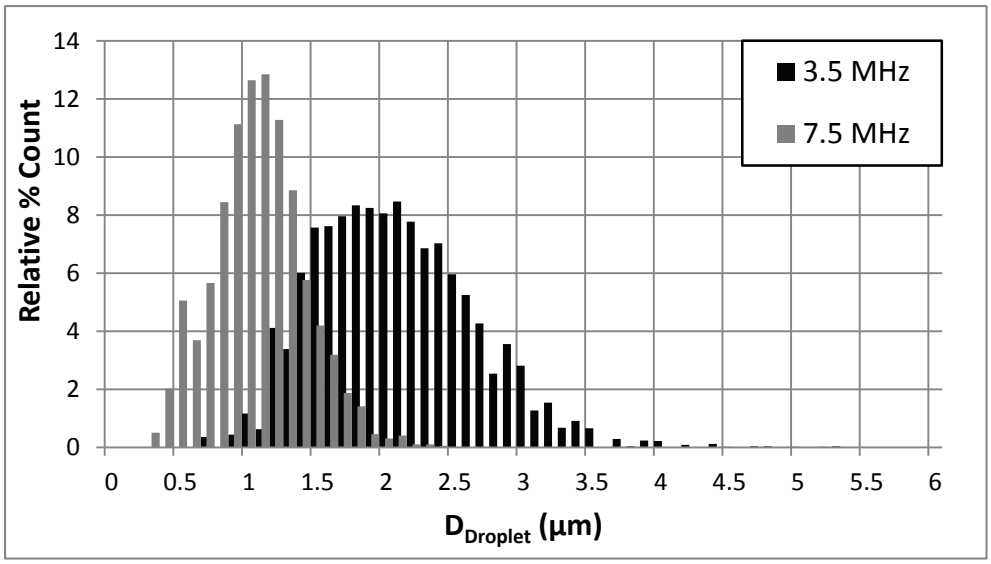

Figure 6. 7: Representative distribution of droplets resulting from atomization process comparing droplet populations generated from the 3.5 MHz transducer and the 7.5 MHz.

Chapter VI: References

[1] O. D. Kripfgans, J. B. Fowlkes, D. L. Miller, O. P. Eldevik and P. L. Carson, "Acoustic Droplet Vaporization for Diagnostic Applications," *Ultrasound in Medicine and Biology,* p. 26(7): 1177–1189, 2000.

[2] M. L. Fabiilli, K. J. Haworth, I. E. Sebastian, O. D. Kripfgans, P. L. Carson and J. B. Fowlkes, "Delivery of Chlorambucil Using Acoustically-Triggered Perfluoropentane Emulsion," *Ultrasound in Medicine & Biology,* vol. 36, no. 8, pp. 1364-1375, 2010.

[3] N. Rapopart, K.-H. Nam, R. Gupta, Z. Gao, P. Mohan, A. Payne, N. Todd, X. Liu, T. Kim, J. Shea, C. Scaife, D. L. Parker, E.-K. Jeong and A. M. Kennedy, "Ultrasound-Mediated Tumor Imaging and Nanotherapy Using Drug Loaded, Block Copolymer Stabilized Perfluorocarbon Nanoemulsions," *Journal of Controlled Release,* vol. 153, pp. 4-15, 2011.

[4] A. D. Maxwell, T.-Y. Wang, C. A. Cain, J. B. Fowlkes, O. A. Sapozhnikov, M. R. Bailey and Z. Xu, "Cavitation Clouds Created by Shock Scattering from Bubbles During Histotripsy," *Journal of the Acoustical Society of America,* vol. 130, no. 4, p. 1888–1898, 2011.

[5] K. Ferrara, R. Pollard and M. Borden, "Ultrasound Microbubble Contrast Agents: Fundamentals and Application to Gene and Drug Delivery," *Annual Review of Biomedical Engineering,* vol. 9, pp. 415-447, 2007.

[6] T. Kodama and Y. Tomita, "Cavitation Bubble Bahavior and Bubble-Shock Wave Interaction Near a Gelatin Surface as a Study of in Vivo Bubble Dynamics," *Applied Physics B: Lasers and Optics,* vol. 70, pp. 139-149, 1999.

[7] J. L. Bull, "Cardiovascular Bubble Dynamics," *Critical Reviews in Biomedical Engineering,* p. 33(4): 299–346, 2005.

[8] J. L. Bull, "The Application of Microbubbles for Targeted Drug Delivery," *Expert Opinion on Drug Delivery,* vol. 4, no. 5, pp. 475-493, 2007.

[9] Z. Z. Wong and J. L. Bull, "Microbubbles and Microdroplets for Drug Delivery," *Journal of Drug Delivery, Science, and Technology,* vol. 21, no. 5, pp. 355-367, 2011.

[10] C. E. Brennen, Cavitation and Bubble Dynamics, New York, New York: Oxford University Press, 1995.

[11] W. Lauterborn and C.-D. Ohl, "Cavitation Bubble Dynamics," *Ultrasonic Sonochemistry,* vol. 4, pp. 65-75, 1997.

[12] O. Lindau and W. Lauterborn, "Cinematographic Observation of the Collapse and Rebound of a Laser-Produced Cavitation Bubble Near a Wall," *Journal of Fluid Mechanics,* vol. 479, pp. 327-348, 2003.

[13] E. Johnsen and T. Colonius, "Numerical Simulations of Non-Spherical Bubble Collapse," *Journal of Fluid Mechanics,* vol. 629, pp. 231-262, 2009.

[14] J. R. Blake, G. S. Keen, R. P. Tong and M. Wilson, "Acoustic Cavitation: The Fluid Dynamics of Non-Spherical Bubbles," *Philisophical Transactions of The Royal Society A,* vol. 357, pp. 251-267, 1999.

[15] D. L. Miller, S. L. Pislaru and J. F. Greenleaf, "Sonoporation: Mechanical DNA Delivery by Ultrasonic Cavitation," *Somatic Cell and Molecular Genetics,* vol. 27, no. 1, pp. 115-134, 2002.

[16] S. Hernot and A. L. Klibanov, "Microbubbles in Ultrasound-Triggered Drug and Gene Delivery," *Advanced Drug Delivery Reviews,* vol. 60, no. 10, pp. 1153-1166, 2008.

[17] M. Faraday, "On a Peculiar Class of Acoustical Figures; and on Certain Forms Assumed by Groups of Particles upon Vibrating Elastic Surfaces," *Philosophical Transactions of the Royal Society of London,* vol. 121, pp. 299-340, 1831.

[18] B. J. W. S. Rayleigh, The theory of sound, Macmillan, 1896 Vol. 2.

[19] R. J. Lang, "Ultrasonic Atomization of Liquids," *The Journal of the Acoustical Society of America,* vol. 34, no. 1, pp. 6-8, 1962.

[20] K. Kumar, "Linear Theory of Faraday Instability in Viscous Liquids," *Journal of Fluid Mechanics,* vol. 279, pp. 49-68, 1994.

[21] R. L. Peskin and R. J. Raco, "Ultrasonic Atomization of Liquids," *The Journal of the Acoustical Society of America,* vol. 35, no. 9, pp. 1378-1381, 1963.

[22] A. Qi, L. Y. Yeo and J. R. Friend, "Interfacial Destabilization and Atomization Driven by Surface Acoustic Waves," *Physics of Fluids,* vol. 20, no. 7, pp. 074103-1-14, 2008.

[23] T. D. Donnelly, J. Hogan, A. Mugler, N. Schommer, M. Schubmehl, A. J. Bernoff and B. Forrest, "An Experimental Study of Micron-Scale Droplet Aerosols Produced via Ultrasonic Atomization," *Physics of Fluids,* vol. 16, no. 8, pp. 2843-2851, 2004.

[24] J. C. Simon, O. A. Sapozhnikov, V. A. Khokhlova, Y.-N. Wang, L. A. Crum and M. R. Bailey, "Ultrasonic Atomization of Tissue and its Role in Tissue Fractionation by High Intensity Focused Ultrasound," *Physics in Medicine and Biology,* vol. 57, pp.

8061-8078, 2012.

[25] J. E. Parsons, C. A. Cain and J. B. Fowlkes, "Cost-Effective Assembly of a Basic Fiber-Optic Hydrophone for Measurement of High-Amplitude Therapeutic Utrasound Fields," *Journal of the Acoustical Society of America,* vol. 119, no. 3, p. 1432–1440, 2006.

[26] L. S. Wan and P. F. Lee, "CMC of Polysorbates," *Journal of Pharmaceutical Sciences,* vol. 63, no. 1, pp. 136-137, 1974.

[27] M. R. R. Nino and J. R. Patino, "Surface Tension of Bovine Serum Albumin and Tween 20 at the Air–Aqueous Interface," *Journal of the American Oil Chemists' Society,* vol. 75, no. 10, pp. 1241-1248, 1998.

[28] A. Kabalnov, D. Klein, T. Pelura, E. Schutt and J. Weers, "Dissolution of Multicomponent Microbubbles in the Bloodstream: 1. Theory," *Ultrasound in Medicine and Biology,* vol. 24, no. 5, pp. 739-749, 1998.

CHAPTER VII: CONCLUSIONS AND FUTURE DIRECTIONS

Conclusions

The work presented and discussed in chapters two through six contributed to the understanding of the dynamics related to the acoustic droplet vaporization (ADV) process thus furthering the development of the gas embolotherapy in addition to other ADV and bubble based ultrasound therapies. Although there is a substantial body of work on the dynamics of bubbles in acoustic fields[1, 2], limited literature exists on the fluid dynamics of the ADV process, let alone in the context therapeutic applications.

The mechanism initiating the primary gas nucleus within the droplets due to ADV was investigated through the comparison of ultra-high speed imaging experiments to acoustic field simulations. Experimental results revealed a droplet material (dodecafluoropentane, DDFP) wavelength to droplet dependency on location of the primary gas nucleus formed within the droplet. Numerical simulations revealed that due to the short wavelength of the carrier frequency in DDFP, the acoustic field is refocused within large droplets ($D_{droplet}$>20 μm). The refocused acoustic field correlated well with the corresponding droplet sized primary gas nucleus found. Moving to small droplets ($D_{droplet}$<20 μm) acoustic field interactions from the oncoming wave and the reflected wave from the back of the droplet had a strong influence on the location where the highest PNP was developed. Results also suggested that the vaporization of droplets much smaller than

the wavelength DDFP may be more influenced by sufficiently high pressure amplitudes of the higher harmonics present in the acoustic wave. The conclusion was that the primary mechanism behind ADV is a cavitation-like event occurring within the droplets due to the acoustic field developed within the droplets. This suggests that the hypothesis of a cavitation event occurring outside the droplet triggering vaporization, proposed by Giesecke and Hynynen 2006, is less likely to take place[3]. Because acoustic cavitation occurs independently from the onset of ADV, potential tissue damage incurred during ADV is unlikely to occur due to nucleation.

With previous ADV ultra-high speed imaging experiments focusing on the sub-microsecond time-scale events of nucleation or several hundred microsecond dynamics of bubble expansion, details on the intermediate time-scales were yet to be observed. Ultra-high-speed imaging of the first seven microseconds after nucleation revealed previously unseen dynamics of possible bubble collapse resulting in toroidal bubbles. The presumed formation of a liquid jet perforating the bubble followed by the pinch off of a section of the bubble toroid was assumed to have potentially damaging consequences independent of acoustic cavitation. However, modulation of acoustic pressure and pulse length can help reduce the likelihood of bubble torus formation and possible cell injury[4]. Tissue damage due to bubble torus formation is best avoided during ADV when pulse lengths are sufficiently short (i.e. less than one microsecond). Although potentially damaging bubble dynamics can be avoided at longer pulse lengths by reducing acoustic pressures, it does not guarantee the elimination of bubble torus formation.

Previous attempts at experimentally visualizing ADV expansion have typically been performed using relatively large microchannels compared to the droplet. Although damping

effects on bubble expansion has been observed, the resulting bubbles generated have never been shown to come into contact with the wall. In an effort to replicate idealized conditions encountered during gas embolotherapy, ADV experiments monitoring bubble expansion in microchannels from 25 to 100 μm in diameter were carried out and compared to conditions where bubble expansion was unconstrained. It was found that droplet diameter to channel diameter ratio played a great influence on the limiting the expansion rate of the droplet. Viscous resistance from the narrowness of the channel diameter caused severely damp the expansion rates observed in channels versus in free field. However, geometric constraints of the channel meant that bubble expansion in cases where the bubble contacted the wall, would result in plug like expansion of the bubble in the channel generating a high velocity Poiseuille flow with a constant shear along the channel wall. This is in contrast to the radially decaying velocity field from unconstrained bubbles which would be limited to damaging tissue near the expanding bubble vicinity. However, it was concluded that depending on intended vessel insonation size droplet size distributions can likely be made in such a way to balance vessel occlusion and limit potential vessel damage and possibly avoid damage altogether.

Moving from the nano- and microsecond details of nucleation and bubble dynamics questions of bubble transport and possibly secondary effects of additional acoustic waves interacting with the bubbles were considered in chapters five and six. A boundary element model investigating a microbubble sliding along a vessel wall towards a bifurcation was simulated. It was concluded that adhesion forces from bubble contact to the wall greatly influences transport velocity and potential of the bubble to lodge at bifurcation points. The geometry of the bifurcation itself appeared to play a large role in small bubbles remained

stuck at the bifurcation and enhanced larger bubble to develop possible additional wall adhesion points, promoting possibly vessel lodging. The results found are in support of bubble lodging patterns observed in microchannel bifurcation as well as those found during ADV in vitro experiments. Furthermore, functionalized bubbles would be less likely to travel downstream if they attach to the vessel wall and approached tortuous vessels and bifurcation points.

Although atomization events at planar gas/liquid interfaces have been investigated in great detail, atomization events in gas bubbles has never been characterized[5-12]. Traditionally, bubble collapse in the form of developing high velocity jets are observed when bubbles are exposed to high intensity ultrasound pulses[13-15]. It was determined that although atomization events precedes liquid jet formation, the atomization event can occur independent of jet formation so long as the pulse length is sufficiently short. Threshold for the atomization event not only occurs at low pressure thresholds than acoustic cavitation, but also is reduced as bubble diameter is reduced. The threshold was found to scale linearly to $MI/\varkappa$ and was also statistically shown to be limited by PNP rather than peak positive pressures. The droplets results from the atomization process, found in the bubble, had statistically no dependency on acoustic power. The droplet distribution generated was statistically different between the 3.5 MHz and the 7.5 MHz transducers and were within reason of the empirically predicted values droplet diameter relationship found by Lang in 1962[7]. It was concluded that the atomization process is likely from the development of capillary waves along the surface of the bubble, which at sufficient pressure amplitudes would result in droplet ejection. These results not only mirror the possibly dynamics seen

during tissue fractionation from histotripsy[11], a potential new explanation to sonoporation or avenue to investigate drug delivery has been introduced.

Summary of Scientific Contributions

The dynamics from the ADV process span the nanosecond timescale processes up to the minute or hour timescale when bubble transport, mass transport, etc. can take place. A variety of bubble and droplet dynamics were explored throughout the dissertation beginning with the initial vaporization process, moving through the expansion process, followed by the subsequent bubble transport and possible atomization events occurring within the bubble. A list of key contributions to the development of gas embolotherapy and the understanding of the ADV process are listed as follows:

- The ADV process is initiated by a cavitation-like event within the bubble which has a wavelength to droplet diameter dependency.
- The wavelength to droplet diameter dependency explains the transition in nucleation site location within the vaporized droplet and suggests that an increase in acoustic pressure to vaporize increasingly smaller droplets is likely a result of reliance on the higher harmonics in a shocked wave propagation.
- Modulation of acoustic pressure and pulse length can mitigate likelihood to collapsing the bubble immediately after phase conversion, which was also a previously unseen dynamic phenomena.
- Confinement of the droplet in a microchannel has no effect on geometric pattern seen in bubble nucleus formation within the droplet. However, viscous effects from the walls do limit the ability of the bubble to collapse from the acoustic wave and limit growth rate of the bubble due to ADV expansion.

- A numerical model developed suggests that bubble lodging is enhanced by the geometry of the bifurcation. Lodging is further enhanced by adhesion forces from the three phase contact line which is geometrically enhanced through turns in the vessel interfaces.
- An atomization process may occur within the bubble when the bubble is hit by a sufficiently intense acoustic wave, which is the result of capillary wave formation along the interface of the bubble, and is threshold limited by acoustic peak negative pressure.

Future Directions

Having developed a well correlated model predicting nuclei formation and establishing a reasonable hypothesis behind the mechanism driving ADV, more refined models and parameter studies should be carried out to assist in maximizing vaporization efficiency. Although the current simulation carried out was able to accurately estimated position of the primary nucleation site formed, the model was based on the assumption of linear acoustics. By moving towards non-linear acoustic models the build of up non-linear wave interactions not only in the bulk fluid but also within the droplet can be more accurately captured. Non-linear acoustic models should more accurately predict the pressures developed within the droplet as potentially help estimate acoustic pressure threshold for ADV. Once pressure thresholds have been determined, parameter studies investigating the effects of acoustic frequency, transducer f-number, droplet distribution, and perfluorocarbon (PFC) fluid properties on acoustic pressures developed within the droplet will help guide development of transducer design and droplet construction to maximize vaporization efficiency. Numerical models predicting location nucleation site formation

could be coupled to volume of fluid based methods of determining liquid to gas conversion of PFC. Coupled with further ultra-high speed imaging experiments, the gas conversion rate could be better estimated, feeding into the development of more accurate models to describe the dynamic process of ADV and bubble expansion and predicting various stresses that could occur *in vivo*.

Additional ultra-high speed imaging experiments visualizing the ADV process should be carried out to isolated cell damage resulting from ADV and possible bubble torus formation. Observing isolated individual droplet vaporization in near the vicinity of a cultured monolayer of endothelial cells would allow the determination of when in the vaporization timeline and under what conditions result in cellular damage. It remains unclear if vessel damage from ADV is limited by the bubble expansion process itself or if collapse events of the bubbles are driving cell death. If bubble torus formation is indeed correlated with cell injury, then the balance of pulse length with acoustic power settings can be weighed for maximizing vaporization efficiency while minimizing (or controlling) cell injury.

In vivo experiments have shown that vessel damage can be incurred from ADV exposure[16]. The results using the PDMS channels during the idealized vessel vaporization experiments described in chapter four showed no sign of wall distortion. If similar channel confined vaporization experiments could be reproduced in softer gel based environments with known mechanical properties, wall deformation from ADV could be observed using high speed imaging. Furthermore, if both the gel phantom along with the bulk fluid surrounding the vaporized droplet were doped with small tracer particles, particle imaging velocimetry techniques could be implemented to capture more accurate estimates of the flow

field and stress fields in the deforming solid domain could be reconstructed with the particle displacement field as boundary conditions for a finite element model[17-20]. Alternatively, boundary integral methods similar to that used in Chapter VI could be implemented if accurate measurements of the deforming boundary can be extracted.

Preliminary results visualizing ADV events at channel bifurcations using ultra-high speed imaging have shown that the resulting bubbles have a tendency to expand at high velocities into the parent channel. In many cases the bubble expansion carries fluid momentum propelling the droplet (Figure 7.1). Relative to bubble expansion in straight channels, expansion at bifurcations may result in elevated stresses incurred at the carina of the bifurcation as well as increase wall shears incurred throughout the parent channel. Further analysis must be performed to quantify the stresses associated with bifurcation expansion events. Because of the early stage contact with the vessel wall, possibly lower order one dimensional models using a modified Bernoulli's equation could potentially be developed to describe the expanding bubble plug like motion[21,22].

There is increasing interest in not just drug delivery to the systemic system but also into mechanisms to penetrate the blood brain barrier[23]. Although many groups have taken a sonoporation approach to locally delivering drugs, the process has been often associated with cavitation and potential tissue damage[24-26]. Although it is still debated whether stable cavitation or inertial cavitation is the driving force behind sonoporation, it is generally accepted that the stresses imposed from bubbles responding from the acoustic field are what is responsible for promoting increased membrane permeability[23, 27, 28]. Having observed an atomization of the bulk fluid within a bubble due to an acoustic pulse and hypothesizing that wall shears from the bubble oscillation could transiently open up tight junctions between the

endothelial cells, cell experiments must be carried out to test if atomization is a viable method of promoting tissue drug update.

Although improvements in ADV efficiency and minimization of undesired bioeffects can be controlled through the ultrasound parameters, several advances can be done through the design of the droplet. Because the droplet distribution is far from being monodisperse using the typical methods of high speed shaking or sonication, a substantial volume of the droplets are too large and may lodge in the microcirculation prior to arriving to the location of interest. This is in contrast to the overwhelming number of droplets that are potentially too small to serve as an effective embolizing agent even after vaporization because the resulting diameter is far too small (Figure 2). This motivates the development of a high-throughput production method of monodisperse droplets specific to therapeutic application[29-34]. Although microfluidic devices have historically been shown to generate consistently monodisperse droplet populations, several physical barriers prevent immediate application to gas embolotherapy applications. First, typical microfluidic applications producing droplets are aimed at droplet populations around tens if not hundreds of microns in diameter. Scaling down to single micron or nanoscale droplets results in high pressure gradients and potential device failure from channel occlusion. Furthermore, production rates for a single channel device normally are rate limited and production rates at on the order of one of five thousand droplets per second[29, 31, 33]. However, typical droplet counts from sonication or high speed shaking results in droplet counts on the order to 10^9 droplets. In order to achieve a similar droplet count, a single device would have to operate for several days to achieve one sample. This motivated early investigation of parallel production of microdroplets. By using cross junctions to with low channel heights relative to width,

relatively large diameter flat disk shaped droplet can be produced which later form sub-10 micron spherical droplets in reservoirs. Preliminary results have also shown that the production can successfully produce monodisperse droplets on a single five junction parallel device constructed from PDMS at rates close to 25,000 droplets/second. These droplet production microfluidic devices would still need to be extended to massively parallel systems with hundreds of cross junctions operating in parallel to achieve ideal production rates of millions of droplets per second for clinical application. Finally, microfluidic droplet production methods can be extended to precise manufacturing of multicomponent droplet designs that balance the volume of vaporizable PFC material and drug diffused material for localized drug delivery[34, 35].

Chapter VII: Figures

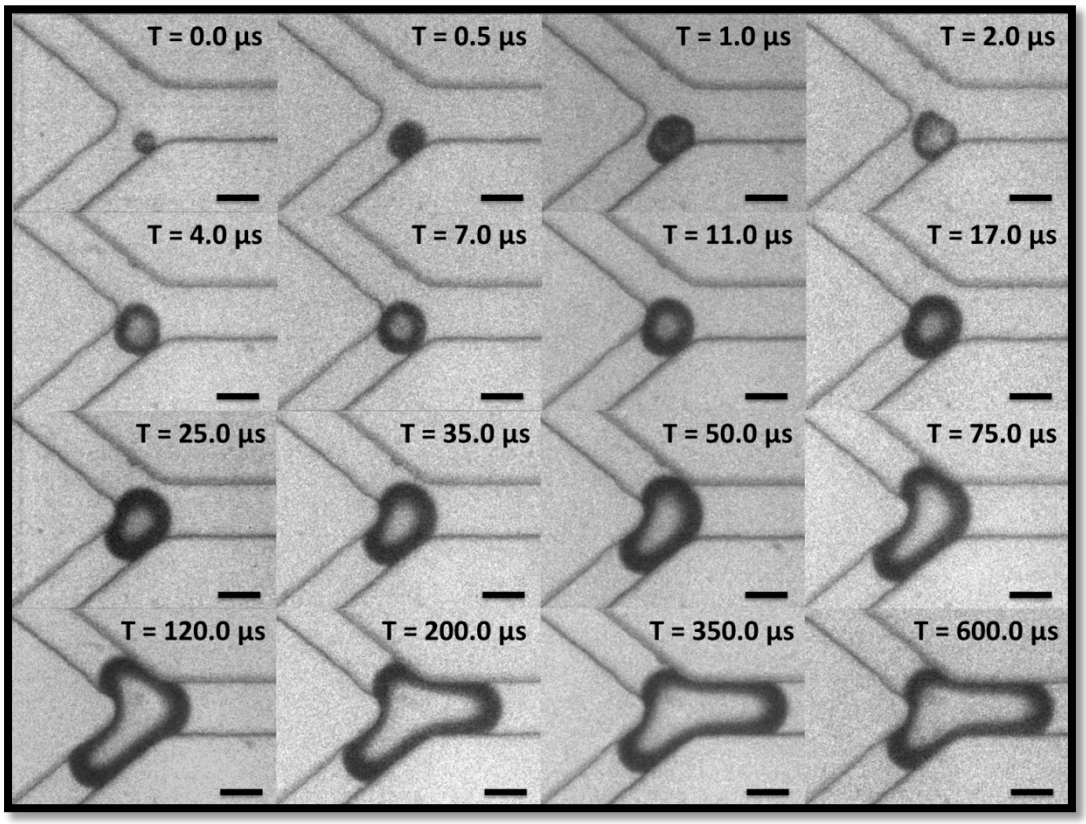

Figure 7. 1: ADV expansion of an initially 10.5 µm PFC bubble at a bifurcation. The bifurcation has a parent channel diameter of 25 µm parent channel (right) and daughter channels (left) which are 78% the parent channel in diameter. At 11 µs a portion of the bubble is in lower daughter channel and the remainder of the bubble is that the junction of the bifurcation. Momentum transfer from the bubble against the bifurcation point at 75 µs into the expansion causes the bubble to expand into the parent channel. Momentum from the bubble expanding into the parent channel likely causes the contact lines in the two daughter channels to recede (T=120 to 600 µs) closer to the parent channel.

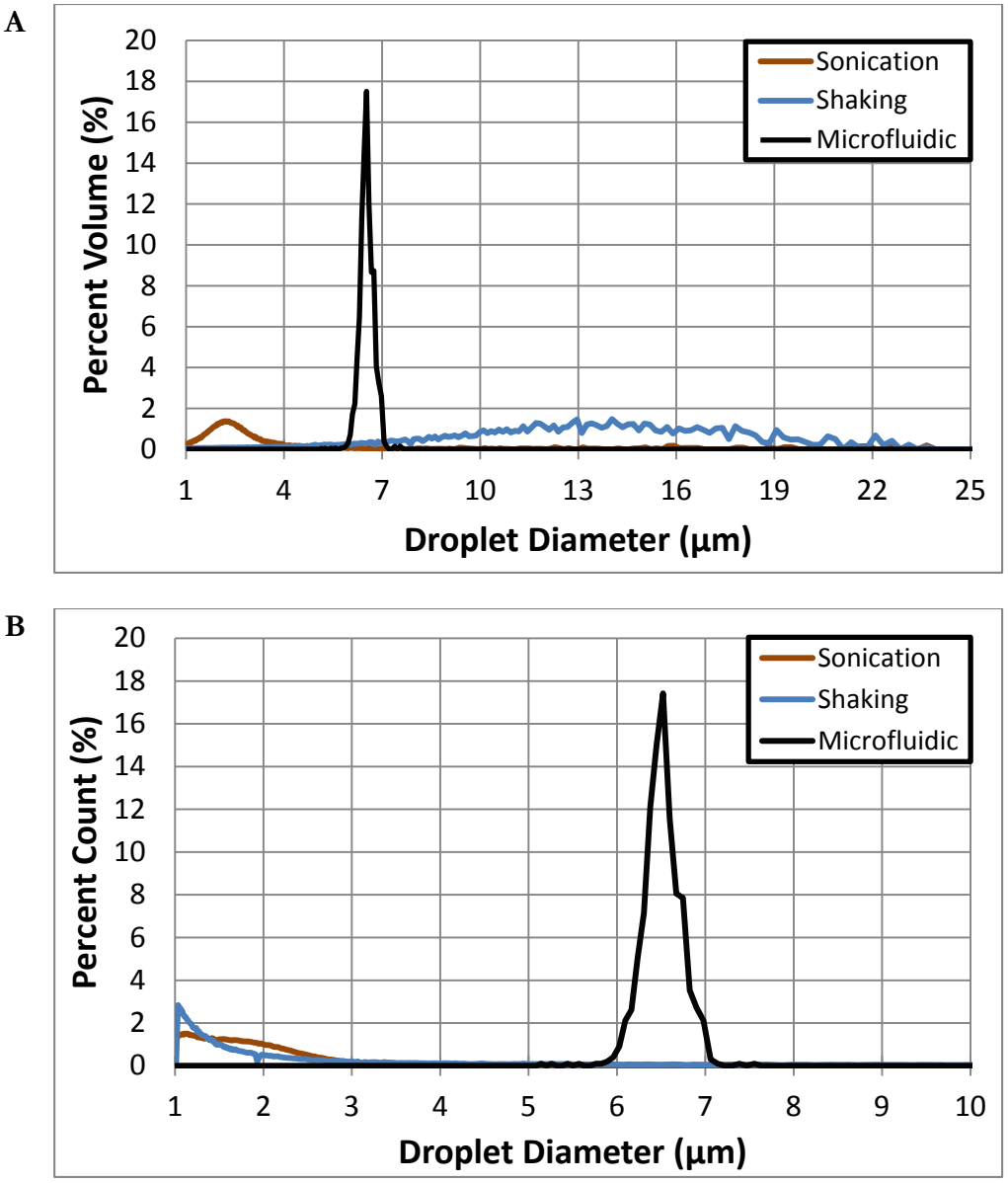

Figure 7. 2: Histograms of droplet distribution generator through sonication, high speed shaking and microfluidic methods are shown above in terms of (A) percent volume and (B) percent count. High speed shaking methods result in a non-negligible number of large droplets that account for majority of the droplet volume. Sonication provides an improved distribution, but the majority of droplets by count are closer to 1 µm in diameter. Microfluidic production of droplets has closely corresponding peaks for both volume and count, indicative of the monodisperse distribution of the droplets.

Chapter VII: References

[1] C. E. Brennen, Cavitation and Bubble Dynamics, New York, New York: Oxford University Press, 1995.

[2] T. G. Leighton, The Acoustic Bubble, Southampton, UK: Academic Press, 1994.

[3] T. Giesecke and K. Hynynen, "Ultrasound-Mediated Cavitation Threshols of Liquid Perfluorocarbon Droplets in Vitro," *Ultrasound in Medicine and Biology,* pp. 1359-1365, 2003.

[4] R. Seda, *Personal Communication,* Ann Arbor, MI, 2013.

[5] T. D. Donnelly, J. Hogan, A. Mugler, N. Schommer, M. Schubmehl, A. J. Bernoff and B. Forrest, "An Experimental Study of Micron-Scale Droplet Aerosols Produced via Ultrasonic Atomization," *Physics of Fluids,* vol. 16, no. 8, pp. 2843-2851, 2004.

[6] M. Faraday, "On a Peculiar Class of Acoustical Figures; and on Certain Forms Assumed by Groups of Particles upon Vibrating Elastic Surfaces," *Philosophical Transactions of the Royal Society of London,* vol. 121, pp. 299-340, 1831.

[7] R. J. Lang, "Ultrasonic Atomization of Liquids," *The Journal of the Acoustical Society of America,* vol. 34, no. 1, pp. 6-8, 1962.

[8] R. L. Peskin and R. J. Raco, "Ultrasonic Atomization of Liquids," *The Journal of the Acoustical Society of America,* vol. 35, no. 9, pp. 1378-1381, 1963.

[9] A. Qi, L. Y. Yeo and J. R. Friend, "Interfacial Destabilization and Atomization Driven by Surface Acoustic Waves," *Physics of Fluids,* vol. 20, no. 7, pp. 074103-1, 2008.

[10] B. J. W. S. Rayleigh, The theory of sound, Macmillan, 1896 Vol. 2.

[11] J. C. Simon, O. A. Sapozhnikov, V. A. Khokhlova, Y.-N. Wang, L. A. Crum and M. R. Bailey, "Ultrasonic Atomization of Tissue and its Role in Tissue Fractionation by High Intensity Focused Ultrasound," *Physics in Medicine and Biology,* vol. 57, pp. 8061-8078, 2012.

[12] S. S. Yoon and S. D. Heister, "A nonlinear atomization model based on a boundary layer instability mechanism," *Physics of Fluids,* pp. 16(1): 47-61, 2004.

[13] T. Kodama and Y. Tomita, "Cavitation Bubble Bahavior and Bubble-Shock Wave Interaction Near a Gelatin Surface as a Study of in Vivo Bubble Dynamics," *Applied Physics B: Lasers and Optics,* vol. 70, pp. 139-149, 1999.

[14] E. Johnsen and T. Colonius, "Numerical Simulations of Non-Spherical Bubble Collapse," *Journal of Fluid Mechanics,* vol. 629, pp. 231-262, 2009.

[15] J. R. Blake, G. S. Keen, R. P. Tong and M. Wilson, "Acoustic Cavitation: The Fluid Dynamics of Non-Spherical Bubbles," *Philisophical Transactions of The Royal Society A,* vol. 357, pp. 251-267, 1999.

[16] S. Samuel, A. Duprey, M. L. Fabiilli, J. L. Bull and J. B. Fowlkes, "In Vivo Microscopy of Targeted Vessel Occlusion Employing Acoustic Droplet Vaporization," *Microcirculation,* vol. 19, pp. 501-509, 2012.

[17] W. R. Legant, J. S. Miller, B. L. Blakely, D. M. Cohen, G. M. Genin and C. S. Shen, "measurement of Mechanical Trantions exerted by Cells in Three-Dimensional Matrices," *Nature Methods,* vol. 2, no. 12, pp. 969-974, 2010.

[18] C. Franck, S. Hong, S. A. Markarinec, D. A. Tirrell and G. Ravichandran, "Three-dimensional Full-field Measurements of Large Deformations in Soft Materials Using Confocal Microscopy and Digital Volume Correlation," *Experimental Mechanics,* vol. 47, pp. 427-438, 2007.

[19] S. Bian, C. F. Tai, D. Halpern, Y. Zheng and J. B. Grotberg, "Experimental Study of Flow Fields in an Airway Closure Model," *Journal of Fluid Mechanics,* vol. 647, pp. 391-402, 2010.

[20] Y. C. Lin, D. O. Brant, R. H. Bartlett, R. B. Hirschl and J. L. Bull, "Pulsatile Flow Past a Cylinder: An Experimental Model of Flow in an Artificial Lung," *ASAIO Journal,* vol. 6, no. 614-623, p. 52, 2006.

[21] D. T. Valassis, R. E. Dodde, B. Eshpuniyani, J. B. Fowlkes and J. L. Bull, "Microbubble Transport Through a Bifurcating Vessel Network with Pulsatile Fow," *Biomedical Microdevices,* vol. 14, pp. 131-143, 2012.

[22] A. Qamar, Z. Z. Wong, J. B. Fowlkes and J. L. Bull, "Dynamics of Acoustic Droplet Vaporization in Gas Embolotherapy," *Applied Physics Letters,* pp. 143702-1-3, 2010.

[23] C. C. Chen, P. S. Sheeran, S.-Y. Wu, O. O. Olumolade, P. A. Dayton and E. E. Konofagou, "Targeted Drug Delivery with Focused Ultrasound-Induced Blood-Brain Barrier Opening Using Acoustically-Activated Nanodroplets," *Journal of Controlled Release,* p. In Press, 2013.

[24] K. Ferrara, R. Pollard and M. Borden, "Ultrasound Microbubble Contrast Agents: Fundamentals and Application to Gene and Drug Delivery," *Annual Review of Biomedical Engineering,* vol. 9, pp. 415-447, 2007.

[25] S. Hernot and A. L. Klibanov, "Microbubbles in Ultrasound-Triggered Drug and Gene Delivery," *Advanced Drug Delivery Reviews,* vol. 60, no. 10, pp. 1153-1166, 2008.

[26] M. S. Tartis, J. McCallan, A. F. Lum, R. LaBell, S. M. Stieger, T. O. Matsunaga and K. W. Ferrara, "Theraputic effects of paclitaxel-containing ultrasound contrast agents," *Ultrasound in Medicine & Biology,* p. 32(11):1771–1780, 2006.

[27] D. L. Miller, S. L. Pislaru and J. F. Greenleaf, "Sonoporation: Mechanical DNA Delivery by Ultrasonic Cavitation," *Somatic Cell and Molecular Genetics,* vol. 27, no. 1, pp. 115-134, 2002.

[28] K. W. Ferrara, "Driving delivery vehicles with ultrasound," *Advanced Drug Delivery Reviews,* p. 60:1097–1102, 2008.

[29] I. Kobayashi, S. Mukataka and M. Nakajima, "Production of Monodisperse Oil-in-Water Emulsions Using a Large Silicon Straight-Through Microchannel Plate," *Industrial and Engineering Chemistry Research,* vol. 44, pp. 5852-5856, 2005.

[30] K. Hettiarachchi, E. Talu, M. L. Longo, P. A. Dayton and A. P. Lee, "On-Chip Generation of Microbubbles as a Practical Technology for Manufacturing Contrast Agents for Ultrasonic Imaging," *Lab on a Chip,* vol. 7, pp. 463-468, 2007.

[31] M. K. Mulligan and J. P. Rothstein, "Scale-Up and Control of Droplet Production in Coupled Microfluidic Fow-Focusing Geometries," *Microfluidics and Nanofluidics,* vol. 13, pp. 65-73, 2012.

[32] Q. Xu and M. Nakajima, "The Generation of Highly Monodisperse Droplets Through the Breakup of Hydrodynamically Focused Microthread in a Microfluidic Device," *Applied Physics Letters,* vol. 85, no. 17, p. 3726, 2004.

[33] W. Li, E. Young, M. Seo, Z. Nie, P. Garstecki, C. Simmons and E. Kumacheva, "Simultaneous Generation of Droplets with Different Dimensions in Parallel Integrated Microfluidic Droplet Generators," *Soft Matter,* vol. 4, p. 258–262, 2007.

[34] L. Shui, J. Eijkel and A. van der Berg, "Multiphase Flow in Microfluidic Systems – Control and Applications of Droplets and Interfaces," *Advances in Colloids and Interface Sciences,* vol. 133, pp. 35-49, 2007.

[35] W. Wang, R. Xie, X.-J. Ju, T. Luo, L. Liu, D. A. Weitz and L.-Y. Chu, "Controllable Microfluidic Production of Multicomponent Multiple Emulsions," *Lab on a Chip,* 2011.

APPENDICIES

APPENDIX I: Photolithography Procedure

One of the challenges of microfabrication is surface adhesion between SU-8 and your substrate (e.g. glass or silicon). Surface adhesion issues normally present themselves in the forms of delamination of SU-8 from the substrate from repeated castings or accidental removal of <25 micron features during rinsing steps during fabrication. This document is an adaptation of MicroChem's procedure on using SU-8 2000 series on how to microfabricate microfluidic molds[1, 2]. The purpose of the modified procedure is to ensure strong adhesion between mold features and the substrate, extend lifetime of the mold, and guarantee features down to single micron widths adhere to the substrate.

Pretreatment

The goal of the pretreatment is to add extra contact area between the features of interest and the substrate, which is normally silicon.

1. Center silicon wafer (or substrate) on spin-coater and apply vacuum.
2. Dispense 4 ml of SU-8 2002 (MicroChem) onto center of silicon wafer and spin at:
    a. 500 RPM for 5 seconds at acceleration of 100 RPM/second.
    b. Continue to 2500 RPM for additional 25 seconds (30 seconds total) at acceleration of 300 RPM/second.
3. Edge bead removal – run a wipe or cotton swab along edge of the substrate to remove finger-like projections of SU-8.
4. Soft bake – transfer coated substrate to hot plate and bake:
    a. Pre-bake at 60°C for 1 minute.
    b. Ramp to 95°C and bake for 2 minutes.
    c. Turn hot plate off and cool for 30-60 minutes.

5. UV exposure – transfer coated substrate for UV exposure. Layer should be 2 microns thick, requiring 80 mW/cm^2 for correct UV exposure. The mask aligner used output 17 mW/(cm^2·sec), therefore exposures should be 4.7 seconds.
6. Post-Exposure Bake – transfer coated substrate to hot plate and bake:
    a. Pre-bake at 60°C for 1 minute.
    b. Ramp to 95°C and bake for 2 minutes.
    c. Turn hot plate off and cool for 30-60 minutes.

Photolithography

Masks were designed using SolidWorks and submitted to CAD/Art, Inc. emulsion up for high resolution prints.

1. Center pre-treated silicon wafer on spin-coater and apply vacuum.
2. Dispense 4 ml of SU-8 2000 series (MicroChem) onto center of silicon wafer and spin. SU-8 formulations used and spin times used can be found in table A1.1. See MicroChem datasheets on SU-8 2000 series for calibration charts on spin time and feature height[1, 2].

Ideal Height (μm)	**SU-8**	**Spin 1 (RPM)**	**Accel. (RPM/sec)**	**Time (sec)**	**Spin 2 (RPM)**	**Accel. (RPM/sec)**	**Time (sec)**	**Measured Height (μm)**
10	SU-8 2007	500	100	5	1700	300	25	9.2
25	SU-8 2015	500	100	5	1950	300	25	23.6
50	SU-8 2025	500	100	5	1900	300	25	49.8
100	SU-8 2075	500	100	5	2700	300	25	93.6

Table A1. 1: Spin times for varying channel heights used for idealized vessel models.

3. Edge bead removal – run a fiber-free wipe or cotton swab along edge of the substrate to remove finger-like projections of SU-8.

4. Soft bake – transfer coated substrate to hot plate and bake. Bake times used are shown in the table below in table A1.2. Once bake steps are complete, turn off hot plate and allow to cool on plate for 30-60 min before proceeding.

Ideal Height (μm)	**SU-8**	**Prebake at 60°C (min)**	**Bake at 95°C (min)**
10	SU-8 2007	1	3
25	SU-8 2015	1	4
50	SU-8 2025	3	6
100	SU-8 2075	5	12

Table A1. 2: Soft-bake times for varying channel heights used for idealized vessel models.

5. UV exposure – transfer coated substrate for UV exposure. For the exposure doses used see the table below in table A1.3.

Ideal Height (μm)	**SU-8**	**Exposure Dose (mW/cm^2)**	**Exposure Time (sec)**
10	SU-8 2007	150	9
25	SU-8 2015	170	9.8
50	SU-8 2025	190	11.0
100	SU-8 2075	260	15.0

Table A1. 3: Exposure times for varying channel heights used for idealized vessel models.

6. Post-Exposure Bake – transfer coated substrate to hot plate and bake. See table A1.4 for bake times used. Once bake steps are complete, turn off hot plate, and allow to cool on plate for 60 min before proceeding.

Ideal Height (μm)	SU-8	Prebake at 60°C (min)	Bake at 95°C (min)
10	SU-8 2007	1	4
25	SU-8 2015	1	5
50	SU-8 2025	2	6
100	SU-8 2075	5	10

Table A1. 4: Post-exposure bake times used for varying channel heights used for idealized vessel models.

7. Development – Wafers should be transferred over to a bath of MicroChem's SU-8 Developer Solution. Development time is based on channel height and should be sprayed with fresh development solution every minute to help expose features. The development times used can be found in table A1.5.

Ideal Height (μm)	SU-8	Development Time (min)
10	SU-8 2007	4
25	SU-8 2015	5
50	SU-8 2025	7
100	SU-8 2075	10

Table A1. 5: Development times used for varying channel heights used for idealized vessel models. Every minute additional developer solution was used to spray the surface of the wafer molds to ensure removal of excess SU-8.

8. Rinse and dry – both sides of the wafer should be thoroughly rinses using isopropyl alcohol followed by DI water. Repeat the process a minimum of 2 times. Dry by blowing compressed air or, preferably, nitrogen across both sides of the wafer onto a clean fiber-free wipe.

9. Hard bake – A final high temperature bake step is needed to annealing the SU-8 to the substrate. Hard bake was performed by slowly raising the wafers from room temperature to 150-200°C and baked for 30-60 minutes on a hot plate. The hot plate was turned off and the wafers were allowed to slowly return to room temperature over a 2 hour period.

Appendix I: References

[1] MicroChem, "SU-8 2000 Permanent Epoxy Negative Photoresist Processing Guidelines For: SU-8 2000.5, SU-8 2002, SU-8 2005, SU-8 2007, SU-8 2010 and SU-8 2015," [Online]. Available: http://microchem.com/pdf/SU-82000DataSheet2000_5thru 2015Ver4.pdf. [Accessed 10 May 2013].

[2] MicroChem, "SU-8 2000 Permanent Epoxy Negative Photoresist Processing Guidelines for: SU-8 2025, SU-8 2035, SU-8 2050 and SU-8 2075," [Online]. Available: http://microchem.com/pdf/SU-82000DataSheet2025thru2075Ver4.pdf. [Accessed 10 May 2013].

APPENDIX II: Spin Coating PDMS

Spin coating PDMS allows for controlled PDMS thicknesses.

1. Center silicon wafer mold on spin coater and apply vacuum.

2. Dispense 4 ml of degassed PDMS mixed at a 10:1 ratio of elastomer to cross-linking agent onto center of wafer.

3. Spin wafer at a 500 RPM accelerating at 110 RPM/second for desired thickness at times specified below in figure A2.1

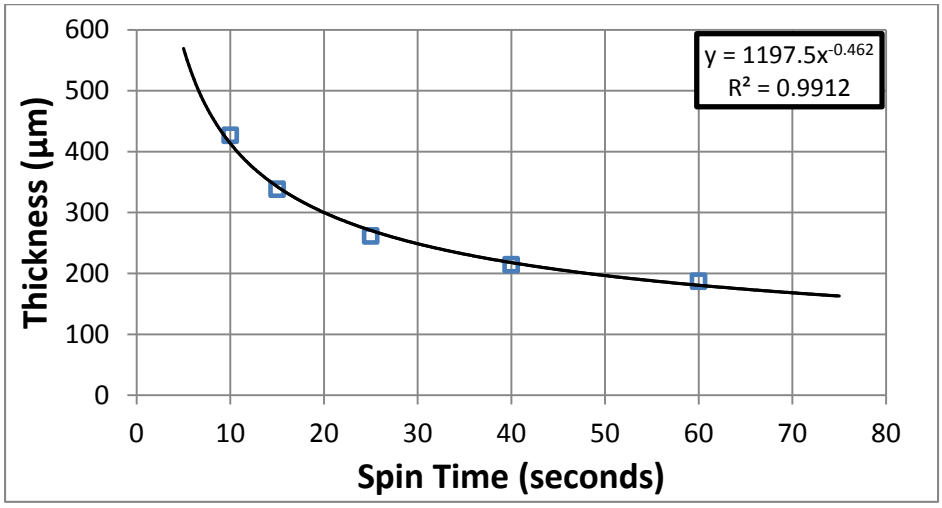

Figure A2. 1: Spin time at 500 RPM and acceleration of 110 RPM/second for PDMS to control PDMS wall thickness. A power law function was used to approximate PDMS thickness as a function of spin time.

4. Using a fiber-free wipe clean off edge of wafer to remove excess PDMS.

5. Transfer wafer to hot plate and bake at 65°C for 30 minutes minimum, 3 hours for full cure.